学位論文

Evidence for the Higgs boson decaying to a pair of b quarks
(b クォーク対に崩壊するヒッグス粒子の証拠)

東京大学大学院理学系研究科
物理学専攻
加藤 千曲

Abstract

The Higgs boson was predicted in the Standard Model (SM) to explain the masses of elementary particles. The Large Hadron Collider (LHC) is used to test the SM in proton-proton collisions at unprecedented center of mass energy. The results are important to search for new physics beyond the SM, which can potentially explain unsolved problems such as hierarchy problem, baryon number, dark matter, neutrino mass and so on. ATLAS and CMS experiments at the LHC discovered the Higgs boson in 2012 (Run1). The mass is about 125 GeV and the properties are consistent with the SM so far. However, the Higgs boson decaying to a pair of b quarks ($H \to bb$) was not observed in Run1, because of large amount of background and limited statistics of data. Therefore, the $H \to bb$ is followed with great attention in the 2nd run from 2015 (Run2).

This thesis presents a piece of evidence for the $H \to bb$. The LHC Run2 proton-proton collisions data collected with the ATLAS detector is used. The center of mass energy is 13 TeV, and the integrated luminosity is 36.1 fb^{-1}. ATLAS level-1 endcap muon trigger achieved about 90% trigger efficiency. A b-jet energy correction improved the Higgs mass resolution about 40% at maximum. An excess over background is found in the Vector boson associated production (VH) 2-lepton channel. The observed (expected) significance is 3.6 (1.9) standard deviations. The signal strength compared to the SM is 2.11 $^{+0.50}_{-0.48}$ (stat.) $^{+0.65}_{-0.47}$ (syst.). In ATLAS VH 0, 1, 2-lepton, Run1 + Run2 combined results, the observed (expected) significance is 3.6 (4.0) standard deviations. The signal strength is 0.90 $^{+0.18}_{-0.18}$ (stat.) $^{+0.21}_{-0.19}$ (syst.). The results are consistent with the SM.

Contents

Chapter 1

Introduction

The Higgs boson was predicted in the Standard Model (SM) to explain the masses of elementary particles [1, 2, 3, 4, 5, 6]. The Large Hadron Collider (LHC) is used to test the SM in proton-proton collisions at unprecedented center of mass energy. The results are important to search for new physics beyond the SM, which can potentially explain unsolved problems such as hierarchy problem, baryon number, dark matter, neutrino mass and so on. ATLAS and CMS experiments at the LHC discovered the Higgs boson in 2012 (Run1) [7, 8]. The mass is about 125 GeV and the properties are consistent with the SM so far [9].

However, the Higgs boson decaying to a pair of b quarks ($H \rightarrow bb$) was not observed in Run1, because of large amount of background and limited statistics of data [10, 11]. The $H \rightarrow bb$ is the most dominant decay of the Higgs boson, which has branching ratio of 58% in the SM. The rate is important to test the Yukawa coupling in the SM, and also sensitive to new physics beyond the SM [12]. For example, Higgs portal models predict Higgs boson decay to dark matter, and Supersymmetry models also predict modification to the coupling.

Historically, CDF and D0 combination reported an excess for the $H \rightarrow bb$ with significance of 2.8 standard deviations at 125 GeV [13]. The Tevatron proton-antiproton collisions data, at center of mass energy of 1.96 TeV, integrated luminosity of 9.7 fb^{-1} was used. ATLAS and CMS combination reported an excess for the $H \rightarrow bb$ with observed (expected) significance of 2.6 (3.7) standard deviations [14]. The LHC proton-proton collisions data at 7 and 8 TeV, integrated luminosities of approximately 5 and 20 fb^{-1} was used. However, as shown in Figure 1.1, the error on the the signal strength was still large, and the central value was lower than the SM. Therefore, the $H \rightarrow bb$ is followed with great attention in the 2nd run from 2015 (Run2).

For the $H \rightarrow bb$, the first and the 2nd largest cross-section Higgs boson production, gluon gluon Fusion and Vector Boson Fusion, have low sensitivity. Because the $H \rightarrow bb$ is reconstructed as 2 b-jets in the final state, and thus it is hard to separate from the multi-jet background. Therefore, the 3rd largest cross-section Higgs boson production, Vector boson associated production (VH), becomes the most sensitive channel for the $H \rightarrow bb$. In this channel, signal events can be selected efficiently by using final state leptons.

In VH, there are 3 channels depending on number of reconstructed leptons: $ZH \rightarrow \nu\nu bb$ (0-lepton), $WH \rightarrow \ell\nu bb$ (1-lepton), $ZH \rightarrow \ell\ell bb$ (2-lepton). The 2-lepton channel has a smaller signal yield compared to the other channels. However, fully reconstructed $Z \rightarrow \ell\ell$ allows to suppress the multi-jet and $t\bar{t}$ background strongly. Furthermore, it is possible to improve the Higgs mass resolution, by constraining the $\ell\ell bb$ to be balanced in the transverse plane (Kinematic Fit). This thesis mainly presents the 2-lepton analysis and also review the ATLAS combined results. The LHC Run2 proton-proton collisions data collected with the ATLAS detector is used. The center of mass energy is 13 TeV and the integrated luminosity is 36.1 fb^{-1}.

This thesis is organized as follows: In Chapter 2, the SM and the Higgs boson are reviewed. In Chapter 3,
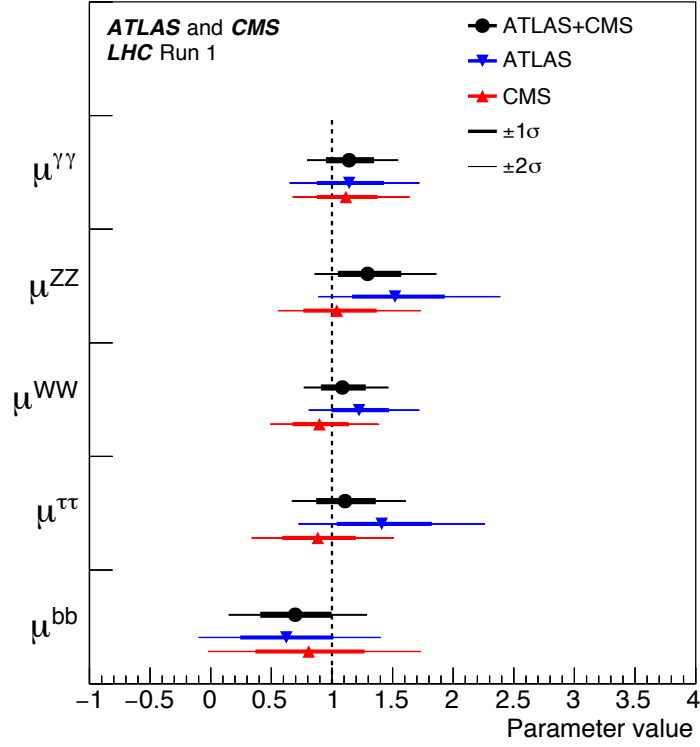
Figure 1.1   The signal strength of the Higgs boson decay in Run1 [14]. μ^{bb} is the signal strength of the $H \to bb$.

the LHC and the ATLAS detector are briefly reviewed. In Chapter 4, data and simulated samples used in this analysis are summarized. In Chapter 5, definitions of physics object in this analysis are briefly described. In Chapter 6, event selection in this analysis is summarized. In Chapter 7, b-jet energy corrections to improve the Higgs mass resolution is presented. In Chapter 8, multivariate analysis to improve the background separation further is briefly presented. In Chapter 9, systematic uncertainties in this analysis are summarized. In Chapter 10, statistical analysis is described. In Chapter 11, results are shown. In Chapter 12, the ATLAS combined results are reviewed. In Chapter 13, conclusion is given.

The results are based on thousands of people's work in the LHC-ATLAS experiment. The author's direct contribution to the results is summarized as follows. The author worked for ATLAS Level1 endcap muon trigger (TGC) at the beginning of Run2. In 2012, the author participated in the production of new TGC to replace broken chambers. In 2014, the author worked for the chamber replacement, electronics, power supply and cooling system. Until 2016, the author participated in the expert on-call shift. From 2015, the author worked for the analysis. For example, the author contributed to muon in jet selection, p_{T} dependent correction, lepton trigger studies, Kinematic Fit for Run2, implementation, validation and production of calibrated datasets, multi-jet studies, approval of ICHEP 2016, modeling and validation of b-jet energy correction.

Chapter 2

The Standard Model and the Higgs boson

The Standard Model (SM) describes elementary particles and fundamental interactions. The Higgs boson was predicted in the SM to explain the masses of elementary particles. In order to establish a search strategy for the $H \to bb$, it is important to review theoretical background and status of the the Higgs boson measurement. In this chapter, the SM and cross-section in proton-proton collisions are briefly summarized in Section 2.1, status of the the Higgs boson measurement and a search strategy for the $H \to bb$ are summarized in in Section 2.2.

2.1 The Standard Model

In this section, elementary particles in the SM are summarized in Subsection 2.1.1, the spontaneous symmetry breaking is briefly summarized in Subsection 2.1.2, cross-section in proton-proton collisions is briefly reviewed in Subsection 2.1.3.

2.1.1 Elementary particles

Elementary particles in the SM is summarized in Table 2.1. Quarks and leptons (fermions) are building blocks of matter, and gauge bosons carry forces between them [15]. Fermions are spin-1/2 particles and gauge bosons are spin-1 particles. The parameters are summarized in the review of particle physics [9]. There are 3 generations (flavors) of fermions confirmed by experiments. The 1st generation particles are stable and make matter that we see every day. The 2nd and 3rd generation particles can only be seen in high energy physics and decay to the 1st generation particles. There are 3 forces included in the SM, electromagnetic force carried by photon (γ), weak force carried by weak bosons ($W^{\pm}$, Z), and strong force carried by gluon (g). Gravitational force is not included in the SM, as it is very small compared to the other forces. Neutrinos are considered to be massless in the SM. However, it is known that neutrinos has small masses, after observation of the neutrino oscillation [16].

2.1.2 Spontaneous symmetry breaking

Fundamental interactions of elementary particles are described by local gauge symmetry in the SM. The symmetry is related to the idea that the conserved quantities are conserved in local regions of space and time. The connection between the symmetry and the conservation is described by quantum field theory using the Lagrangian. The Lagrangian is defined as

$$L = T - V, \tag{2.1}$$

	Name	Spin	Charge	Mass
Quarks	u	1/2	+2/3	2.2 MeV
	d	1/2	-1/2	4.7 MeV
	c	1/2	+2/3	1.27 GeV
	s	1/2	-1/2	96 MeV
	t	1/2	+2/3	173 GeV
	b	1/2	-1/2	4.2 GeV
Leptons	e	1/2	2/3	0.511 MeV
	ν_e	1/2	-1/2	<2 eV
	μ	1/2	2/3	105 MeV
	ν_{mu}	1/2	-1/2	<0.19 MeV
	τ	1/2	2/3	1.78 GeV
	ν_{tau}	1/2	-1/2	<18.2 MeV
Gauge Bosons	γ	1	0	0 GeV
	g	1	0	0 GeV
	$W^\pm$	1	± 1	80 GeV
	Z	1	0	91 GeV

Table 2.1   Elementary particles in the SM [9]. Anti-particles of quarks and leptons are not listed as they are identical particles with opposite sign quantum numbers.

where T is kinematic energy and V is potential energy of the system. In classical mechanics, equation of motion of particles is obtained from the Lagrange's equation

$$\frac{d}{dt}\left(\frac{\partial L}{\partial \dot{q}_i}\right) - \left(\frac{\partial L}{\partial q_i}\right) = 0, \tag{2.2}$$

where q_i are coordinates of particles and t is time. The formalism can be extended to a continuous system. For example (2.1) becomes

$$L(q_i, \dot{q}_i, t) \to \mathcal{L}\left(\phi, \frac{\partial \phi}{\partial x_\mu}, x_\mu\right), \tag{2.3}$$

where ϕ is a field as functions of continuous parameters x_μ, and (2.2) becomes

$$\frac{\partial}{\partial x_\mu}\left(\frac{\partial \mathcal{L}}{\partial(\partial \phi/\partial x_\mu)}\right) - \left(\frac{\partial \mathcal{L}}{\partial \phi}\right) = 0, \tag{2.4}$$

where $\mathcal{L}$ is the Lagrangian density,

$$L = \int \mathcal{L} d^3 x, \tag{2.5}$$

which is just called as Lagrangian in the following. Lagrangian of the SM is written as

$$\mathcal{L}_{\mathrm{SM}} = \mathcal{L}_{\mathrm{Gauge}} + \mathcal{L}_{\mathrm{Higgs}} + \mathcal{L}_{\mathrm{Yukawa}}. \tag{2.6}$$

$\mathcal{L}_{\mathrm{Gauge}}$ describes gauge interactions of elementary particles. There are strong interaction (QCD) and electroweak interaction (EW) in gauge interactions.

The gauge symmetry forbids masses of elementary particles. This is consistent with photon and gluon to be massless. However, it is known that weak bosons and fermions have masses, as shown in Table 2.1. Therefore,

the masses are generated by spontaneous symmetry breaking. This introduces a scaler field that corresponds to the Higgs boson. $\mathcal{L}_{\text{Higgs}}$ is written as

$$\mathcal{L}_{\text{Higgs}} = |\mathcal{D}_\mu \phi|^2 - V(\phi), \tag{2.7}$$

where ϕ is a Higgs field, $\mathcal{D}_\mu$ is a covariant derivative, $V(\phi)$ is a Higgs potential

$$V(\phi) = \mu^2 |\phi|^2 + \lambda |\phi|^4, \tag{2.8}$$

where μ is a Higgs mass parameter and λ is a self-coupling. $\mu^2 < 0$ and $\lambda > 0$ is considered. In this case the potential become minimum at

$$|\phi|^2 = \frac{-\mu^2}{2\lambda} = \frac{v^2}{2}, \tag{2.9}$$

where

$$v = \sqrt{\frac{-\mu^2}{\lambda}}. \tag{2.10}$$

Now vacuum expectation value can be chosen as

$$\phi_0 = \frac{1}{\sqrt{2}} \begin{pmatrix} 0 \\ v \end{pmatrix}, \tag{2.11}$$

and thus spontaneous symmetry breaking occurred. Substituting (2.11) to (2.7), the gauge boson masses are generated as

$$m_W = \frac{1}{2} v g, \ m_Z = \frac{1}{2} v \sqrt{g^2 + g'^2} \tag{2.12}$$

$$\frac{g'}{g} = tan\theta_W, \ \frac{m_W}{m_Z} = cos\theta_W, \tag{2.13}$$

where g is SU(2) gauge coupling and g' is U(1) gauge coupling and θ_W is weak mixing angle. Fermion masses can also be generated using Yukawa coupling. For example, $\mathcal{L}_{\text{Yukawa}}$ is written as

$$\mathcal{L}_{\text{Yukawa}} = -G_d(\bar{u}, \bar{d})_L \phi d_R - G_u(\bar{u}, \bar{d})_L \phi_c u_R + H.C., \tag{2.14}$$

where G_u and G_d are the couplings, $(\bar{u}, \bar{d})_L$ is quark isospin doublet, d_R and u_R are down and up type quark singlet, and $H.C.$ is the Hermitian Conjugate. Spontaneously breaking the symmetry and substituting

$$\phi = \frac{1}{\sqrt{2}} \begin{pmatrix} 0 \\ v + h \end{pmatrix}, \ \phi_c = \frac{1}{\sqrt{2}} \begin{pmatrix} v + h \\ 0 \end{pmatrix}, \tag{2.15}$$

and choosing G_u and G_d to be

$$m_u = \frac{G_u v}{\sqrt{2}}, \ m_d = \frac{G_d v}{\sqrt{2}}, \tag{2.16}$$

(2.14) becomes

$$-m_d \bar{d}d - m_u \bar{u}u - \frac{m_d}{v} \bar{d}dh - \frac{m_u}{v} \bar{u}uh, \tag{2.17}$$

Thus, fermion masses are generated and the coupling is proportional to fermion masses.

2.1.3   Cross-section in proton-proton collisions

The SM can be tested in proton-proton collisions at the LHC [17]. Number of events of a process can be calculated from cross-section and integrated luminosity as

$$N = \sigma \int L dt, \tag{2.18}$$

where $\int L dt$ is integrated luminosity. Generally cross-section is calculated [18] and integrated luminosity is measured [19]. Since proton is made of valence quarks (uud), sea quarks and gluons, the structure is described by Parton Distribution Functions (PDF). The PDF are probability $f_i(x_i, Q^2)$ to find a parton with momentum fraction x_i with momentum transfer Q^2. They are determined from deep-inelastic scattering (DIS) and related hard-scattering data [20].

A production cross-section in proton-proton collision is described as

$$\sigma = \sum_{i,j} \int_0^1 dx_i dx_j f_i(x_i, Q^2) f_j(x_j, Q^2) \hat{\sigma}_{ij}, \tag{2.19}$$

where $\hat{\sigma}_{ij}$ is partonic cross-section for initial state partons i and j. The partonic cross-section is multiplied with the PDF f_i and f_j. The product is integrated over x_i, x_j, and all combinations of i, j are summed. Figure 2.1 shows proton-proton cross-sections as a function of center of mass energy.

The factorization theorem allows to calculate the cross-section, separating long-distance behavior from short-distance behavior [21] The long-distance behavior is not perturbatively calculable and needs to be factorized into the PDF. The short-distance behavior is perturbatively calculable. This introduces a scale (factorization scale).

The renormalization allows to remove infinities in the quantum correction. This also introduces a scale (renormalization scale). The partonic cross-section is calculated from the Lagrangian and perturbation theory. The precision of the calculation of QCD is called as Leading Order (LO), Next to Leading Order (NLO), Next to Next Leading Order (NNLO).

2.2   The Higgs boson

In this section, status of the Higgs boson measurement is briefly reviewed in Subsection 2.2.1, the Higgs boson production is summarized in Subsection 2.2.2, VH channel is discussed in Subsection 2.2.3.

2.2.1   Status of the Higgs boson measurement

ATLAS and CMS experiments discovered the Higgs boson in Run1 [7, 8]. Status of the measurements are summarized in [9]. The mass is measured to be

$$m_H = 125.09 \pm 0.21 \text{ (stat.)} \pm 0.11 \text{ (syst.) GeV.} \tag{2.20}$$

The width is predicted to be 4.2 MeV and constrained to be less than few GeV. Alternative models are excluded in favor of the SM Higgs boson quantum numbers, spin-0, CP-even [23]. However, the the Higgs boson decaying to a pair of b quarks ($H \to bb$) was not observed in Run1, because of large amount of background and limited statistics of data [10, 11]. The discovery (observed significance of 5 standard deviations) was mainly achieved by bosonic decay channels such as $H \to ZZ$, $H \to WW$, $H \to \gamma\gamma$, and fermionic decay channel was only discovered in $H \to \tau\tau$, as shown in Table 2.2. Therefore, $H \to bb$ is followed with great attention in Run2.
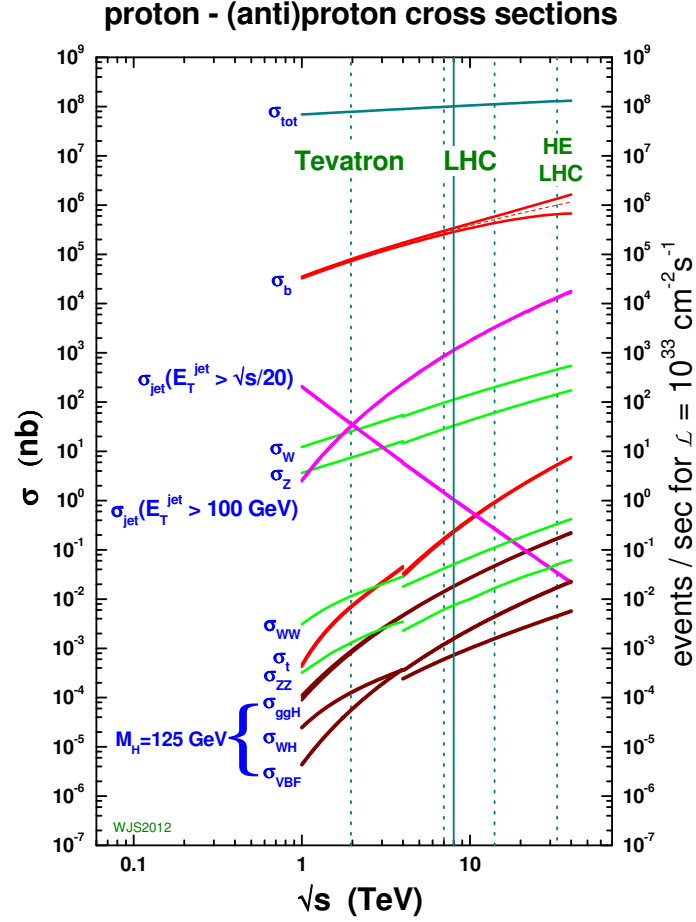
Figure 2.1   Proton-proton cross-sections as a function of center of mass energy [22]. Vertical lines are Tevatron 1.96 TeV, LHC 7 TeV, 14 TeV and High Energy LHC 33 TeV.

2.2.2   The Higgs boson production

Feynman diagrams of the Higgs boson production at the LHC are shown in Figure 2.2. There are:

- gluon gluon Fusion (ggF)
- Vector Boson Fusion (VBF)
- Vector boson associated production (VH)
- top quark pair associated production (ttH)

For ZH production there is also contribution from gluon induced signal ($gg \rightarrow ZH$), as shown in Figure 2.3. The Higgs boson branching ratios and production cross-sections are shown in Figure 2.4. ggF and VBF are the 1st and 2nd largest cross-section. However, they can not be used for $H \rightarrow bb$ search, because of the huge amount of multi-jet background. Therefore, VH, the 3rd largest cross-section, is the most sensitive channels for $H \rightarrow bb$. In this channel Signal events can be selected efficiently using final state leptons.
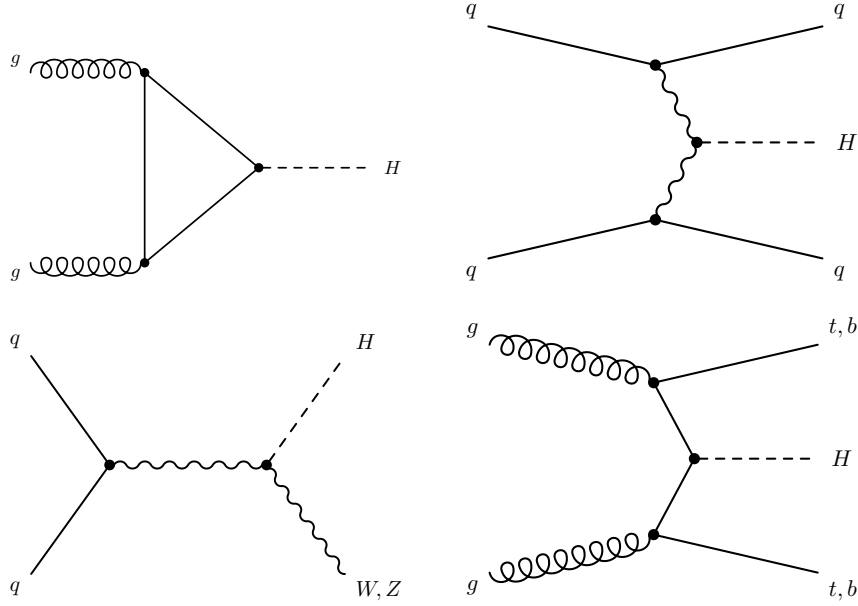
Figure 2.2   Feynman diagrams of the Higgs boson production at the LHC [14]. ggF (top left), VBF (top right), VH (bottom left) and ttH (bottom right).
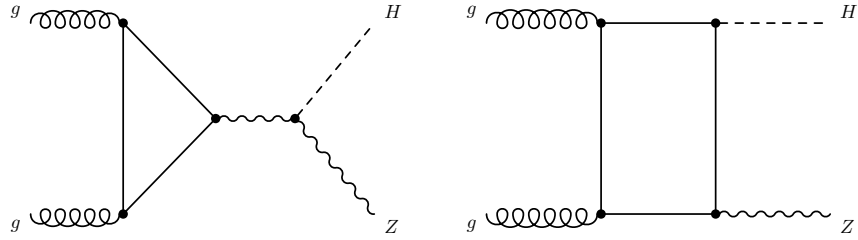

Figure 2.3   Feynman diagrams of $gg \rightarrow ZH$ signal [14]. Triangle (left) and box (right). Triangle is not top Yukawa coupling dependent and box is top Yukawa coupling dependent. Therefore, $gg \rightarrow ZH$ contribution is not fully proportional to top Yukawa coupling.

2.2.3 VH channel

In VH, there are 3 channels depending on number of reconstructed leptons:

- $ZH \rightarrow \nu\nu bb$ (0-lepton)
- $WH \rightarrow \ell\nu bb$ (1-lepton)
- $ZH \rightarrow \ell\ell bb$ (2-lepton)

The 2-lepton channel has a smaller signal yield compared to the other channels as shown in Table 2.3. However, fully reconstructed $Z \rightarrow \ell\ell$ allows to suppress the multi-jet and $t\bar{t}$ background strongly. Furthermore, it is possible to improve the Higgs mass resolution, by constraining the $\ell\ell bb$ to be balanced in the transverse plane (Kinematic Fit). This thesis mainly presents the 2-lepton analysis and also review the ATLAS combined results. The LHC Run2 proton-proton collisions data collected with the ATLAS detector is used. The center of mass energy is 13 TeV and the integrated luminosity is 36.1 fb^{-1}.
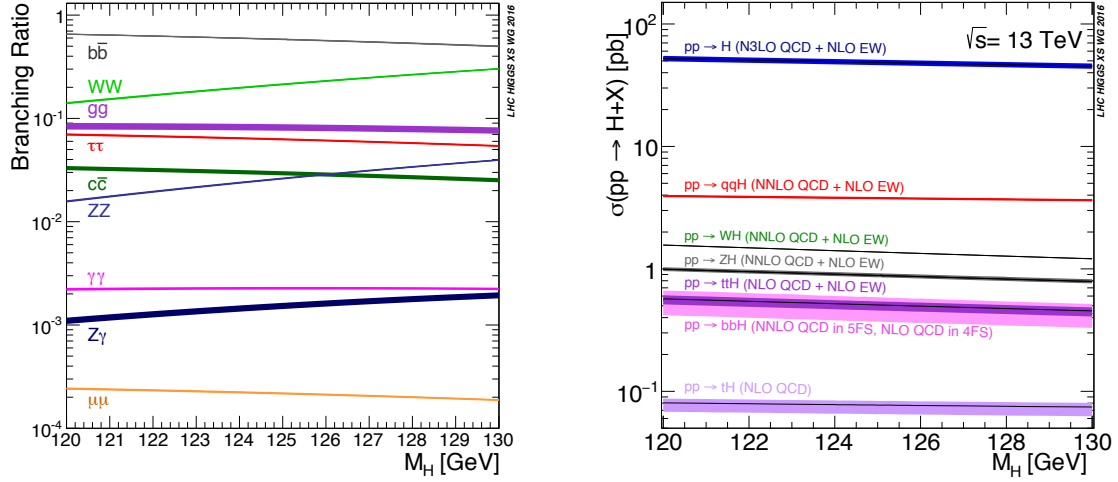
Figure 2.4   Higgs boson branching ratios (left) and production cross-sections (right) [24]. $H \to bb$ is the most dominant decay of the Higgs boson. It has a branching ratio of 58% in the SM. VH, the 3rd largest cross-section, is the most sensitive channels for $H \to bb$. It has about 1 pb cross-section in the SM.

	Expected	Observed
$H \to \gamma\gamma$	4.6σ (ATLAS) 5.3σ (CMS)	5.2σ (ATLAS) 4.6σ (CMS)
$H \to ZZ$	6.2σ (ATLAS) 6.3σ (CMS)	8.1σ (ATLAS) 6.5σ (CMS)
$H \to WW$	5.9σ (ATLAS) 5.4σ (CMS)	6.5σ (ATLAS) 4.7σ (CMS)
$H \to \tau\tau$	3.4σ (ATLAS) 3.9σ (CMS) 5.0σ (Combined)	4.5σ (ATLAS) 3.8σ (CMS) 5.5σ (Combined)
$H \to bb$	2.6σ (ATLAS) 2.5σ (CMS) 3.7σ (Combined)	1.4σ (ATLAS) 2.1σ (CMS) 2.6σ (Combined)

Table 2.2   Expected and observed significance of the Higgs boson in Run1 [9]. The expected is calculated from simulation and the observed is calculated from data. $H \to \gamma\gamma$, $H \to ZZ$, $H \to WW$ reached 5σ in ATLAS or CMS. $H \to \tau\tau$ reached 5σ in ATLAS and CMS combined results.

	Cross-section (σ) [fb]	Branching Ratio (BR)	$\sigma \times$ BR (σ_{tot}) [fb]
$ZH \to \ell\ell bb$	884	0.0336	29.71
$ZH \to \nu\nu bb$	884	0.2010	177.62
$WH \to \ell^+\nu bb$	840	0.1085	91.17
$WH \to \ell^-\nu bb$	533	0.1085	57.83

Table 2.3   Cross-section and branching ratio of VH channels [24]. Here σ_{tot} includes Drell-Yang like VH cross-section at NNLO QCD, NLO EW correction, and gluon induced signal cross-section (σ_{ggZH}). photon induced signal cross-section (σ_γ) is not included here, to show the cross-section without vector boson BR (σ). σ_{ggZH} contributes about 14%. NLO EW correction is about -5% for ZH and -7% for WH. σ_γ is about 0.4% for ZH and 3% for WH.

Chapter 3

The Large Hadron Collider and the ATLAS detector

The Large Hadron Collider (LHC) is used to test the SM, in proton-proton collisions at unprecedented center of mass energy. The ATLAS detector is a general purpose particle detector at the LHC. The $ZH \rightarrow \ell\ell bb$ signal is reconstructed as 2 electrons/muons and 2 b-jets in the final state. Therefore, all part of the ATLAS detector is important. In this chapter, the LHC is briefly summarized in Section 3.1, the ATLAS detector is summarized in Section 3.2, with emphasis on level-1 endcap muon trigger work at the beginning of Run2.

3.1 The Large Hadron Collider

CERN's accelerator complex is shown in Figure 3.1. The LHC proton injector chain consists of following [17]:

- LINAC2: Accelerate protons up to 50 MeV
- BOOSTER: Accelerate protons up to 1.4 GeV
- Proton Synchrotron (PS): Accelerate protons up to 25 GeV
- Super Proton Synchrotron (SPS): Accelerate protons up to 450 GeV

Design and performance of the LHC up to 2016 are summarized in Table 3.1. Beam energy was raised up to 6.5 TeV from 2015 (Run2). This corresponds to the center of mass energy of 13 TeV. Number of protons per bunch is about 1.1×10^{11} in Run2. Maximum number of bunches was limited at 2220, because of SPS vacuum leak in 2016 [25]. Bunch spacing is 25 ns from Run2. Crossing angle was reduced in September 2016 from 370 μrad to 280 μrad. This increased the luminosity about 25%. Peak luminosity reached 1.38×10^{34} cm^{-2}s^{-1} in 2016. Total delivered integrated luminosity was 4.2 fb^{-1} and 38.5 fb^{-1} in 2015 and 2016. Integrated luminosity recorded with the ATLAS detector and average interaction per crossing are summarized in Chapter 4.

The luminosity, L in (2.18), can be written as

$$L = \frac{N_b^2 n_b f_{\text{rev}} \gamma_r}{4\pi \varepsilon_n \beta*} F,$$ (3.1)

where N_b is number of protons per bunch, n_b is number of bunches, f_{rev} is the revolution frequency, γ_r is the relativistic gamma factor, ε_n is the normalized transverse beam emittance, $\beta*$ is the beta function at the collision point, F is the reduction factor as a function of crossing angle. The unit b is defined as

$$1\text{b} = 10^{-24}\text{cm}^2.$$ (3.2)

Therefore, to have integrated luminosity of 1 fb^{-1} with constant luminosity 1×10^{34} cm^{-2}s^{-1}, it will take 10^5 s $\approx$ 28 hours. Thus, 1 fb^{-1} / day is very good case in Run2.
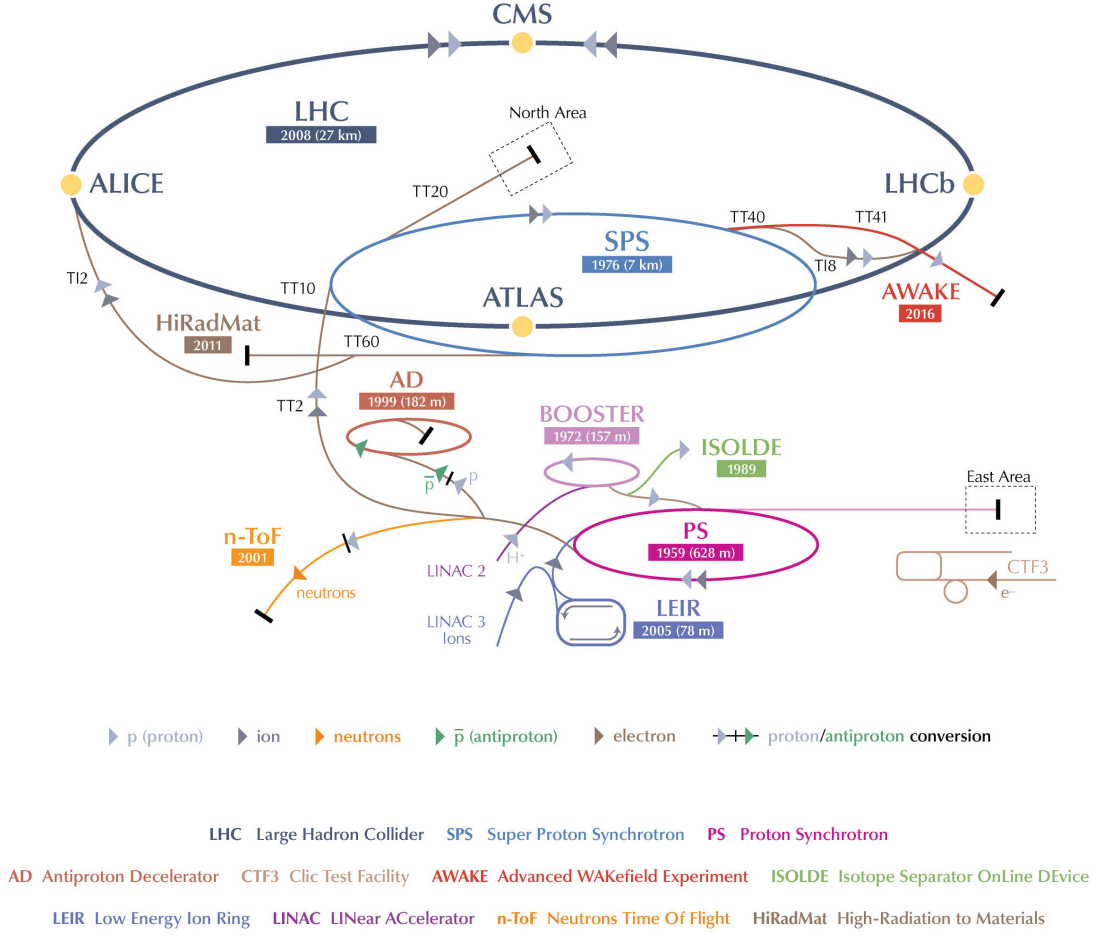
Figure 3.1   CERN's accelerator complex [26].   The LHC proton injector chain consists of LINAC2, BOOSTER, Proton Synchrotron (PS) and Super Proton Synchrotron (SPS) [17].

Table 3.1   Design and performance of the LHC up to 2016. [27] [25] [28]. is average at start of collisions. *The crossing angle was reduced in september 2016 from 370 μrad to 280 μrad.

|	Design	2010	2011	2012	2015	2016
Beam Energy [TeV]	7.0	3.5	3.5	4.0	6.5	6.5
Number of protons per bunch [10^{11}]	1.15	1.0	1.3	1.5	1.1	1.1
Maximum number of bunches	2808	368	1380	1380	2244	2220
Bunch spacing [ns]	25	150	50	50	25	25
Transverse normalized emittance ε_n [μm]	3.75	2.6	2.4	2.4	3.5	3.4
Crossing angle [μrad]	286	200	240	292	290	280*
β function (β*)	0.55	2.0–3.5	1.0–1.5	0.6	0.8	0.4
Peak luminosity [10^{34} cm^{-2}s^{-1}]	1.0	0.021	0.35	0.77	0.51	1.38
Integrated luminosity [fb^{-1}]	-	0.048	5.5	22.8	4.2	38.5
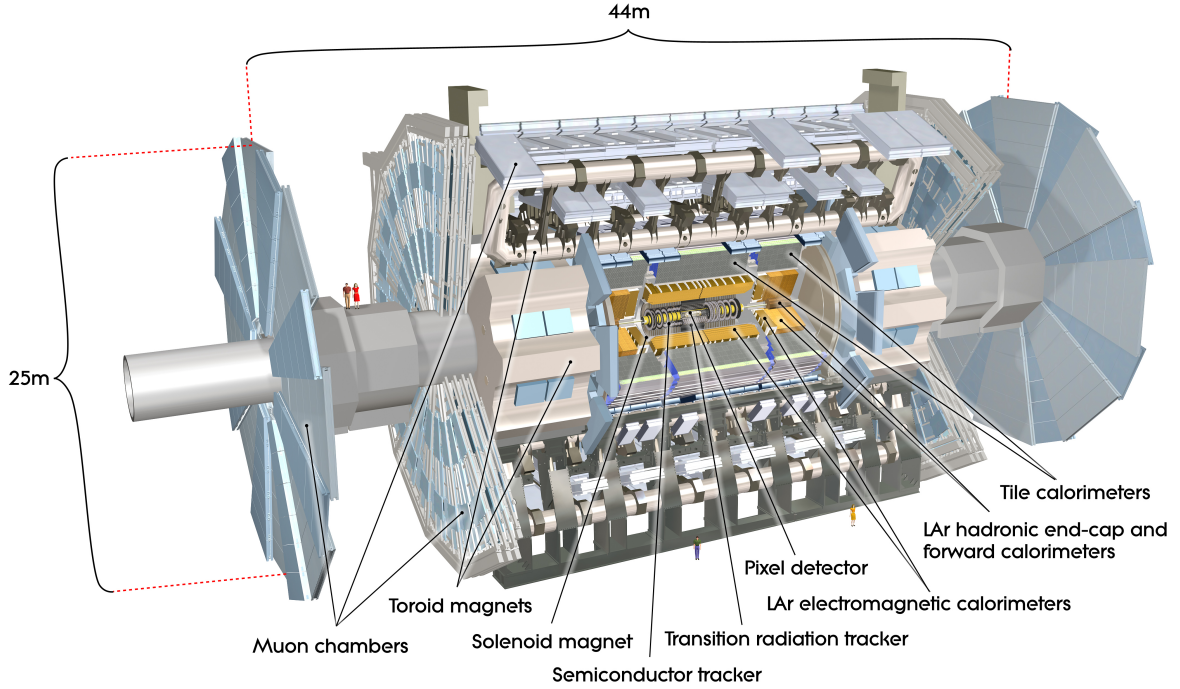
Figure 3.2   ATLAS detector [29]. ATLAS consists of Inner Detectors (ID), Calorimeter, Muon Spectrometer (MS), and Trigger and Data AcQuisition system (TDAQ). There are man and woman on the beam pipe. The author worked in that region in 2014–2015, to prepare level-1 endcap muon trigger for Run2.

3.2   The ATLAS detector

The ATLAS detector is shown in Figure 3.2. ATLAS consists of Inner Detectors (ID), calorimeter, Muon Spectrometer (MS), and Trigger and Data AcQuisition system (TDAQ). Required resolution and coverage of ATLAS is summarized in Table 3.2 The $ZH \rightarrow \ell\ell bb$ signal has 2 leptons and 2 b-jets in final states. The 2 leptons are detected using ID, calorimeter and MS. The 2 b-jets are detected using ID and calorimeter [*1].

In this section, ID, calorimeter, MS and TDAQ are summarized in Subsection 3.2.1, 3.2.2, 3.2.3 and 3.2.4 respectively.

3.2.1   Inner Detector

The ID is used for track and vertex reconstruction and momentum measurement of charged particle. Fine granularity is required since track density is large around the interaction point (IP). About 1000 particles come out from the IP every 25 ns in $|\eta| < 2.5$. A solenoid magnet is used for the ID. It provides 2 T magnetic field. The ID is show in Figure 3.3. 3 tracking detector technologies are used.

[*1] ATLAS uses a xyz-coordinate from the IP. x-axis points to the center of the LHC. y-axis points to the sky. z-axis points to the Airport side (A-side). Negative direction of z axis points to Chary's pub side (C-side). Other coordinate and variables are also used. r is distance from z-axis. ϕ is azimuthal angle around z-axis. θ is polar angle. η is pseudo-rapidity defined as $\eta = \ln\tan(\theta/2)$. ΔR is distance in (η,ϕ) coordinate defined as $dR = \sqrt{d\phi^2 + d\eta^2}$. p_T is transverse momentum defined as $p\sin\theta$. E_T is transverse energy defined as $E\sin\theta$.

Table 3.2   Required resolution and coverage of ATLAS [29]. σ is the resolution. p_{T} is the transverse momentum. E is the energy. η is the pseudo-rapidity.

Detector component	Required resolution	Measurement ($|\eta|$)	Trigger ($|\eta|$)
Inner detector	$\sigma_{p_{\mathrm{T}}}/p_{\mathrm{T}} = 0.05\% p_{\mathrm{T}} \oplus 1\%$	< 2.5	-
Electromagnetic calorimeter	$\sigma_E/E = 10\%/\sqrt{E} \oplus 0.7\%$	< 3.2	< 2.5
Hadronic calorimeter (barrel and endcap)	$\sigma_E/E = 50\%/\sqrt{E} \oplus 3\%$	< 3.2	< 3.2
Hadronic calorimeter (forward)	$\sigma_E/E = 50\%/\sqrt{E} \oplus 3\%$	3.1–4.9	3.1–4.9
Muon spectrometer	$\sigma_{p_{\mathrm{T}}}/p_{\mathrm{T}} = 10\%$ at $p_{\mathrm{T}} = 1$ TeV	< 2.7	< 2.4

Silicon pixel detectors (**Pixels**) is the innermost detector in ATLAS. There are 3 layers in the barrel region, and 3 disks in each side of the endcap region. The pixel size is 50×400 $\mu\mathrm{m}^2$ in $R - \phi \times$ z. In total there are 80.4 M channels for the pixel detector. The innermost layer of the pixel (b-layer) is important for the secondary vertex measurement. From Run2, additional insertable b-layer (IBL) is used [30]. The IBL and new software improved the track and vertex reconstruction. Particularly, the b-jet identification, as summarized in Section 5.5, achieved a few times better light and c-jet rejection in Run2 [31, 32].

SiliCon microstrip Tracker (**SCT**) is placed after the Pixels. There are 4 layers in the barrel region, and 9 disks in each side of the endcap region. In total there are 6.3 M channels for SCT. SCT consists of 6.4 cm daisy chained sensors with a strip pitch of 80 μm. Each SCT layer is made of 2 strips to measure the hit space point. One strip is parallel to the beam pipe and the other strip rotated by 40 mrad.

Transition Radiation Tracker (**TRT**) provides information of transition radiation. The information is important not only for tracking but also for electron identification. The radiation energy is known to be high for electron. The transition radiation material is made of polypropylene. The straw diameter is 4 mm and the anode wire diameter is 31 μm. The cathode is operated at about -1530 V. The gas is Xenon-based and cheaper Ar-based in some channels from Run2 [33]. There are 73 layers in the barrel region, and 80 disks in each side of the endcap region. In total there are 351 k channels for the TRT. In the barrel region, the length of the straw is 144 cm, and the wires are divided at $\eta = 0$. In endcap, the straws are 37 cm and arranged radially.

3.2.2   Calorimeter

Calorimeters with active material and absorber are used, to measure the energy of electromagnetic and hadronic showers. The calorimeter is shown in Figure 3.4. It covers $|\eta| < 4.9$. 4 types of calorimeters are used.

LAr electromagnetic barrel/endcap calorimeter (**EM**) is a lead-LAr detector. Lead is absorber and LAr is active material. Barrel covers $|\eta| < 1.475$ and endcap covers $1.375 < |\eta| < 3.2$. Total thickness is more than 20 radiation length [*2]. For $|\eta| < 2.5$, there are 3 segments in depth. For $|\eta| < 1.8$, a presampler detector is used to correct energy loss before the calorimeter. There are about 110 k channels for barrel and 64 k channels for endcap, including the presampler.

[*2]   The radiation length (X_0) is a distance to reduce energy of high energy electron by $1/e$.

6.2m

2.1m

Barrel semiconductor tracker

Pixel detectors

Barrel transition radiation tracker

End-cap transition radiation tracker

End-cap semiconductor tracker

R = 1082mm

TRT

R = 554mm
R = 514mm
R = 443mm
SCT
R = 371mm
R = 299mm

R = 122.5mm
Pixels   R = 88.5mm
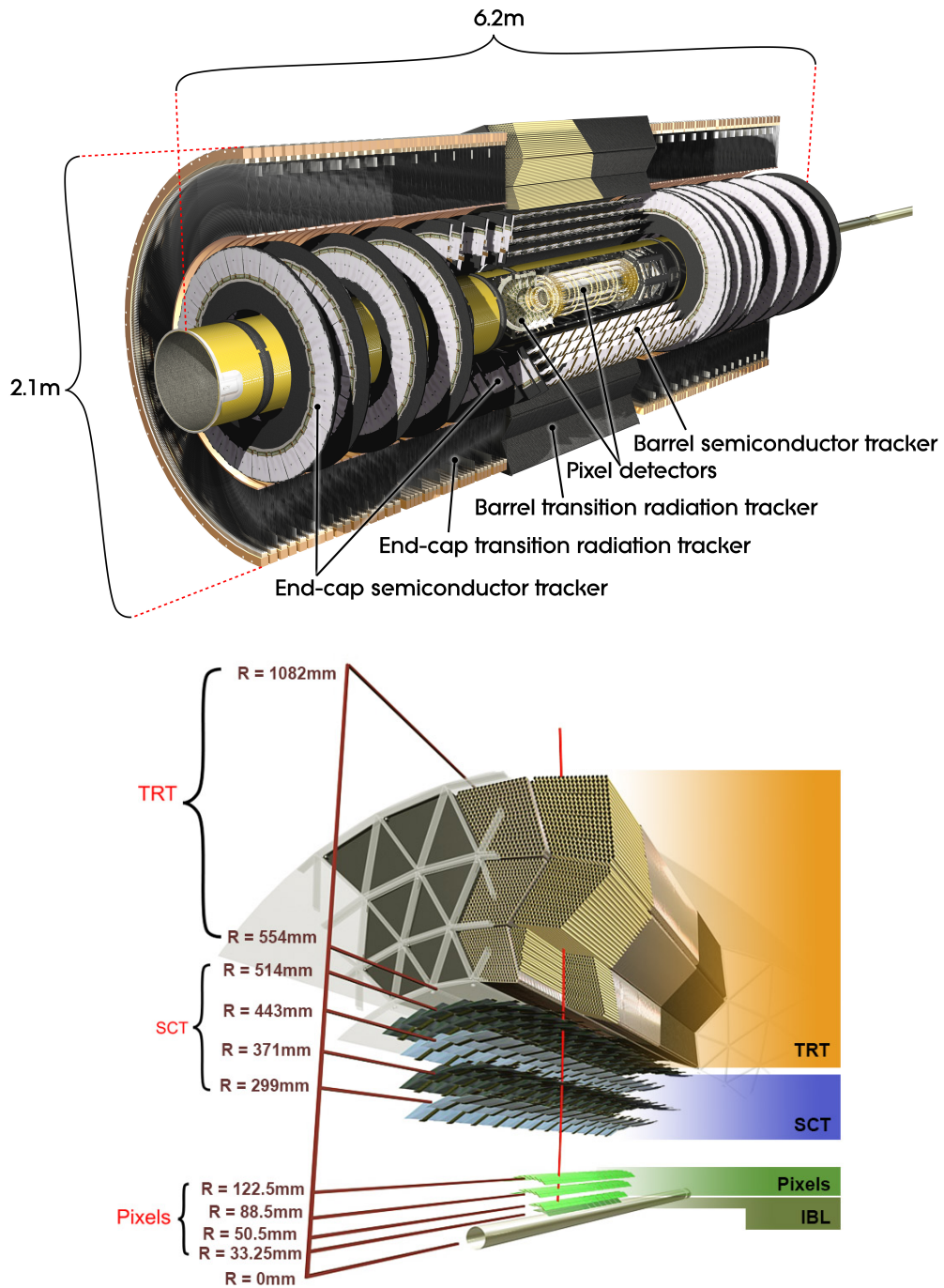R = 50.5mm
R = 33.25mm
R = 0mm

TRT

SCT

Pixels

IBL

Figure 3.3   Inner Detector (ID) [29, 30]. Overview (top) and barrel closeup (bottom). ID consists of the insertable b-layer (IBL). Pixel detectors (Pixels), semiconductor tracker (SCT), and Transition Radiation Tracker (TRT).
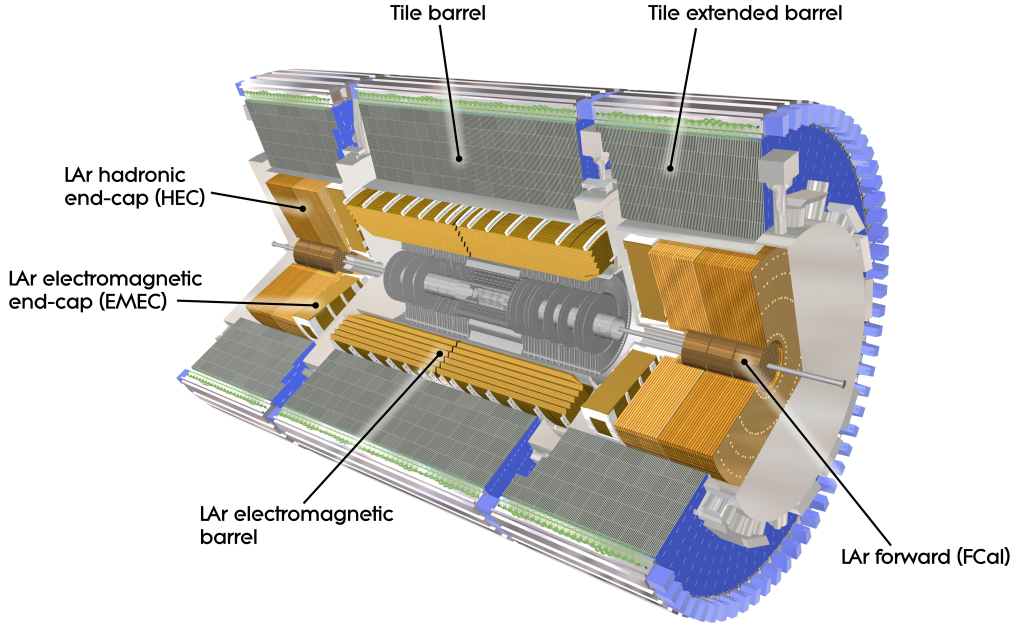
Figure 3.4   Calorimeter [29]. There are 2 types of calorimeter: electromagnetic (LAr) calorimeter and hadronic (Tile) calorimeter.

Tile hadronic barrel/extended barrel calorimeter(**Tile**) is a steel-scintillator detector placed after the EM calorimeter. Steel is absorber and scintillator is active material. Barrel covers $|\eta| < 1.0$ and extended barrel covers $0.8 < |\eta| < 1.7$. There are about 6 k channels for barrel and 4 k channels for extended barrel. The depth is segmented in 3 layers. The total thickness is about 10 interaction length [*3].

LAr hadronic endcap calorimeter (**HEC**) is located behind the EM endcap calorimeter. It covers $1.5 < |\eta| < 3.2$, overlapping the Tile hadronic extended barrel calorimeter and LAr hadronic forward calorimeter. There are about 5.6 k channels for HEC. The depth is segmented in 2 layers. 25 mm and 50 mm copper plates are used for inner layers and outer layers. The LAr gaps are 8.5 mm.

LAr electromagnetic/hadronic forward calorimeter (**FCal**) covers $3.1 < |\eta| < 4.9$. There are about 3.5 k channels for FCal. The depth is about 10 interaction length. 3 modules are used. The 1st one is made of copper for electromagnetic measurements. The others are made of tungsten for hadronic measurements.

3.2.3   Muon Spectrometer

MS is used to measure muon momentum. Muon tracks are bent in the magnetic field. Difference from infinite momentum track (straight line) is used to measure the momentum. The toroid magnets are used for MS. There are 1 barrel toroid magnet and 2 endcap toroid magnets. Magnetic field strength of the endcap and barrel toroids

---

[*3] The interaction length (λ_{int}) is a distance to reduce number of charged particles in a hadron shower by $1/e$.

are 1 T and 0.5 T. The MS is shown in Figure 3.5. There are 4 types of detector in MS.

Monitored Drift Tube (**MDT**) is used for precise muon tracking. It covers $|\eta| < 2.7$ with drift tube detectors. The innermost layer covers $|\eta| < 2.0$. There are 1150 chambers and 354 k channels for MDT. Cathode tube diameter is 29.970 mm. Central anode wire diameter is 50 μm. Average position resolution per tube is 80 μm. High-Voltage of about 3 kV is applied to the wire. The gas is Ar:CO$_2$ (93:7) at about 3 atmospheric pressure. Maximum drift time is about 700 ns.

Cathode Strip Chambers (**CSC**) is a multiwire chamber. It covers $2.0 < |\eta| < 2.7$ for precision tracking, in the first layer instead of MDT. The rate limit for safe operation is 150 Hz/cm^2 for MDT but 1000 Hz/cm^2 for CSC. There are 32 chambers and 31 k channels for CSC. The wire pitch is 2.5 mm and the anode cathode spacing is also 2.5 mm. The readout pitch is about 5 mm. Position resolution is 80 μm per plane. Anode wire diameter is 30 μm. High-Voltage of about 1900 V is applied to the wire. Gas is Ar:CO$_2$ (80:20). Total ionization is about 90 ion pairs. Maximum drift time is about 40 ns.

Resistive Plate Chambers (**RPC**) is a parallel electrode-plate gas detector. It covers $|\eta| < 1.05$ for trigger and ϕ measurement. There are 606 chambers and 373 k channels for RPC. The resistive plate is made of phenolic-melaminic plastic laminate. 2 plates are placed in parallel with a distance of 2 mm. Metallic strip is used to readout z-*phi* position of hits. Readout pitch is 23–35 mm. The electric field strength in the 2 mm gap is about 4.9 kV/mm. The gas is C$_2$H$_2$F$_4$:Iso-C$_4$H$_1$0:SF$_6$ (94.7:5:0.3). Signal width is about 5 ns.

Thin Gap Chambers (**TGC**) is used for the trigger, and also for measurement of ϕ, to complement the MDT that measures r. It covers $1.05 < |\eta| < 2.7$ with multiwire chambers. The trigger is for $1.05 < |\eta| < 2.4$. Figure 3.6 shows the cross-section of the MS. The inner station is called as Small Wheel (SW) and the middle station is called as Big Wheel (BW). Figure 3.7 shows the TGC BW in the ATLAS cavern. There are 3588 chambers and 318 k channels for TGC. Figure 3.8 shows the TGC triplet and doublet. The triplet is used for the 1st layer of the middle station (M1). The doublet is used for the inner station layer, and the 2nd and 3rd layer of the middle station (M2 and M3). Figure 3.9 shows the TGC structure. Gold coated Tungsten wires are used to measure r of the hits. The Wire to cathode distance is 1.4 mm. The Wire to wire distance is 1.8 mm. The Wire diameter is 50 μm. The Wire potential is $\sim$2.9 kV. To achieve required momentum resolution within limited band width, the wires are grouped from 6 to 31 depending on η. The granularity is from 10.8 mm to 55.8 mm. Graphite is painted on 1.6 mm G-10 board. Cuprum strip is used to measure the ϕ. The granularity is 2–3 mrad. The gas is CO$_2$:n-pentane (55:45). CO$_2$ is the ionizing gas and the n-pentane is the quencher. The angle of a track from the IP is always greater than 10 degree. Therefore, 99% of signal is detected within in 25 ns.

3.2.4   Trigger and data acquisition

Trigger and data acquisition system (TDAQ) is used to trigger and record interesting events. Several key components and structure of the system is summarized as follows.

Hardware based Level1 trigger (**L1**) **and software based High Level Trigger** (**HLT**) is used to trigger interesting events from the multi-jet background events. L1 selects events up to 100 kHz level from the 40 MHz
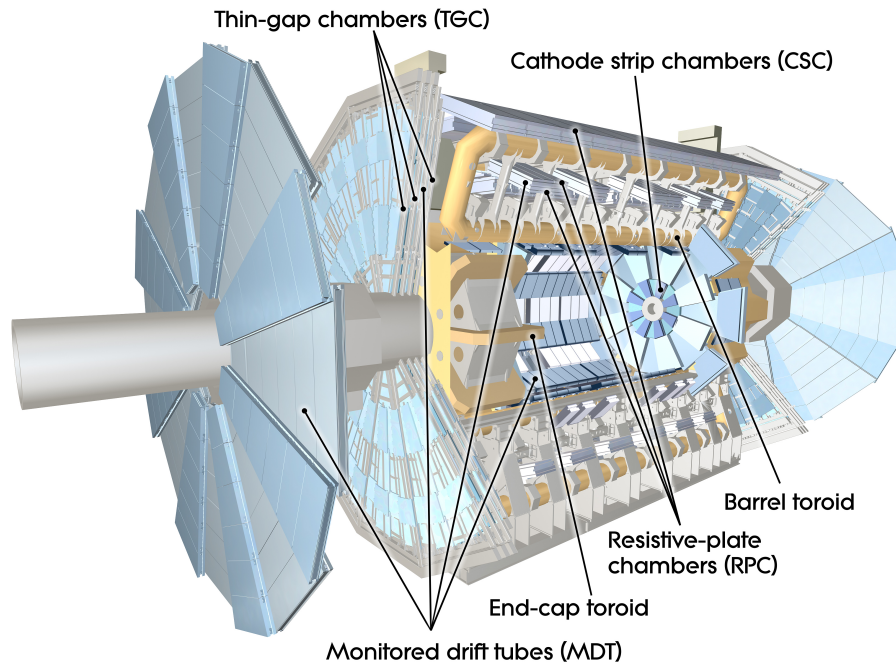
Figure 3.5   Muon Spectrometer [29]. The MS consists of Monitored Drift Tube (MDT), Cathode Strip Chambers (CSC), Resistive Plate Chambers (RPC), Thin Gap Chambers (TGC).
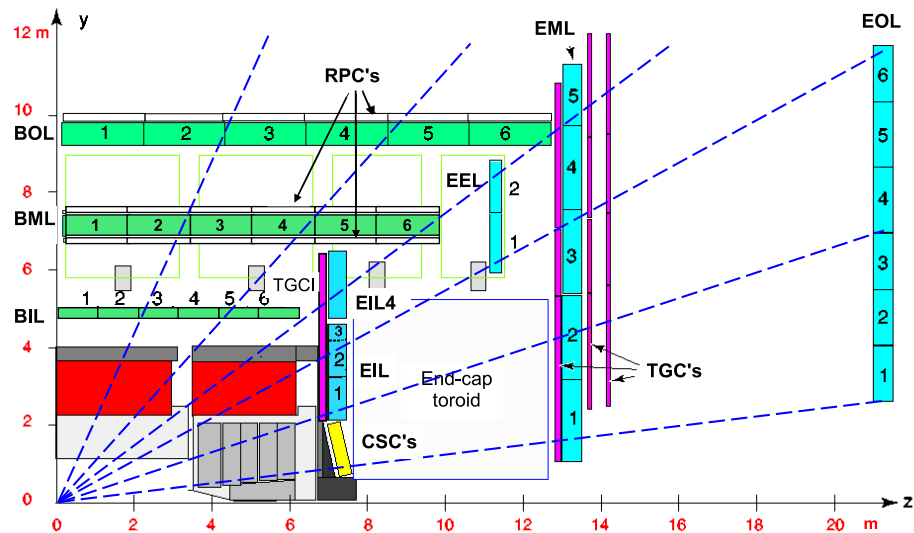

Figure 3.6   Cross-section of the Muon Spectrometer [29]. Dashed line illustrates the infinite momentum track. The TGC inner station is placed at ~7 m in z-axis. The TGC middle station is placed at ~14 m in z-axis.
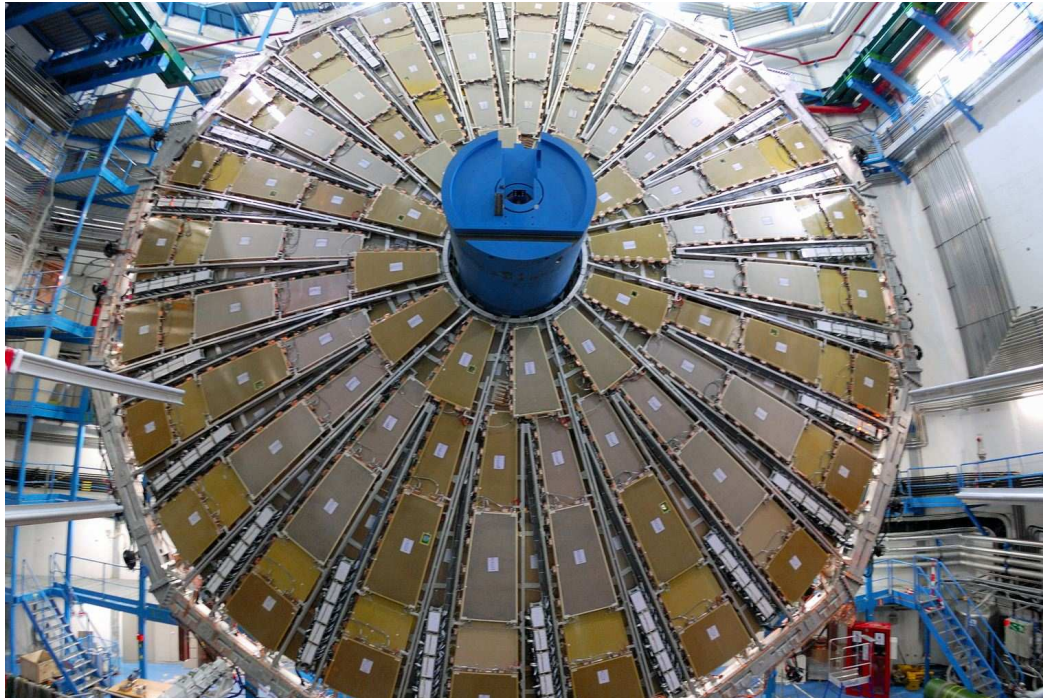
Figure 3.7   TGC Big wheel in the ATLAS cavern [29]. There are 12 sectors in each side of end-cap. A chamber covers 7.5 (15) degree in end-cap (forward) part.
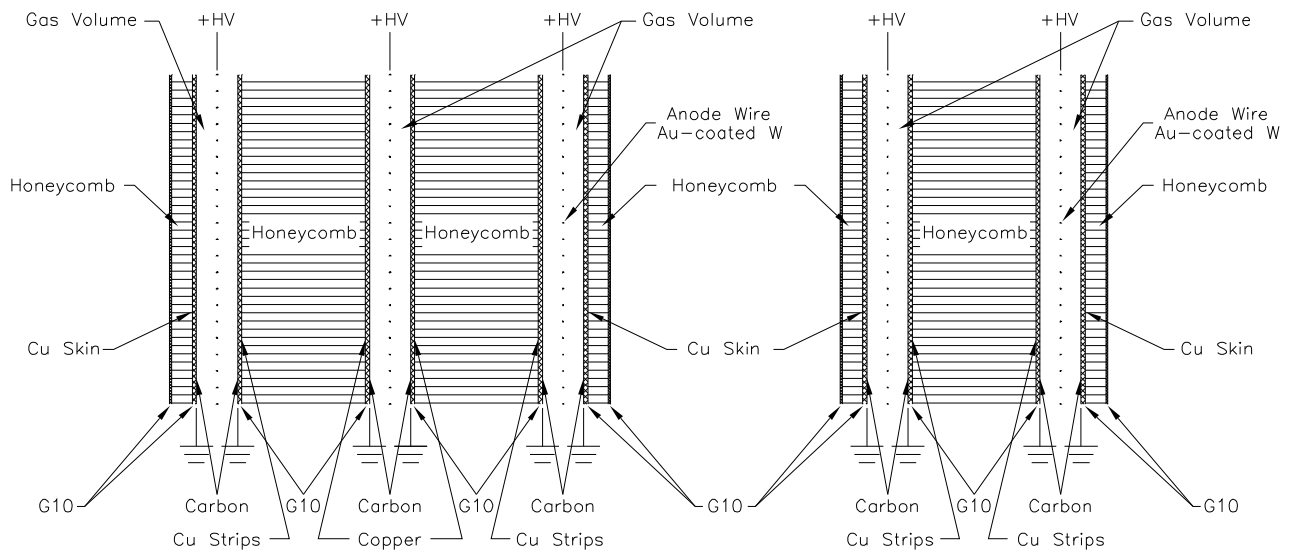

Figure 3.8   TGC triplet (left) and doublet (right) [29]. The triplet has 3 wire chambers and and 2 strip layers. The doublet has 2 wire chambers and and 2 strip layers.
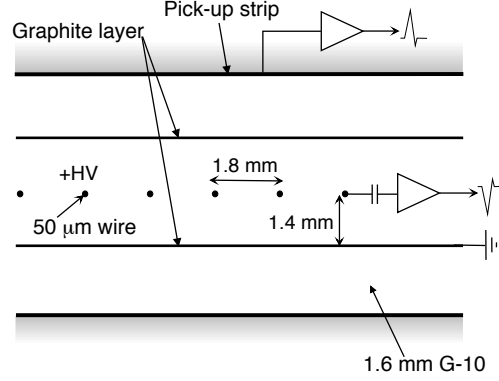
Figure 3.9   TGC structure [29]. Gold coated Tungsten wires are used to measure r of the hits. The Wire to cathode distance is 1.4 mm. The Wire to wire distance is 1.8 mm. The Wire diameter is 50 μm. The Wire potential is $\sim$2.9 kV.

bunch crossing. It uses limited information of the detector to make decision within 2.5 μs. The results from muon triggers and calorimeter triggers are considered in Central Trigger Processor (CTP). CTP makes final L1 decision, and send L1 Accept (L1A) signal to all sub-detectors. HLT selects events up to 1000 Hz level from the L1 triggers. Offline analysis calibration is performed and decision is made within 4 s.

Timing Trigger Control system (**TTC**) **and Detector Control System** (**DCS**) are provided for all sub-detectors. TTC distributes the L1A and LHC 40 MHz clock and reset signals. DCS controls, monitors, and archives operational parameters. For example Low-Voltage (LV) and High-Voltage (HV), gas, cooling, temperature, humidity, and magnetic field. The DCS communicates with LHC, CERN technical services, ATLAS magnet and detector safety system.

Data AcQuisition (**DAQ**) is realized by a readout scheme summarized as follows. Each sub-detectors have their own front-end electronics and ReadOut Drivers (ROD). Front-end includes components such as, analogue or analogue-to-digital processor, L1 buffer to hold data until the L1A, derandomising buffer to hold data after the L1A, and dedicated link to the ROD. For the front-end to ROD link, an optical link (g-link) is used, since the distance from cavern to the counting room is about 100 m. ROD gathers data from front-end and builds a common event format, and send it to ReadOut Buffer (ROB) in ReadOut System (ROS) via a common optical link (s-link). It also follows a common error/recovery mechanism. After HLT, data is stored in a storage in CERN computer center.

TGC trigger and readout scheme is summarized in Figure 3.10. It requires hit coincidence to select high p_{T} muon events. However, most of triggers are known to be fake triggers originating from protons from beam pipe and low p_{T} muon because of limited momentum resolution. Therefore, TGC had to reduce fake triggers for Run2 data taking. In 2015, during the Run2 commissioning rush, the inner coincidence was enabled, and fake trigger rate was reduced about 20% as shown in Figure 3.11. Thus, Run2 data taking became possible. After successful operation in Run1, tens of TGC chambers were broken. In 2014 and 2015, many part of the system was fixed. This includes chambers, electronics, connection, power supply and cooling system. Thus, TGC achieved about 90% efficiency as shown in Figure 3.12.
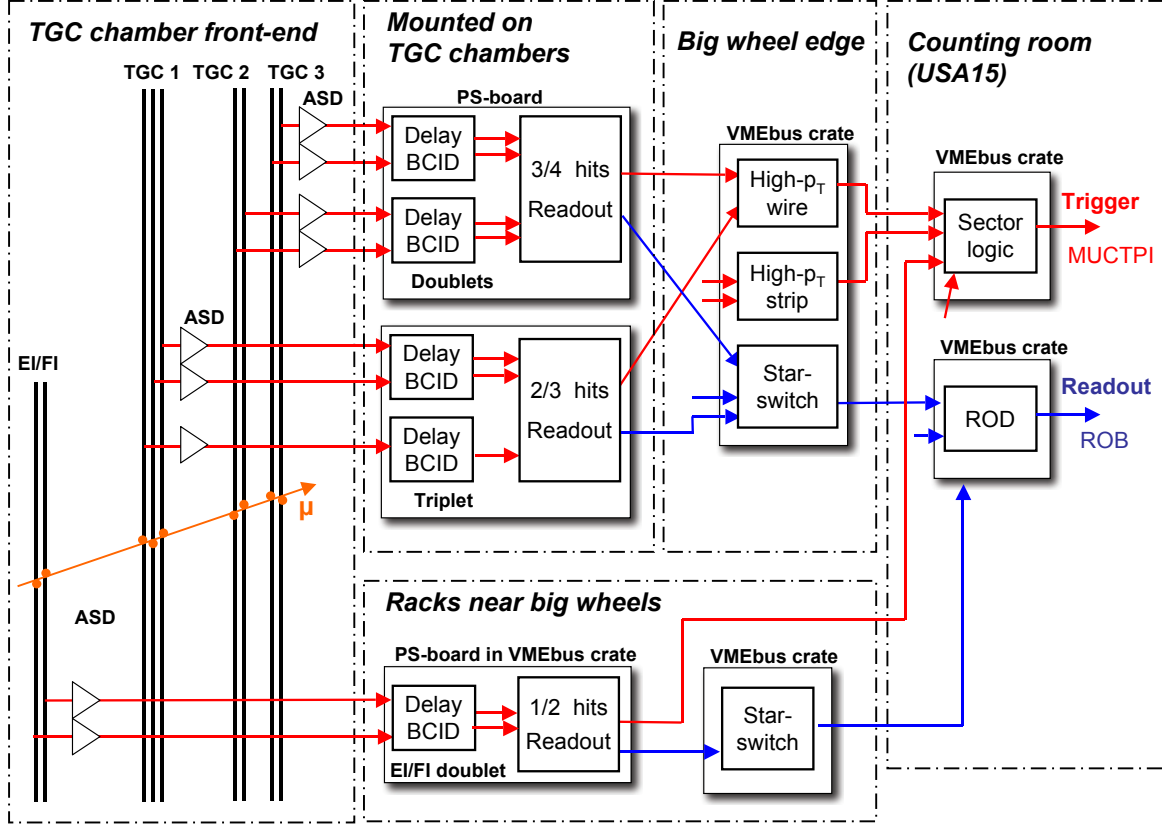
Figure 3.10 TGC trigger and readout scheme [29]. Red line illustrates the trigger scheme. At first, The signal is digitized in the Amplifier Shaper Discriminator (ASD). Then, in the PS board, the doublet 3/4 coincidence and the triplet 2/3 coincidence is required for wire and strip separately. Then, the doublet-triplet coincidence is required for wire and strip separately, in the High-p_T board on the Big Wheel edge. Finally, the wire-strip coincidence and the inner coincidence is required in the Sector Logic (SL) board in the counting room (USA15), and the results are send to the Central Trigger Processor (CTP) via MUon CTP Interface (MUCTPI). Blue line illustrates the readout scheme. When the PS-board receives the Level1 Accept (L1A) signal from the CTP via the Timing Trigger Control (TTC), the hit data is readout form the L1 buffer in the PS-board. The Star-SWitch (SSW), gathers, suppresses, and send the data to the ReadOut Driver (ROD) in the USA15. The ROD format the data into ATLAS format, and send data to the ReadOut Buffer (ROB). Low Voltage Differential Signaling (LVDS) connection is used in the cavern. An optical connection (G-link) is used for the connection between the SSW and the ROD, that is ∼100 m from the cavern to the USA15.
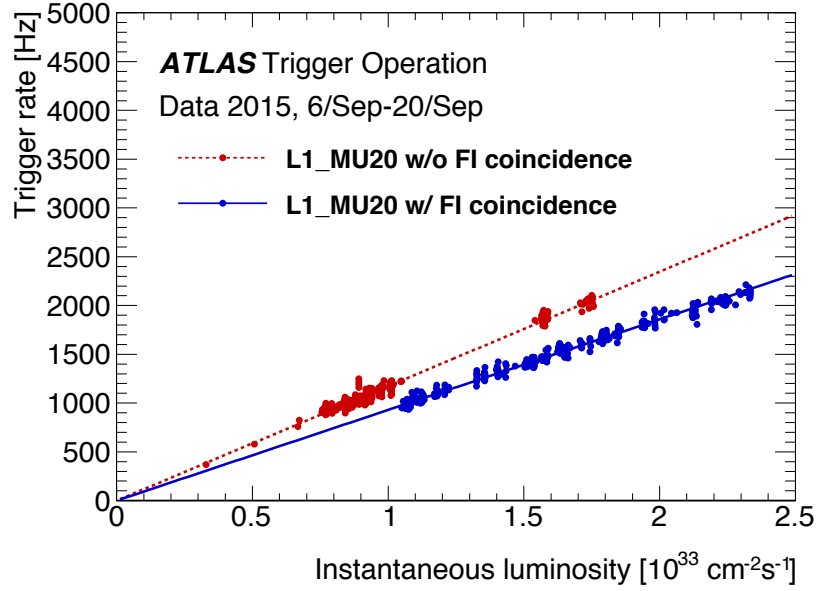
Figure 3.11 Trigger rate reduction by the inner coincidence [34]. Red shows trigger rates without the inner coincidence. Blue shows trigger rates with the inner coincidence. Fake trigger was reduced about 20%, mainly rejecting protons from beam pipe.

Figure 3.12 p_T turn on curve of L1 endcap muon trigger at the beginning of Run2 [35]. Black shows data in 2015 and red shows data in 2016. The efficiency is measured using $Z \to \mu\mu$ events. TGC achieved about 90% efficiency in the plateau region.

Chapter 4

Data and simulated samples

Data and Monte Carlo (MC) simulated samples are used to estimate background and extract the signal strength. The results are affected by statistical and systematic uncertainties on data and simulated samples. Therefore, it is important to have data and simulated samples as much as pos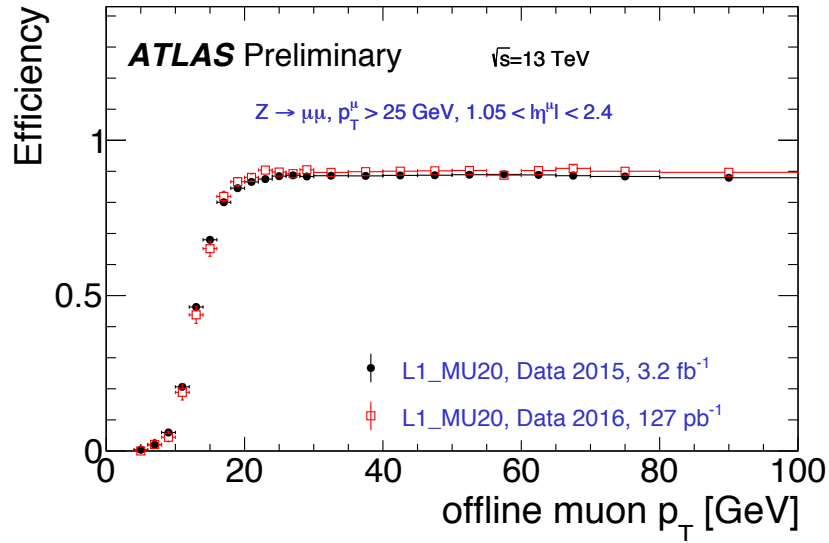sible and as accurate as possible. In this chapter, data used in this analysis are summarized in Section 4.1, simulated samples are listed in Section 4.2. Alternative samples used to assess systematic uncertainties are discussed in Section 9.2.

4.1 Data

The LHC Run2 proton-proton collisions data collected with the ATLAS detector is used in this analysis. The center of mass energy is 13 TeV and the integrated luminosity is 36.1 fb^{-1}. Figure 4.1 shows the integrated luminosity by day in 2015 and 2016. The integrated luminosity is 3.2 fb^{-1} in 2015, and 32.9 fb^{-1} in 2016, after requiring that all detectors were running. Figure 4.2 shows the peak luminosity in 2015 and 2016. The peak luminosity reached 0.5×10^{34} cm^{-2}s^{-1} in 2015, and 1.38×10^{34} cm^{-2}s^{-1} in 2016. Figure 4.3 shows the mean number of interactions per crossing (μ). The number is calculated for each bunch as

$$\mu = L_{\text{bunch}} \times \sigma_{\text{inel}}/f_{\text{r}}, \tag{4.1}$$

where L_{bunch} is per bunch instantaneous luminosity, σ_{inel} is considered to be 80 mb for 13 TeV proton-proton collisions, and f_{r} is the LHC revolution frequency. Average number of μ was 14 in 2015, and 25 in 2016.

4.2 Simulated samples

Simulated samples used in this analysis are summarized in Table 4.1. All samples are simulated with the ATLAS full simulation using the GEANT4 [36], and normalized to the most accurate cross-sections available at the time. Pile-up from the same or nearby bunch crossing are overlaid to the events. The pile-up events are simulated as soft QCD events with PYTHIA8.186 [37] with A2 [38] set of Underlying Event (UE) tune and MSTW2008LO PDF [20]. The events are reweighted to make the same mean number of interactions per crossing distribution as data, as shown in Figure 4.3. Such MC reweights to data are also applied for each object reconstruction and identification efficiency. The decay of b and c hadrons is described by the EVTGEN v1.2.0 [39] or SHERPA [40].
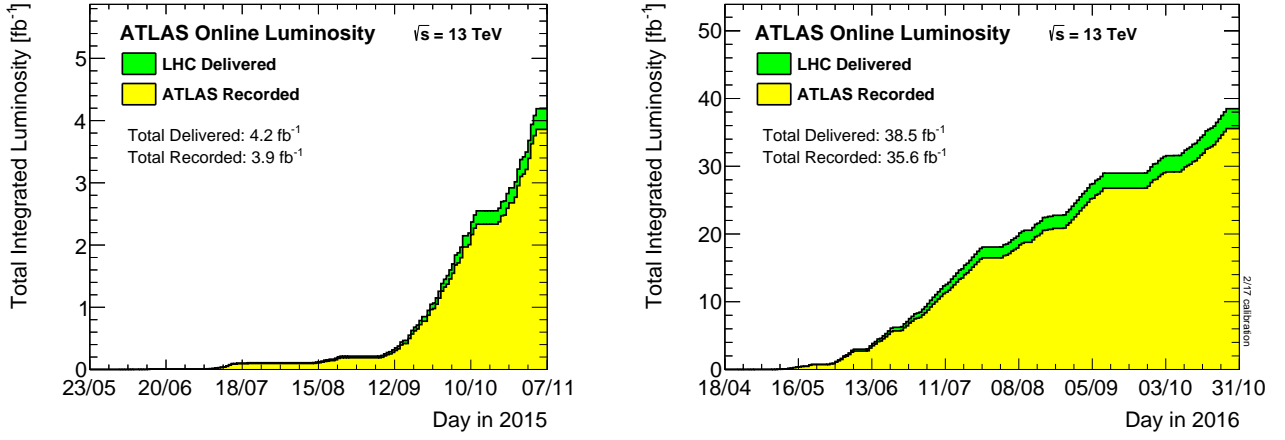
Figure 4.1   Integrated luminosity by day in 2015 (left) and 2016 (right) [28]. The integrated luminosity is 3.2 fb^{-1} in 2015, and 32.9 fb^{-1} in 2016, after requiring that all detectors were running.
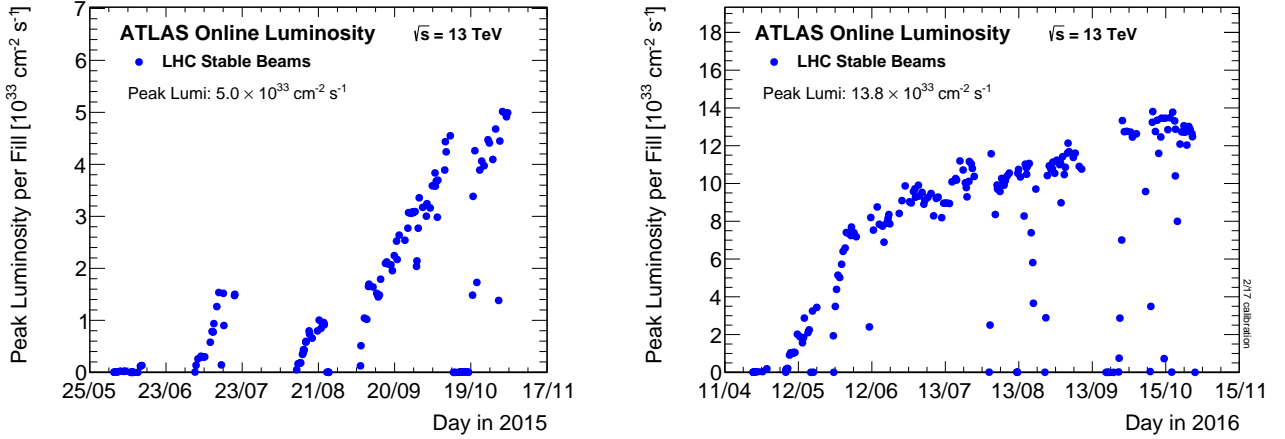
Figure 4.2   Peak luminosity by fill in 2015 (left) and 2016 (right) [28]. Peak luminosity was 0.5×10^{34} cm^{-2}s^{-1} in 2015, and 1.38×10^{34} cm^{-2}s^{-1} in 2016.

Figure 4.3   Mean number of interactions per crossing in 2015 (left) and 2016 (right) [28]. Average number of interactions per crossing was 14 in 2015, and 25 in 2016. Structure in the distribution is from changes in the LHC configuration as mentioned in Section 3.1.

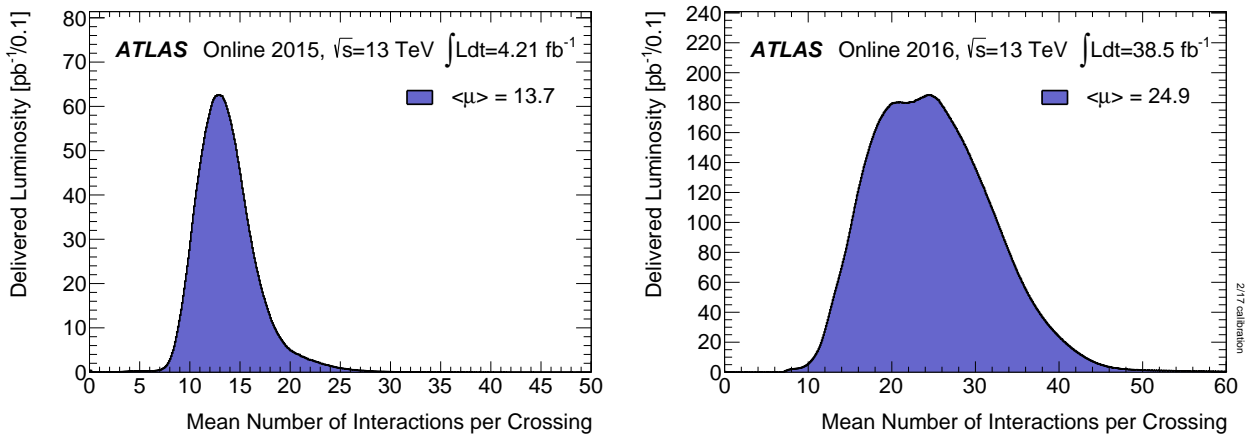|	Process	ME generator	PDF	PS	UE	Cross-section
Signal	$qq \to ZH$	Powheg-Box v2 +GoSam+MiNLO	NNPDF3.0NLO	Pythia8.212	AZNLO	NNLO(QCD) +NLO(EW)
	$gg \to ZH$	Powheg-Box v2	NNPDF3.0NLO	Pythia8.212	AZNLO	NLO+NLL
Top	$t\bar{t}$	Powheg-Box v2	NNPDF3.0NLO	Pythia8.212	A14	NNLO+NNLL
	s-channel	Powheg-Box v1	CT10	Pythia6.428	P2012	NLO
	t-channel	Powheg-Box v1	CT10	Pythia6.428	P2012	NLO
	Wt	Powheg-Box v1	CT10	Pythia6.428	P2012	NLO
V+jets	$Z \to \ell\ell$	Sherpa2.2.1	NNPDF3.0NNLO	Sherpa2.2.1	Default	NNLO
	$W \to \ell\nu$	Sherpa2.2.1	NNPDF3.0NNLO	Sherpa2.2.1	Default	NNLO
Diboson	ZZ	Sherpa2.2.1	NNPDF3.0NNLO	Sherpa2.2.1	Default	NLO
	WZ	Sherpa2.2.1	NNPDF3.0NNLO	Sherpa2.2.1	Default	NLO
	WW	Sherpa2.1.1	CT10	Sherpa2.2.1	Default	NLO

Table 4.1   Simulated samples used in this analysis. ME generator , PDF, PS, and UE are the Matrix Element generator, the Parton Distribution Functions, the Parton Shower and hadronization model, and the Underlying Event model respectively. NNPDF3.0NLO means that the events are generated using NNPDF3.0NLO PDF set, and reweighted to PDF4LHC15NLO PDF set using Powheg-Box v2, to follow the PDF4LHC recommendations [41].

4.2.1   Signal

The quark induced signal ($qq \to ZH$) is generated with Powheg-Box v2 + GoSam + MiNLO [42]. Powheg method interfaces parton-shower generators with NLO QCD calculation [43]. Powheg-Box implements NLO calculations in shower programs [44]. GoSam automates calculation of one-loop amplitudes [45]. MiNLO consistently account for the kinematic scales [46]. The gluon induced signal ($gg \to ZH$) is generated with Leading Order (LO) Powheg-Box v2. A correction factor as a function of p_T^V is applied for $qq \to ZH$, to take account of EW correction at NLO, using Hawk [47]. The samples are required to have $H \to bb$ and $Z \to \ell\ell$ ($\tau\tau$ is also included). Higgs boson mass is set at 125 GeV. AZNLO UE tune is used to model the UE [48]. Cross-section of $pp \to ZH$ is calculated at NNLO (QCD) and NLO (EW) [49, 50, 51, 52, 53]. Cross-section of $gg \to ZH$ is calculated at NLO and next-to-leading logarithm (NLL) [54, 55, 56, 57, 58]. Cross-section of $qq \to ZH$ is calculated from $pp \to ZH$ cross-section subtracting $gg \to ZH$ cross-section. About 1–4 M events are generated for signal samples.

4.2.2   Top

$t\bar{t}$ is generated with Powheg-Box v2 [59]. A14 UE tune is used to model the UE [60]. Single top (s-channel, t-channel, Wt) are produced with Powheg-Box v1 [61, 62]. P2012 UE tune is used [63]. Top quark mass is set at 172.5 GeV. The samples are required to have at least a W boson decaying leptonically. Cross-section of $t\bar{t}$ is calculated at NNLO and resummation of soft gluon emmission at next-to-next-leading logarithm (NNLL) with Top++2.0 [64]. Cross-section of single-top is calculated at NLO [65, 66, 67]. About 60 M events are generated for $t\bar{t}$ samples with at least 1 W boson decaying leptonically. About 20 M events are generated for $t\bar{t}$ samples with 2 W boson decaying leptonically. About 1–10 M events are generated for single top samples.

4.2.3 $V+$jets

$V+$jets are simulated with Sherpa2.2.1 [40, 68] interfaced with NNPDfs [69]. Matrix Elements (ME) are calculated with Open-Loops [70] and Comix [71]. In order to have a good modeling at large number of jets, up to 2 additional partons are included at NLO ME, and up to 4 additional partons are included in LO ME. The merging is achieved through CKKW-L merging technique, with a merging scale of 20 GeV [72, 73]. Parton shower and underlying event are provided by Sherpa. Higher number of jets events are modeled by parton shower. Cross-sections are calculated at NNLO [74]. In order to obtain enough statistics in sensitive regions, samples are generated separately for sliced kinematic phase spaces, and filtered jet flavor composition. About 1–12.5 M events are generated for each samples.

4.2.4   Diboson

ZZ and WZ (VZ) are generated with Sherpa2.2.1 [40, 75]. interfaced with NNPDfs [69]. In order to have a good modeling at large number of jets, up to 1 additional partons are included at NLO ME, and up to 3 additional partons are included at LO ME. WW is generated with Sherpa2.1.1, and up to 3 additional partons at LO. However, the contribution of WW to this analysis is negligible. The merging is achieved through CKKW-L merging technique, with a merging scale of 20 GeV [72, 73]. Parton shower and underlying event are provided by Sherpa. Higher number of jets events are modeled by parton shower. Cross-sections are calculated at NLO. About 4–7 M events are generated for diboson samples.

Chapter 5

Object definition

This analysis uses reconstructed objects such as electron, muon and jet. However, there are huge amount of background objects such as jet from the multi-jet events and pile-up events. Therefore, object definition is important to suppress background objects. In this chapter, definitions of Primary Vertex (PV), electron, muon, jet, b-jet, truth tagging, τ-jet missing transverse momentum ($E_{\mathrm{T}}^{\mathrm{miss}}$), and overlap removal are summarized in 5.1, 5.2, 5.3, 5.4, 5.5, 5.6, 5.7, 5.8, and 5.9 respectively.

5.1 Primary Vertex

Interaction vertices are reconstructed from tracks in the ID [76]. A vertex with the highest sum of track $p_{\mathrm{T}}{}^{2}$ is defined as Primary Vertex (PV). Electron, muon and jets are required to originate from the PV to reduce background objects from pile-up events. Impact parameters described below are used for the requirements.

- d_0: minimum distance between a track and PV in the x-y plane
- z_0: minimum distance between a track and PV along the z-axis

Usually $z_0\sin\theta$ is used to make efficiency less dependent on polar angle.

5.2 Electron

Electrons are reconstructed in following steps [77]. The effect of radiative

- Cluster finding: A sliding window is used to search for a seed cluster. The sliding window size is 3×5 in unit of 0.025×0.025 in $\eta \times \phi$. This corresponds to the granularity of the middle layer of the EM calorimeter. The cluster is required to have $E_{\mathrm{T}} \geq 2.5$ GeV. The efficiency of the cluster finding is 95–99% at $E_{\mathrm{T}} = 7$–15 GeV and more than 99% in $E_{\mathrm{T}} > 15$ GeV. Single particle samples are used for the efficiency studies.
- Track reconstruction: Track reconstruction is done by a pattern recognition and track fit. The standard pattern recognition uses pion hypothesis for energy loss. Seed track is required to have 3 hits in the silicon detector layers and $p_{\mathrm{T}} \geq 1$ GeV. Full track is required to have at least 7 hits in the ID. If a track fail to become full track using the pion hypothesis, then pattern recognition using electron hypothesis is performed. Then track fit is performed with pion hypothesis or electron hypothesis. If a track candidate fails to fit with pion hypothesis, then electron hypothesis is used.
- Matching: The track is extrapolated in to the middle layer of the EM calorimeter and distance between

the track and the cluster is used for the matching. The matching takes into account of the radiative energy loss (bremsstrahlung) in the ID, using the Gaussian Sum Filter algorithm [78]. A clusters without a track is considered as a photon. If more than 1 track is matched then 1 track is selected as primary track. The selection is based on the distance, p_{T} and hit in the 1st layer of silicon layer.

Electron energy is calibrated by a multivariate technique based on simulation [79]. The $Z \rightarrow ee$ data driven correction is re-derived for Run2 or extrapolated from Run1.

Electron identification is performed with a likelihood method [77]. The likelihood uses signal and background Probability Density Functions (PDF) of discriminating variables:

$$L_{S,B}(\vec{x}) = \prod_{i=1}^{n} P_{S,Bi}, (x_i), \tag{5.1}$$

where L_S and L_B are the likelihood for signal and background, P_S and P_B are the PDF, and $\vec{x}$ is the vector of discriminating variables. The variables contain information of calorimeter shower shape, TRT likelihood, track-cluster matching, track properties, and bremsstrahlung. Then a discriminant is constructed as:

$$d_L = \frac{L_S}{L_S + L_B}. \tag{5.2}$$

There are Loose, Medium, Tight working points. The signal efficiencies range from 90% to 78% at $E_{\mathrm{T}} = 25$ GeV, and increase with E_{T}. The background rates range from 0.8% to 0.3% at $E_{\mathrm{T}} = 25$ GeV, and decrease with E_{T}.

In this analysis, following requirements are used to define VHLoose electron:

- $p_{\mathrm{T}} \geq 7$ GeV
- $|\eta| < 2.47$
- $|d_0|/\sigma_{d_0} < 5$
- $|z_0\sin\theta| < 0.5$ mm
- Loose likelihood
- Track isolation

The track isolation uses sum all tracks p_{T},in a variable cone with $\Delta R = \min(0.2, 10 \text{ GeV}/E_{\mathrm{T}})$, and it is tuned to achieve 99% flat efficiency as a function of E_{T}. The track quality requirements are:

- $E_{\mathrm{T}} \geq 1$ GeV
- Number of hits requirements
- $|z_0\sin\theta| < 3$ mm

An additional requirement is used to define VHSignal electrons:

- $p_{\mathrm{T}} \geq 27$ GeV

Acceptance $\times$ efficiency of the $ZH \rightarrow eebb$ signal is about 70%, requiring exactly 2 VHLoose electrons and at least 1 VHSignal electron. The acceptance of p_{T} and η is about 80%. The efficiency of the other selection is about 90%.

5.3   Muon

Muon tracks are reconstructed separately in the ID and the MS, and then the tracks are combined [80]. The ID track reconstruction is similar to electron. The MS track reconstruction starts from finding segments in each muon chamber. MDT segments are reconstructed by a straight-line fit to the hits in each layer. RPC and TGC are used to measure the position in the η-ϕ plane. CSC segments are reconstructed by a separate search in the η-ϕ plane. The segments are loosely required to originate from the IP. Then MS tracks are reconstructed by fitting hits in the segments. The hits, segments and tracks are selected based on the fit quality. Finally, ID and MS tracks are combined in 4 types of muon listed below.

- Combined (CB) muon: CB muon is reconstructed from combined refit to the ID and MS hits. It is used as a default muon type. Most of muons are reconstructed by an outside-in pattern recognition which extrapolates MS track into ID. An inside-out approach is used if the outside-in approach failed.
- Segment-tagged (ST) muon: ST muon is an ID track with at least 1 segment in MDT or CSC. It is used for muons that cross only 1 layer of MS because of low p_{T} or low MS acceptance.
- Calorimeter-tagged (CT) muon: CT muon is an ID track with an energy deposite in the calorimeter which is compatible with minimum ionizing particle. It is used for muons in $|\eta| < 0.1$ where MS is not fully installed because of cabling and services.
- Extrapolated (ME) muon: ME muon is reconstructed only from a MS track and loosely required to originate from the IP. It is used for muons in $2.5 < |\eta| < 2.7$ where ID is not installed. The muon parameters are defined at the IP, taking account of energy loss in the calorimeter.

Overlaps among muon types are removed in priority of CB > ST > CT. The ME muon does not overlap among muon types.

Muon identification is performed to suppress background such as pion and kaon decay in flight. The background is expected to have bad fit quality and different p_{T} of the ID muon and the MS muon. The variables used for the CB muon are listed below.

- q/p significance: difference between the ratio of charge and momentum of the ID muon and the MS muon divided by uncertainty
- ρ': difference between p_{T} of the ID muon and the MS muon divided by p_{T} of the CB muon
- Normalized χ^2 of the combined fit

Number of ID hits is required to have at least 1 Pixel hit, at least 5 SCT hits, fewer than 3 holes, at least 10% of TRT hits remain in the final fit for muons in $0.1 < |\eta| < 0.9$. A hole is counted if a track passes an active sensor without hit. Then, four identification quality are defined as follows.

- Loose: Loose quality is used to maximise the efficiency. All muon types are used. The CT muon and the ME muon are used only for $|\eta| < 0.1$ region.
- Medium: Medium quality is a standard quality. The CB muon and the ME muon are used. The CB muon is required to have ≥ 3 hits in at least 2 MDT layers except $|\eta| < 0.1$ region. The CB muon in $|\eta| < 0.1$ region is required to have at least 1 MDT layer. No more than 1 MDT hole layer is allowed. ME is required to have at least 3 MDT or CSC layers. The q/p significance is required to be < 7.

- Tight: Tight quality is used to maximize the purity. The CB muon is used. At least 2 station of the MS hits are required. Normalized χ^2 of the combined fit is required to be < 8. A 2-dimensional cut on the q/p significance and ρ' as function of p_T is applied. This is to reduce background especially in $p_T < 20$ GeV where background rate is higher.
- High-p_T: High-p_T quality is used to maximise the momentum resolution in $p_T > 100$ GeV. At least 3 station of the MS hits are required. This requirement reduces 20% of efficiency and improves p_T resolution by 30% at $p_T > 1.5$ TeV. Regions where MS is not well aligned are vetoed.

The efficiencies of Loose, Medium, Tight, and High-p_T are about 97%, 95%, 90%, 80%. Background rates are less than 1% without isolation requirement, and the isolation reduces the background rates significantly. The rates are derived from simulation however it is also valid in data. $K_S^0 \rightarrow \pi^+\pi^-$ data was collected with calorimeter-based triggers and good agreement in data/simulation was observed.

In this analysis, muons passed following requirements are defined as VHLoose muons:

- $p_T \geq 7$ GeV
- $|\eta| < 2.7$
- $|d_0|/\sigma_{d_0} < 3$
- $|z_0 \sin\theta| < 0.5$ mm
- Loose quality
- Track isolation

Loose quality is used in 2-lepton channel to maximise the efficiency. since fake rate is negligible after requiring 2 muons and Z mass. The track isolation uses sum of all track p_T, in a variable cone with $\Delta R = \min(0.3, 10$ GeV$/p_T)$, and it is tuned to achieve 99% flat efficiency as function of p_T. The track is required to be $p_T > 1$ GeV. Additional requirements are used to define VHSignal muons in this analysis:

- $p_T \geq 27$ GeV
- $|\eta| < 2.5$

Acceptance $\times$ efficiency of the $ZH \rightarrow \mu\mu bb$ signal is about 70%, requiring exactly 2 VHLoose muons and at least 1 VHSignal muon. The acceptance of p_T and η is about 80%. The efficiency of the other selection is about 90%.

5.4 Jet

Jets are reconstructed at the electromagnetic energy scale (EM-scale) with the AntiKt algorithm with radius parameter $R = 0.4$ (AntiKt4) [81]. The EM-scale corresponds to the energy deposit of electromagnetically interacting particles. The AntiKt algorithm uses a collection of topological clusters (topo-clusters). Topo-clusters are reconstructed from neighboring calorimeter cells with significant energy above noise level (typically 4 standard deviations). The noise threshold is estimated from simulated of pile-up noise and measured calorimeter electronic noise. Topo-clusters are now not allowed to seed from the presampler layers to reduce jet from pile-up events. Jets are required to have $p_T > 7$ GeV at the reconstruction.

Jet cleaning is performed following a criteria [82]. Events with bad jets are removed. The efficiency is 99.5-99.9% for $p_T = 20$–100 GeV. Main sources of backgrounds are listed below.

- Beam Induced Background (BIB): BIB are caused by proton losses before IP. Muons from the secondary

cascade can reach ATLAS.

- Cosmic-ray showers: Cosmic-ray showers are produced in the atmosphere. Muons can reach ATLAS in the 100 m underground.
- Calorimeter noise: Noisy cells are masked before jet and missing transverse momentum reconstruction. Some of them are always masked and others are masked in event by event. Events with large amount of noise are removed. Most of them are removed at the data quality check however small amount of events needs to be removed in the analysis.

Jet Vertex Tagger (JVT) requirement is also used to suppress jets from pile-up events [83]. JVT is a two dimensional likelihood discriminant based on tracks and vetex information. It uses 2 variables called corrJVF and R_{p_T}. corrJVF is similar to Jet Vertex Fraction JVF that was used in Run1:

$$\mathrm{JVF} = \frac{\sum_m p_\mathrm{T}^{track(m)}(PV_0)}{\sum_n \sum_l p_\mathrm{T}^{track(l)}(PV_n)}, \tag{5.3}$$

where $\sum_m p_\mathrm{T}^{track(m)}(PV_0)$ is scalar sum of tracks p_T associated to the jet from hard-scatter vertex (PV_0), $\sum_n \sum_l p_\mathrm{T}^{track(l)}(PV_n)$ is scalar sum of tracks p_T from all vertices. The ratio is the scalar sum of tracks p_T fraction of the jet. However, the efficiency was found to decrease with number of PV. Therefore, corrJVT is used in Run2:

$$\mathrm{corrJVF} = \frac{\sum_m p_\mathrm{T}^{track(m)}(PV_0)}{\sum_m p_\mathrm{T}^{track(m)}(PV_0) + \frac{p_\mathrm{T}^{PU}}{kn_{track}^{PU}}}, \tag{5.4}$$

where $\sum_m p_\mathrm{T}^{track(m)}(PV_0)$ is scalar sum of tracks p_T associated to the jet from hard-scatter vertex (PV_0), p_T^{PU} is scalar sum of tracks p_T from any of pileup vertex, n_{track}^{PU} is number of pileup tracks. k is 0.01 from slope of p_T^{PU} with n_{track}^{PU}, corrJVF is similar to JVF but the number of PV dependence is corrected.

$$R_{p_\mathrm{T}} = \frac{\sum_k p_\mathrm{T}^{track(k)}(PV_0)}{p_\mathrm{T}^{jet}}, \tag{5.5}$$

where p_T^{jet} is fully calibrated jet p_T. These variables achieves flat efficiency as a function of number of PV, and JVT achieves about 90% efficiency with pile-up fake rate of about 1%.

In this analysis, jets are required to pass following requirements.

- $p_\mathrm{T} > 20$ GeV in $|\eta| < 2.5$ (central region)
- $p_\mathrm{T} > 30$ GeV in $|\eta| \geq 2.5$ (forward region)
- JVT requirement for $p_\mathrm{T} < 60$ GeV in $|\eta| < 2.4$

Truth jet is also reconstructed in simulation for jet calibration studies. The default truth jet uses stable final state particles, except for muons and neutrinos. Truth jet that includes muons and neutrinos is called TruthWZ jet. TruthWZ jet is used for dedicated *b*-jet energy correction in this analysis. Details are in Section 7.

5.5   *b*-jet identification

Identification of jet with *b*-hadron (*b*-jet) is performed with a multivariate discriminant (MV2c10) [31]. The MV2c10 combines three basic algorithms listed below. Lifetime of *b*-hadrons is long about $\sim$1.5 ps, $c\tau \sim 450~\mu$m. Therefore, a displaced vertex and larger impact parameter tracks can be used to select *b*-jets. Tracks used are

associated to jets using ΔR between track and jet. The ΔR become narrow for high p_T jets. For example, ΔR = 0.45 for p_T = 20 GeV and ΔR = 0.26 for p_T = 150 GeV. Further track selection is written in [32].

- Impact parameter based algorithm (IP2D, IP3D): IP2D and IP3D are log likelihood ratio discriminants, $\sum_{i=1}^{N} log(p_b/p_u)$. N is number of tracks in a jet. p_b and p_u are PDF value for b-jet and light-jet derived from simulation. IP2D uses d_0/σ_{d_0} and IP3D uses both d_0/σ_{d_0} and $z_0 sin\theta/\sigma_{z_0 sin\theta}$.
- Secondary vertex finding algorithm (SV): SV explicitly reconstruct an secondary vertex. All track pairs in a jet are used for a two track vertex test. If a two track vertex is likely from b-hadron then the new vertex is fitted with all tracks from the vertex. The SV variables such as mass, ΔR, number of tracks associated to the SV are used for MV2c10.
- Decay chain multi-vertex algorithm (JetFitter): JetFitter tries to reconstruct full b- and c- hadron decay chain. A Kalman filter is used. The JetFitter variables such as mass, ΔR, number of tracks used in JetFitter are used for MV2c10.

At 70% b-jet tagging efficiency, c-jet and light-jet misidentification rates are 0.3% and 8.2% based on $t\bar{t}$ simulation. b-tagging efficiency was measured using similar ways as Run1 [84]. In this analysis, jets are required to pass following requirements.

- $p_T > 20$ GeV in $|\eta| < 2.5$ (central region)
- pass an average 70% efficiency cut on MV2c10

5.6   Truth tagging

Simulated jets are labeled as follows, using truth hadrons with $p_T > 5$ GeV in ΔR(jet, hadron) < 0.3. If a b-hadron is found in a jet, then the jet is labeled as b. If no b-hadron is found and c-hadron is found in a jet, then the jet is labeled as c. Else, then the jet is labeled as l. The label is used to categorize $V+$ jets events. $V + bb, V + bc, V + bl, V + cc$ are categorized as $V+$ heavy flavor (HF). The rest is categorized as $V + cl, V + ll$.

For processes with large cross-sections and small acceptances, it is difficult to produce many simulated events to get the same number of events as data after selection. Therefore, a parameterized tagging is applied for $V + cc$, $V + cl$, $V + ll$ and WW. In this case, the b-tagging cut is not applied but the events are weighted according to the expected probability. The probability is parameterized as function of jet p_T and η based on tt simulation studies. These backgrounds are small about 1% level of total background in this analysis.

5.7 τ-jet

τ leptons decaying hadronically are reconstructed as jets [85]. τ leptons decay hadronically ($\tau_{had} \rightarrow$ hadrons ν_τ) or leptonically ($\tau_{lep} \rightarrow l\nu_\tau$). The hadronic decay branching ratio is about 65% and the leptonic is about 35%. 72% of the hadronic decay have 1 charged pion track. 22% have 3 charged pions tracks. 68% have at least 1 neutral pion. The pions are visible part of τ decay ($\tau_{had-vis}$). A multivariate discriminant is used to separate $\tau_{had-vis}$ from jets. The discriminant is based on shower shape, number of tracks and displaced vertex information. Electrons are also suppressed by an electron likelihood requirement with 95% τ efficiency. τ-jet reconstruction, energy calibration and identification are updated for 2016 data.

The performance were measured using 2015 data, using $Z \rightarrow \tau\tau$ tag-and-probe, with one (tag) decaying to

muon and neutrino (τ_μ), and the other (probe) decaying to τ_{had}. tt tag-and-probe was used for high p_{T}. The efficiency correction factors for simulation were derived, with a relative precision of 5% for 1 track and 6% for 3 tracks. The energy calibration is derived from the mass distribution of muon and $\tau_{\mathrm{had-vis}}$, with a relative precision of 2% for 1 track and 3% for 3 tracks. The electron rejection was measured using $Z \to ee$ tag-and-probe, with a relative precision of 3–14% depending on η. In this analysis, τ-jets are required to pass following requirements.

- $p_{\mathrm{T}} > 20$ GeV
- $|\eta| < 2.5$
- outside of the barrel endcap transition region of the calorimeter, $1.37 < |\eta| < 1.52$
- have 1 or 3 tracks in $\Delta R < 0.2$ of the jet
- pass an p_{T} independent 55% (40%) efficiency cut on the multivariate discriminant for 1 (3) tracks

5.8   Missing transverse momentum

Neutrinos can be reconstructed as a missing transverse momentum ($E_{\mathrm{T}}^{\mathrm{miss}}$) [86]. The $E_{\mathrm{T}}^{\mathrm{miss}}$ is defined as transverse momenta of negative vector sum of electrons, muons, jets (hard term) and track-based soft term (soft term). All of them are required to be from the PV and the jets and soft term are corrected to mitigate the effect of pile-up. In this analysis, $ZH \to \ell\ell bb$ signal does not have high $E_{\mathrm{T}}^{\mathrm{miss}}$. Therefore, $E_{\mathrm{T}}^{\mathrm{miss}}$ can be used to reduce tt background. The event selection is summarized in Chapter 6.

5.9   Overlap removal

Some objects can be counted as different objects even after the object definition. Therefore, an overlap removal procedure is applied in following order.

- if $\Delta R(\tau\text{-jets, electrons or muons}) < 0.2$, then τ-jets are removed
- if a muon and an electron share the ID track, then the electron is removed
- if $\Delta R(\text{jets, electrons}) < 0.2$, then jets are removed
- if $\Delta R(\text{jets, electrons}) < \min(0.4, 0.04 + 10/p_{\mathrm{T}}^{\mathrm{electron}})$, then electrons are removed
- if $\Delta R(\text{jets, muons}) < 0.2$, then jets are removed
- if $\Delta R(\text{jets, muons}) < \min(0.4, 0.04 + 10/p_{\mathrm{T}}^{\mathrm{muon}})$, then muons are removed
- if $\Delta R(\text{jets, } \tau\text{-jets}) < 0.2$, then jets are removed

At first, jets around selected leptons within $\Delta R = 0.2$ are removed. Then, $p_{\mathrm{T}} = 10$ GeV level leptons around jets within $\Delta R = 0.4$ level are removed, since the leptons are likely to be from survived jets. Such leptons are removed from lepton multiplicity counting, but used in the b-jet energy correction in Chapter 7.

Chapter 6

Event selection and categorization

In order to search for the $ZH \to \ell\ell bb$ signal, this analysis selects events with 2 leptons and 2 b-jets. Main backgrounds are $Z + bb$, $t\bar{t}$, diboson, and single top events. The background cross-sections are much larger than the signal as shown in Figure 2.1. Therefore, event selection and categorization are important to enhance the sensitivity. This thesis presents a multivariate analysis and a cut-based analysis. The multivariate analysis can improve the sensitivity, by separating the signal and background efficiently, using several kinematic variables at the same time, instead of applying simple cuts on each variable. Therefore, a loose event selection is applied for the multivariate analysis. The cut-based analysis is also important as a cross check of the multivariate analysis. In this chapter, event selection and categorization for the multivariate analysis is summarized in Section 6.1, for the cut-based analysis is summarized in Section 6.2.

Lepton triggers used in this analysis are summarized in Table 6.1. Single lepton triggers were used since acceptance gain by di-lepton triggers was found to be 1% level. Low p_T isolated triggers and high p_T non-isolated triggers are used to maximize the acceptance. Higher threshold and tighter requirement triggers are used from 2016, due to the limited band width and the increasing luminosity. However, the acceptance loss for the signal is less than 1% and the sensitivity loss is negligible, since high p_T^V region is sensitive in this analysis. Trigger efficiency of simulated signal events, with regard to the offline selection is about 95% for the electron channel and 87% for the muon channel, in ≥ 2 jet, inclusive p_T^V region. The lower efficiency in the muon channel is mainly from the geometrical coverage in the barrel region.

6.1 Multivariate analysis

Event selection for the multivariate analysis is summarized in Table 6.2. The multivariate analysis uses a looser event selection compared to the cut-based analysis as mentioned earlier. At first, events are required to pass the single lepton triggers. Exactly 2 loose electrons or 2 loose muons are required. At least one of the 2 leptons is required to have medium quality and $p_\mathrm{T} > 27$ GeV. Invariant mass of the 2 leptons $m_{\ell\ell}$ is required to be around the Z mass, 81–101 GeV. Thus, $t\bar{t}$ and multi-jet are reduced and the Z boson processes are selected. Multi-jet was found to be negligible as shown in Appendix A. The Z boson p_T (p_T^V) is required to be $p_\mathrm{T}^V \geq 75$ GeV, since sensitivity in $p_\mathrm{T}^V < 75$ GeV is small. At least 2 jets and exactly 2 b-jets are required. Leading b-jet p_T is required to be greater than 45 GeV, since there is no signal with leading b-jet with $p_\mathrm{T} < 45$ GeV.

Event categorization for the multivariate analysis is also summarized in Table 6.2. The p_T^V is separated into 2 regions of 75–150 GeV and 150– GeV. Separating regions with enough statistics is basically beneficial, since number of signal and background events are different among regions. The 150 GeV is from the $E_\mathrm{T}^\mathrm{miss}$ trigger

Period	Electron	Muon
2015	`HLT_e24_lhmedium_L1EM20VH`	`HLT_mu20_iloose_L1MU15`
	OR `HLT_e60_lhmedium`	OR `HLT_mu40`
2016	`HLT_e26_lhtight_nod0_ivarloose`	`HLT_mu24_iloose`
	OR `HLT_e60_lhmedium_nod0`	OR `HLT_mu40`
	OR `HLT_e60_medium`	
	OR `HLT_e140_lhloose_nod0`	
	`HLT_e26_lhtight_nod0_ivarloose`	`HLT_mu24_ivarmedium`
	OR `HLT_e60_lhmedium_nod0`	OR `HLT_mu50`
	OR `HLT_e60_medium`	
	OR `HLT_e140_lhloose_nod0`	
	`HLT_e26_lhtight_nod0_ivarloose`	`HLT_mu26_ivarmedium`
	OR `HLT_e60_lhmedium_nod0`	OR `HLT_mu50`
	OR `HLT_e60_medium`	
	OR `HLT_e140_lhloose_nod0`	

Table 6.1   Lepton triggers used in this analysis. HLT means the High Level Trigger. e24 means $E_T >$ 24 GeV. mu24 means $p_T >$ 24 GeV. lhmedium means medium likelihood requirement. nod0 means no d0 variables is used in the likelihood. iloose means $p_T\text{cone}20/p_T < 0.12$. $p_T\text{cone}20$ is the p_T sum of other ID tracks in cone ΔR=0.2. imedium means $p_T\text{cone}30/p_T < 0.06$. $p_T\text{cone}30$ is the p_T sum of other ID tracks in cone ΔR=0.3. ivarloose means $p_T\text{varcone}30/p_T(\text{muon}) < 0.16$. $p_T\text{varcone}30$ is the p_T sum of other ID tracks in variable cone at maximum ΔR=0.3. ivarmedium means $p_T\text{varcone}30/p_T(\text{muon}) < 0.07$.
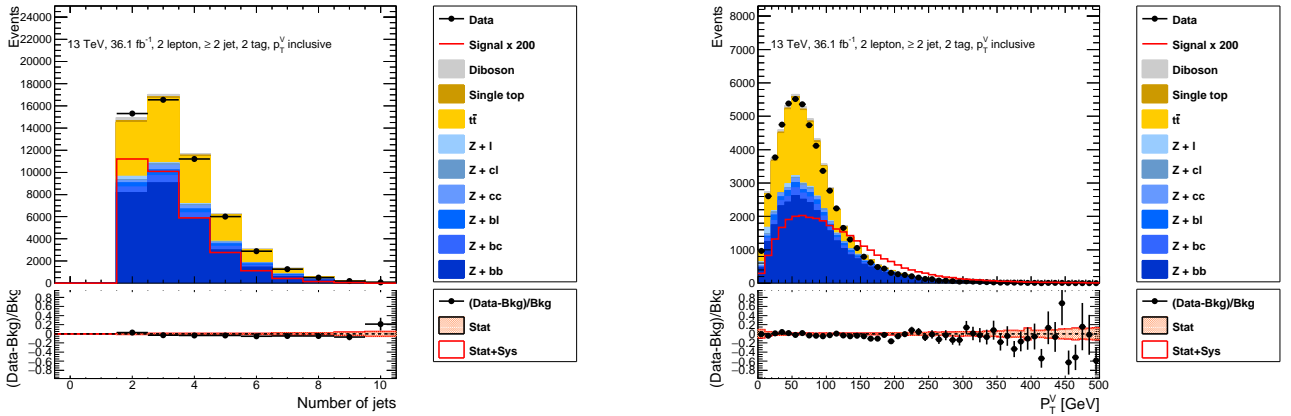

Figure 6.1   Number of jets (left) and p_T^V (right) distributions. Z+HF is scaled by 1.25 since nominal prediction was found to be lower than data as shown in Chapter 11. Signal is scaled by 200.

threshold that is used in 0-lepton and 1-lepton channel. Number of jets is separated into 2 regions, 2 jet and ≥ 3 jet. Figure 6.1 shows the number of jets and p_T^V distributions. The Signal to Background ratio (S/B) is the best in 2 jet $p_T^V =$ 150– GeV, as shown in Figure 6.1. Furthermore, flavor and charge of the 2 leptons are also used to define regions. For Signal Region (SR), the 2 leptons are required to have the same flavor, ee or $\mu\mu$. Muons are required to have opposite charge while electrons are not. This is because electron charge mis-identification rate is higher than muons, as shown in Appendix A. For top Control Region (CR), 2 leptons are required to have different flavor, $e\mu$, and opposite charge.

	Multivariate analysis	Cut-based analysis
Trigger	Single lepton	Single lepton
Leptons	2 VHLoose,	2 VHLoose
	≥ 1 VHSignal	≥ 1 VHSignal
$E_{\mathrm{T}}^{\mathrm{miss}}$		$E_{\mathrm{T}}^{\mathrm{miss}}/\sqrt{S_{\mathrm{T}}} < 3.5$
$m_{\ell\ell}$	81–101 GeV	81–101 GeV
Jets	2 jets	2 jets
	≥ 3 jets	≥ 3 jets
Jet p_{T}	> 20 GeV	> 20 GeV
b-jets	Exactly 2 b-jets	Exactly 2 b-jets
Leading b-jet p_{T}	> 45 GeV	> 45 GeV
$p_{\mathrm{T}}^{V}, \Delta R(b,b)$	75–150 GeV	75–150 GeV, < 3.0
	150– GeV	150–200 GeV, < 1.8
		200– GeV, < 1.2
SR	ee	ee
	$\mu\mu$, opposite charge	$\mu\mu$, opposite charge
CR	$e\mu$, opposite charge	$e\mu$, opposite charge

Table 6.2   Event selection for the multivariate (left) analysis and the cut-based analysis (right). S_{T} is scalar sum of all leptons and jets p_{T}. The $E_{\mathrm{T}}^{\mathrm{miss}}$ cut is only applied for the SR in the cut-based analysis, since the statistics of data was limited in the top CR.

6.2   Cut-based analysis

Event selection for the cut-based analysis is also summarized in Table 6.2. The cut-based analysis applies additional cuts to enhance the sensitivity. Figure 6.2 shows the variables to consider additional cuts for the cut-based analysis. The p_{T} and $m_{\ell\ell}$ cuts are already optimized in the multivariate analysis. Therefore, only $E_{\mathrm{T}}^{\mathrm{miss}}$ significance cut, $E_{\mathrm{T}}^{\mathrm{miss}}/\sqrt{S_{\mathrm{T}}} < 3.5$, where S_{T} is scalar sum of all leptons and jets p_{T}, is applied as an additional cut, before splitting p_{T}^{V} regions. This reduces the $t\bar{t}$ background. The $E_{\mathrm{T}}^{\mathrm{miss}}$ cut is only applied for the SR in the cut-based analysis, since the statistics of data was limited in the top CR.

Event categorization for the cut-based analysis is also summarized in Table 6.2. For the SR, p_{T}^{V} is split into 75–150 GeV, 150–200 GeV and 200– GeV. The S/B is the best in 2 jet $p_{\mathrm{T}}^{V} = 200$– GeV region, as shown in Figure 6.1. For the top CR, p_{T}^{V} is split into 75–150 GeV and 150– GeV, since the statistics of data was limited in the top CR, especially in the 2 jet high p_{T}^{V} region. Figure 6.3 shows $\Delta R(b,b)$ distributions in each p_{T}^{V} categories in the cut-based analysis. In order to reduce Z+jets background, $\Delta R(b,b)$ cuts are applied as follows:

- $\Delta R(b,b) < 3.0$ in $p_{\mathrm{T}}^{V} = 75$–150 GeV region,
- $\Delta R(b,b) < 1.8$ in $p_{\mathrm{T}}^{V} = 150$–200 GeV region,
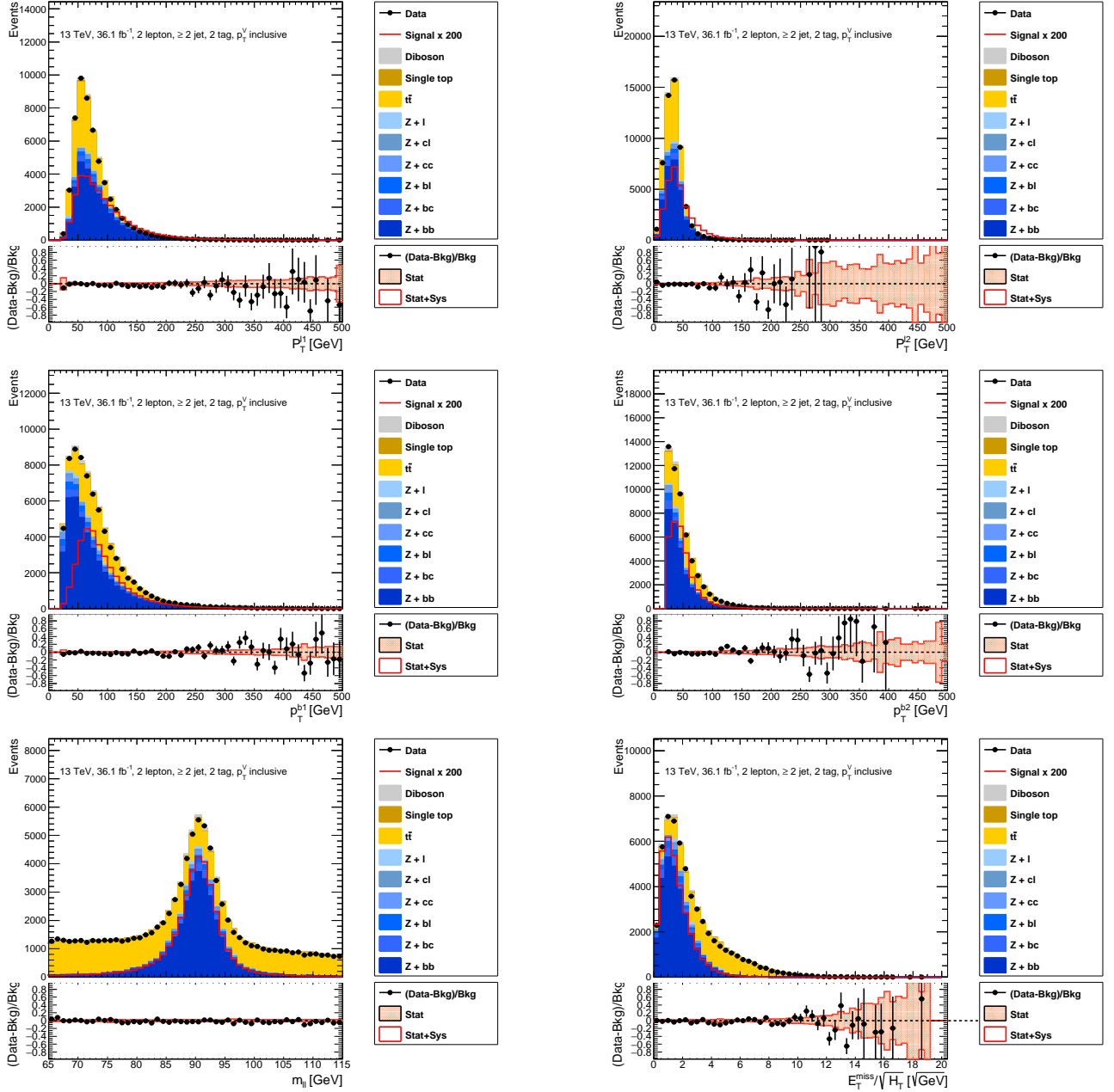- $\Delta R(b,b) < 1.2$ in $p_{\mathrm{T}}^{V} = 200$– GeV region.

Figure 6.2   Variables to consider additional cuts for the cut-based analysis. p_T of leading lepton (top left), p_T of sub-leading lepton (top right), p_T of leading b-jet (middle left), p_T of sub-leading b-jet (middle right), $m_{\ell\ell}$ (bottom left), $E_T^{miss}/\sqrt{S_T}$ (bottom right). p_T of sub-leading b-jet and $m_{\ell\ell}$ (bottom left) are so called N-1 plots, removing cut on each variable. Z+HF is scaled by 1.25 since nominal prediction was found to be lower than data as shown in Chapter 11. Signal is scaled by 200.
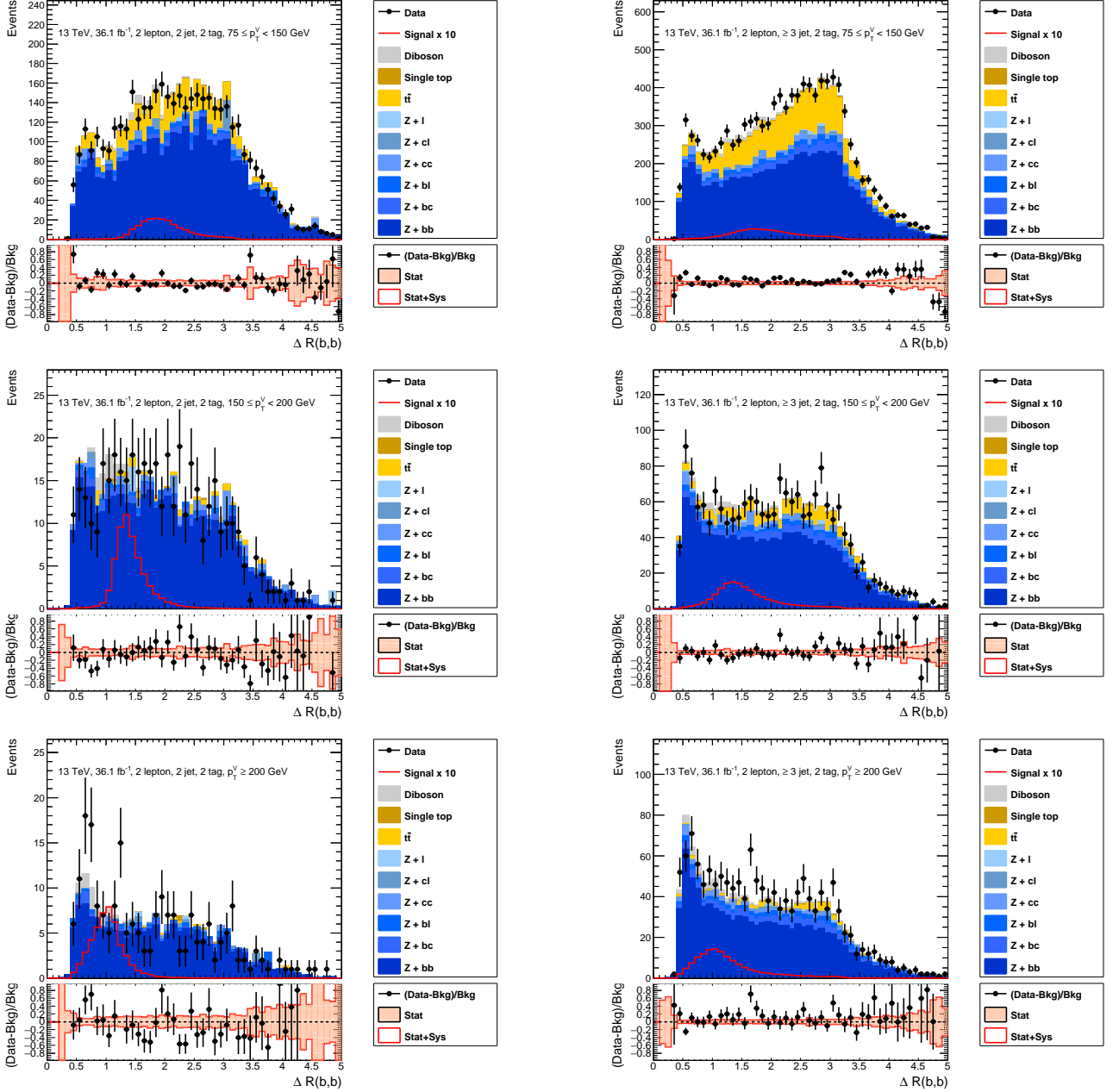
Figure 6.3 $\Delta R(b, b)$ distributions in each p_T^V categories in the cut-based analysis. 2 jet (left) and ≥ 3 jet (right). $p_T^V = 75$–150 GeV (top), $p_T^V = 150$–200 GeV (middle), $p_T^V = 200$– GeV (bottom). Z+HF and $t\bar{t}$ are scaled by the same factors in Section 11.1. Signal is scaled by 10.

Chapter 7

b-jet energy correction

The $H \rightarrow bb$ signal can be observed as a bump in the m_{bb} distribution. However, the default jet calibration is not optimized for b-jet, and it degrades the m_{bb} resolution significantly. Therefore, additional b-jet energy correction is studied to improve the Higgs mass resolution. In this chapter, the default jet calibration is reviewed in Section 7.1, muon-in-jet correction is presented in Section 7.2, p_{T} dependent correction is summarized in Section 7.3, kinematic fit correction is discussed in Section 7.4, performance of b-jet energy correction is shown in Section 7.5.

7.1 Global Sequential Calibration

The default jet calibration is called Global Sequential Calibration (GSC) [81]. It uses 5 jet properties to improve jet energy resolution. Jet p_{T} corrections as functions of properties are applied sequentially for the AntiKt4 EM+JES jets. The variables are listed below.

- fraction of jet energy measured in the 1st layer of the Tile calorimeter (f_{Tile0})
- fraction of jet energy measured in the 3rd layer of the LAr calorimeter (f_{LAr3})
- number of associated tracks with $p_{\mathrm{T}} > 1$ GeV (n_{trk})
- average p_{T}-weighted transverse distance in the transverse plane between the jet axis and all associated tracks with $p_{\mathrm{T}} > 1$ GeV (W_{trk})
- the number of muon track segments associated with the jet (n_{segments})

Differences between data and simulation are also corrected, using p_{T} balance of Z+jet and γ+jet events. However, GSC is not optimized for b-jet and it results in low p_{T} responce, since b-jet has unique features such as semileptonic decay and out-of-cone effect. Therefore, additional b-jet energy correction is studied in following sections.

7.2 muon-in-jet correction

b-jet with semileptonic decay muon results in lower energy responce, since the muon carries energy outside of the calorimeter. The lower responce can be corrected by adding the muon 4-vector back to the jet, after subtracting minimum ionizing particle energy loss in the calorimeter. This correction is called muon-in-jet correction (Muon). About 10% of b-jets have muons from the semileptonic decay. Muons for the muon-in-jet correction is selected with following requirements:
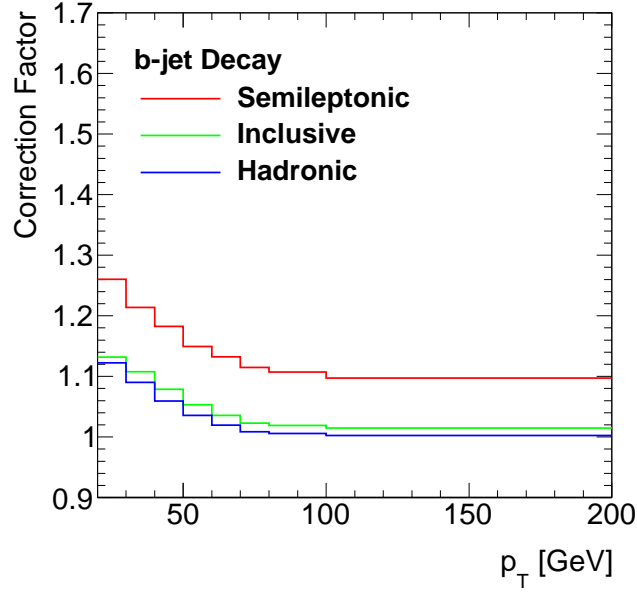
- $\Delta R(\mathrm{jet}, \mathrm{muon}) < 0.4$

Figure 7.1   *b*-jet p_T dependent correction factors. Inclusive (green), semileptonic (red) and hadronic (blue) *b*-jet decay.

- $p_T > 5$ GeV
- $|\eta| < 2.7$
- Medium quality cuts

If more than one muon are found, the closest to the jet axis is selected. These requirements are optimized to suppress fake muon rate less than 1% level and maximize the efficiency up to 95% level. The muon quality cuts are summarized in Section 5.3. The loose quality includes calorimeter based muons around $\eta = 0$ to cover the muon spectrometer holes. However, higher fake rate was found around the $\eta = 0$. Therefore, the medium quality is required for the muon-in-jet.

7.3 p_T dependent correction

b-jet p_T responce after the muon-in-jet correction is still low about 13–1% at $p_T = 20$-100 GeV, because of semileptonic decay neutrino and out-of-cone effect. The out-of-cone effect is expected in low p_T *b*-jet, since the mass of *b* quark is higher than light quarks, as shown in Table 2.1. Therefore, a p_T dependent correction (PtReco) was derived using the TruthWZ jet in signal samples. Figure 7.1 shows the p_T dependent correction factors, for inclusive, semileptonic and hadronic *b*-jet decay separately. The inclusive correction factors were used in Run1. The correction factors are separated for semileptonic and hadronic in Run2. Larger correction factors about 26–10% is applied for semileptonic to take account of the semileptonic decay neutrino. The semileptonic decay is tagged by muon or electron in jet. The electron in jet is selected with following requirements.

- $\Delta R(j, e) < 0.4$
- $p_T > 5$ GeV
- $|\eta| < 2.47$
- Quality cuts

7.4   Kinematic Fit

Jet energy resolution is typically 10% level, and electron energy and muon momentum resolution are typically 1% level. Therefore, it is possible to improve b-jet energy correction by constraining the $\ell\ell bb$ system to be balanced in the transverse plane. This correction is called Kinematic Fit (KF). It was developed in Run1 [87] and upgraded in Run2. There are 4 (5) fit parameters for 2 (3) jet event:

- p_{T} of 2 b-jets
- p_{T} of 2 leptons
- (p_{T} of additional jet)

There are 3 constraints in the KF:

- p_{T} : Gaussian with a width of resolution for 2 leptons and 3rd jet, Transfer Functions (TF) for 2 b-jets
- p_{X}^{ZH} and p_{Y}^{ZH} : Gaussian with a width of 9 GeV
- $m_{\ell\ell}$: Breit-Wigner (BW) distribution of Z

A negative log likelihood is minimized to get the fit value:

$$-2\ln L = -\sum_{b-\mathrm{jets}} 2\ln L_{p_{\mathrm{T}}^{\mathrm{Fit}}} + \sum_{\mathrm{leptons,\ jets}} \frac{(p_{\mathrm{T}}^{\mathrm{Nominal}} - p_{\mathrm{T}}^{\mathrm{Fit}})^2}{\sigma_{p_{\mathrm{T}}}^2} + \frac{(p_{\mathrm{X}}^{ZH})^2}{\sigma_{p_{\mathrm{X}}^{ZH}}^2} + \frac{(p_{\mathrm{Y}}^{ZH})^2}{\sigma_{p_{\mathrm{Y}}^{ZH}}^2} + 2\ln\left((m_{\ell\ell}^2 - m_Z^2)^2 + m_Z^2\Gamma_Z^2\right) \quad (7.1)$$

The 1st term is the b-jet TF. The TF are b-jet p_{T} responce probability functions as shown in Figure 7.2. b-jet with muons shows lower response because of semileptonic decay neutrino. The TF are separated for b-jet with and without muons in Run2, to take account of the lower response. The 2nd term is the p_{T} constrained by the Gaussian with a width of resolution. $p_{\mathrm{T}}^{\mathrm{Nominal}}$ is measured p_{T}. Additional jet is also included for 3 jet events. The 3rd and 4th terms are the balance constraints in the transverse plane. The Gaussian with a width of 9 GeV is used to get the best m_{bb} resolution of the signal as shown in Figure 7.3. The $\ell\ell bbj$ system is constrained to be balanced in the transverse plane for 3 jet events. The 5th term is the Z mass constraint. m_Z is the Z mass of about 91 GeV. Γ_Z is the Z width of about 2.5 GeV.

7.5   Performance

Figure 7.4–7.5 are m_{bb} distributions of $qq \to ZH$, $gg \to ZH$, comparing various b-jet energy correction. Bukin function is used to fit the distributions [88]. The muon-in-jet correction improves m_{bb} resolution of signal by 13%. The p_{T} dependent correction improves m_{bb} resolution of signal by 18%. The KF improves m_{bb} resolution of $qq \to ZH$ by 40% (30%) for 2 jet (3 jet) in the most sensitive $p_{\mathrm{T}}^V > 150$ GeV region. However, the KF did not improve m_{bb} resolution in ≥ 4 jet events, since the system balance is more smeared by additional jets. Therefore, the p_{T} dependent correction is used for ≥ 4 jet events.

Figure 7.6, 7.7 and 7.8 are the m_{bb} distribution in 2 jet, 3 jet and ≥ 4 jet events. Appendix B shows the KF variables. Good agreement between data and simulation was found in the m_{bb} sideband and the KF variables. Backgrounds are not enhanced at the mass of 125 GeV, since none of b-jet energy correction uses the Higgs mass constraint. Table 7.1 shows sensitivity in each region comparing various b-jet energy correction. The sensitivity is calculated from the binned log likelihood ratio, defined as square root of sum of $2((s+b)\ln(1+s/b)-s)$ in each bin. The sensitivity gain by the KF is about 10% in the most sensitive 2 tag 2 jet $p_{\mathrm{T}}^V = 150-$ GeV.
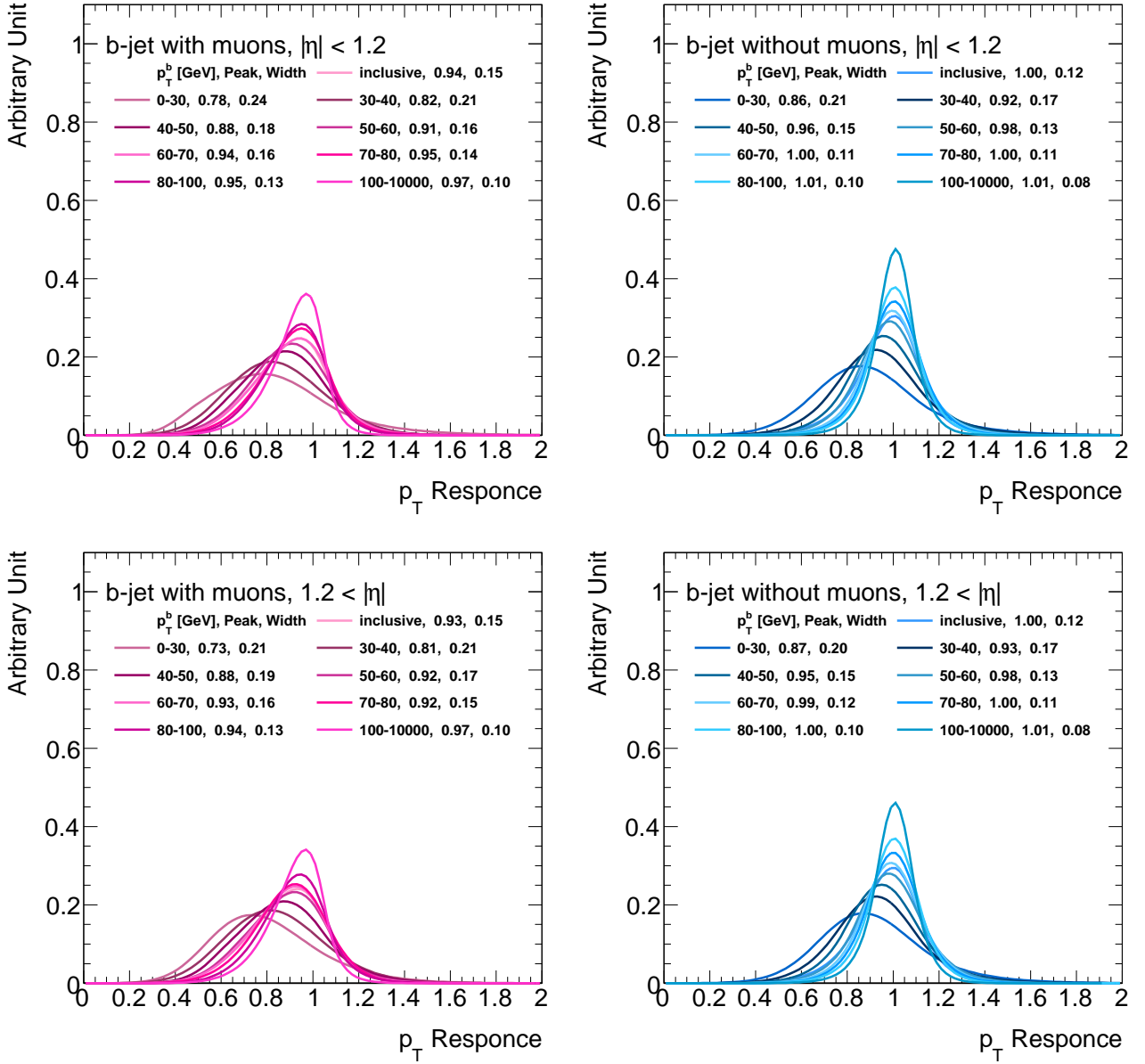
Figure 7.2 Transfer Functions. *b*-jet with muons (left), *b*-jet without muons (right), $\eta = 0$–1.2 (top), $\eta >$ 1.2 (bottom).
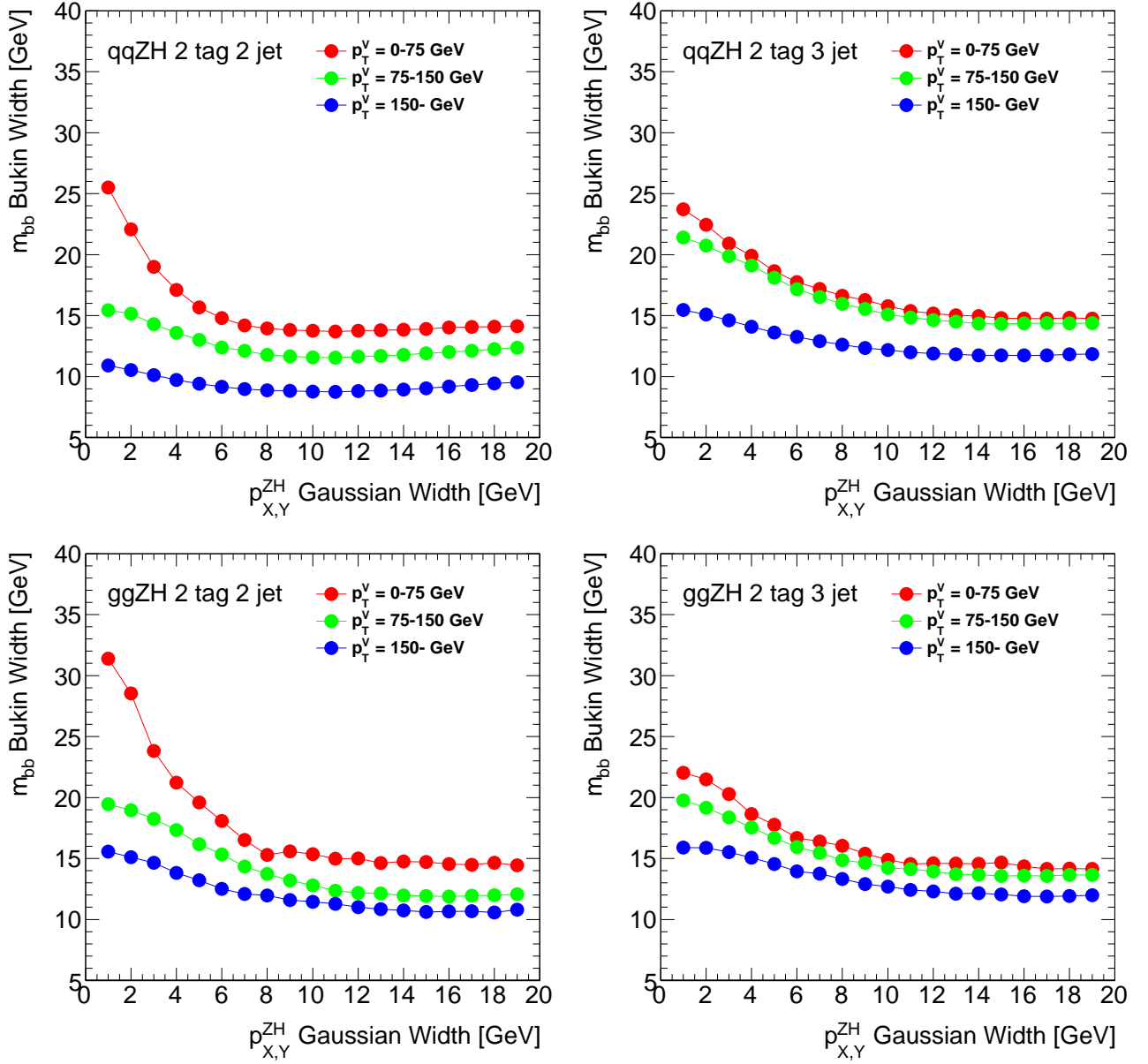
Figure 7.3 m_{bb} width of signal as a function of p_X^{ZH} and p_Y^{ZH} balance constraint. 2 jet (left), 3 jet (right), $qq \to ZH$ (top), $gg \to ZH$ (bottom).
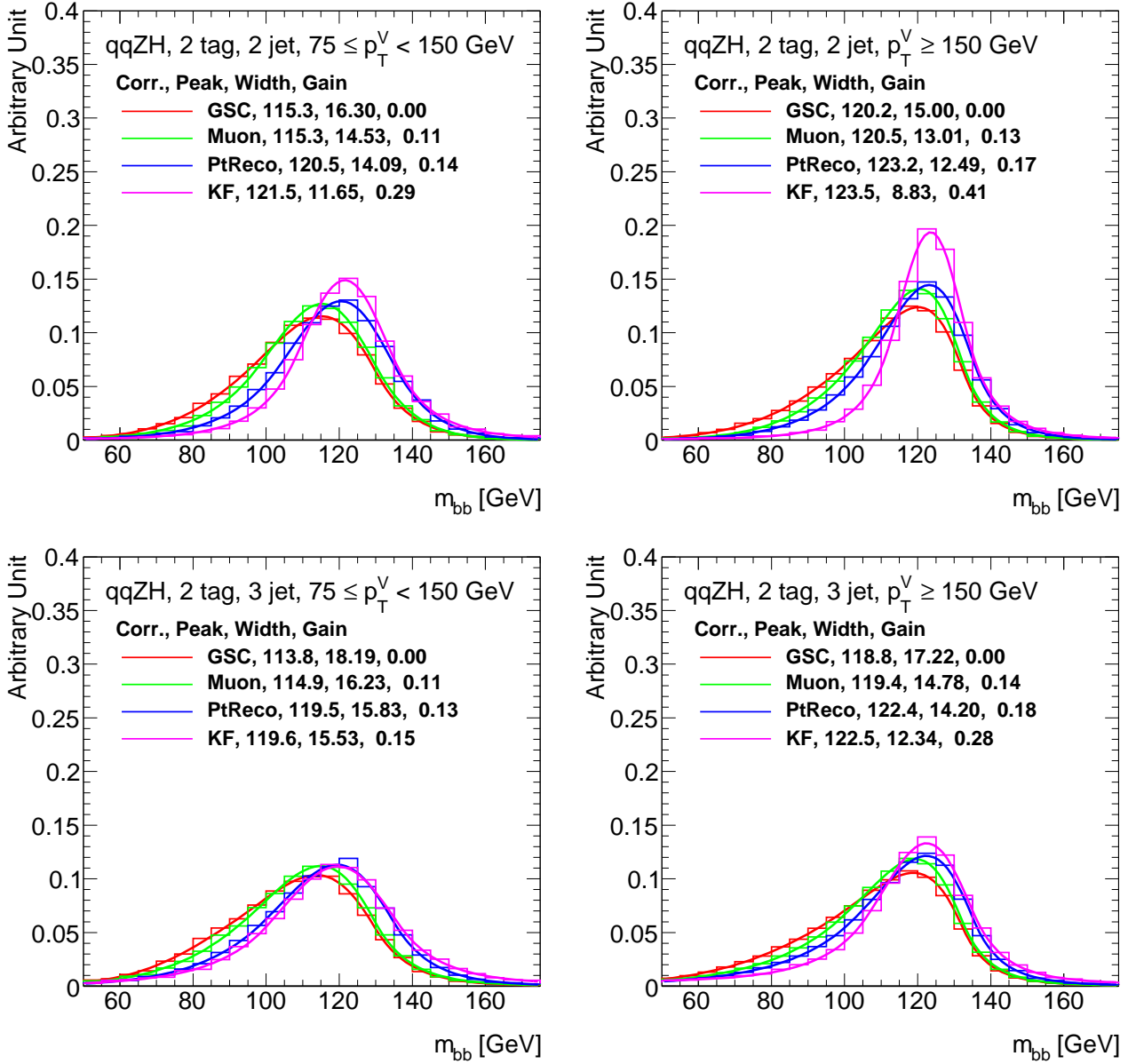
Figure 7.4 m_{bb} of $qq \to ZH$ comparing *b*-jet energy correction. 2 jet (left) 3 jet (right), $p_T^V = 75$–150 GeV (top), $p_T^V = 150$– GeV (bottom).
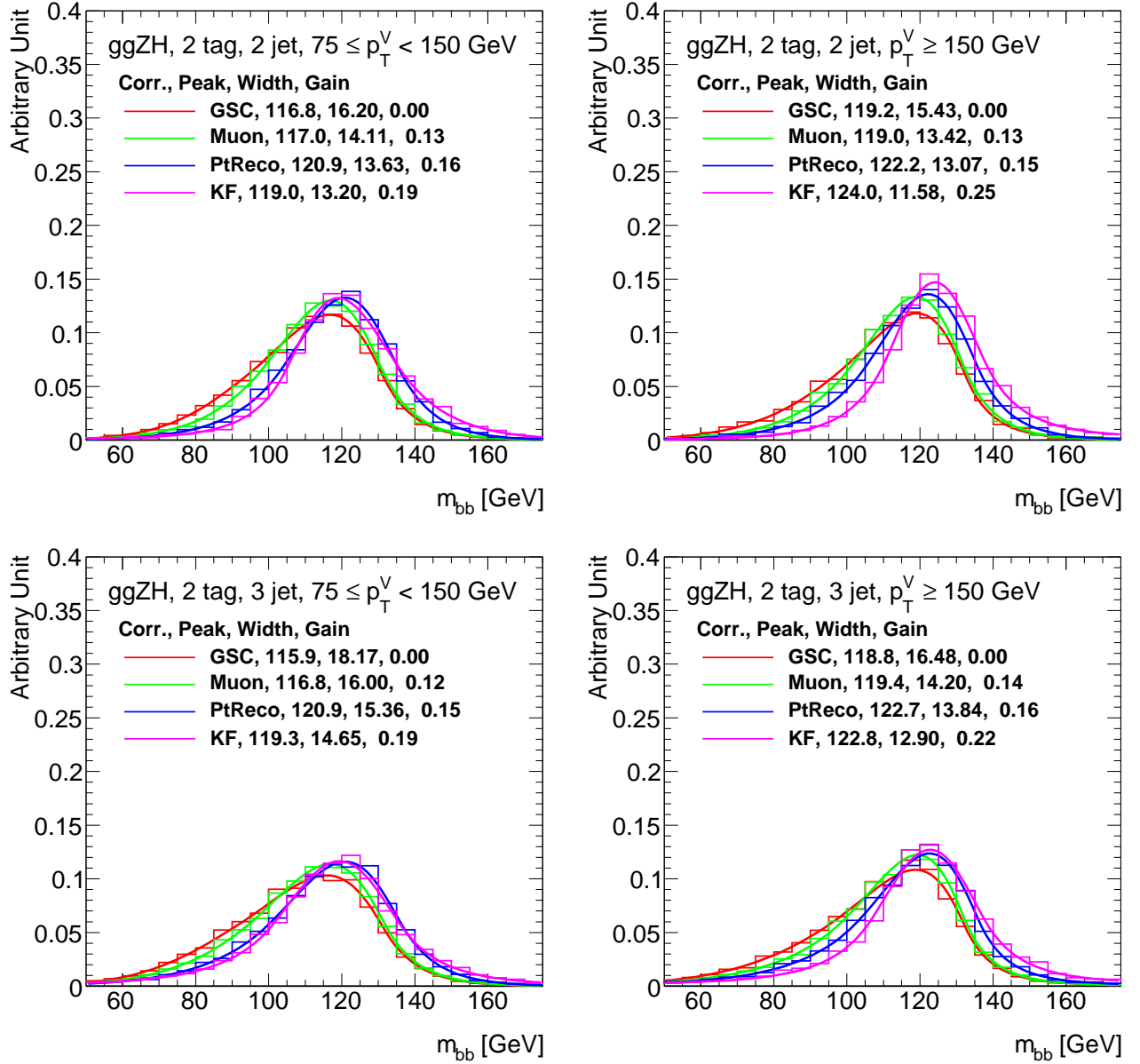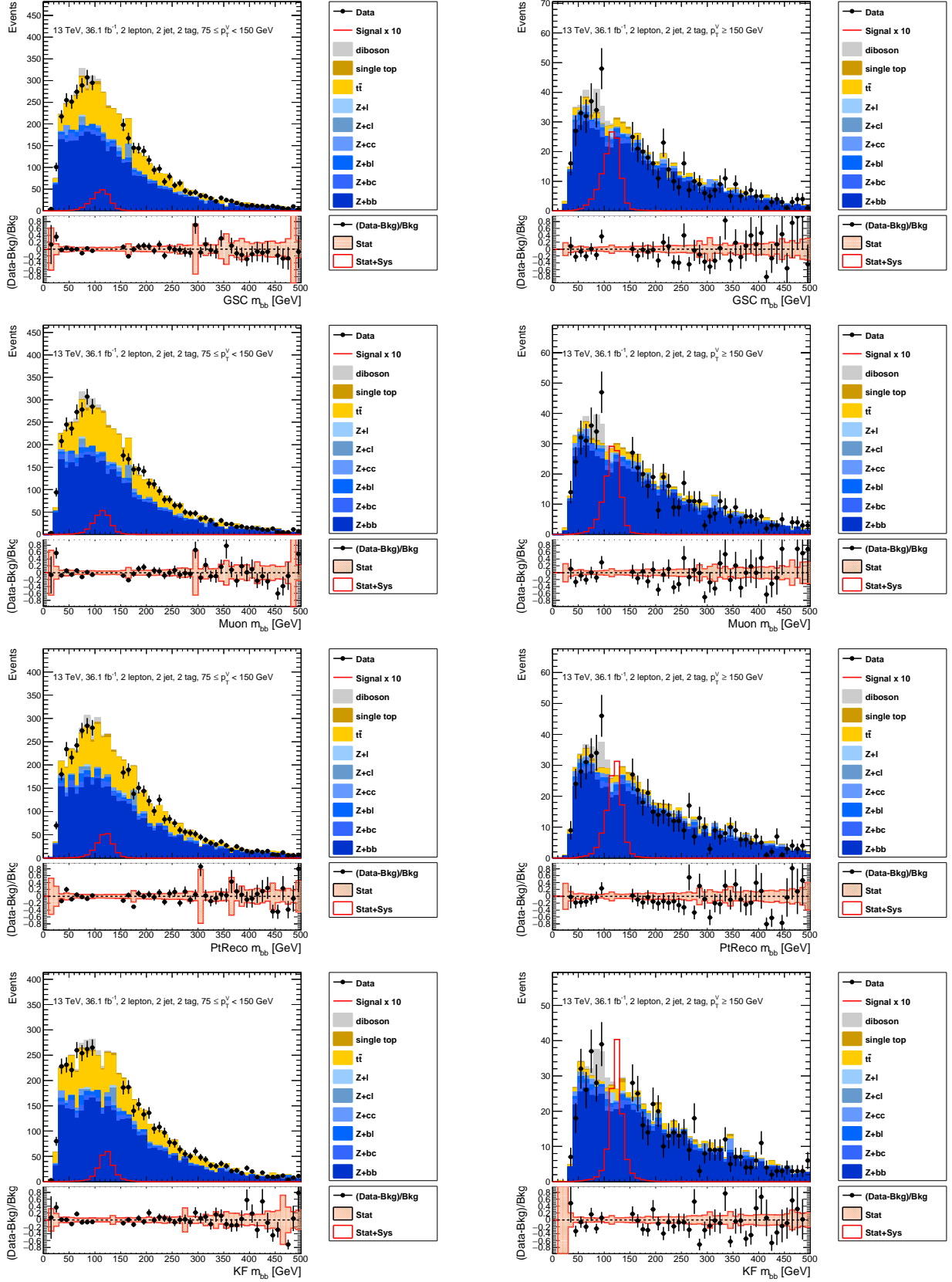
Figure 7.5 m_{bb} of $gg \rightarrow ZH$ comparing b-jet energy correction. 2 jet (left), 3 jet (right), $p_T^V = 75$–150 GeV (top), $p_T^V > 150$ GeV (bottom).

Figure 7.6 m_{bb} with various *b*-jet energy correction in 2 jet. $p_T^V = 75$–150 GeV (left) and $p_T^V = 75$–150 GeV (right). From top to bottom GSC, Muon, PtReco, KF. Data in $m_{bb} = 100$–150 GeV is blinded. Signal is scaled by 10. Z+HF and $t\bar{t}$ are scaled by the same factors in Section 11.1.
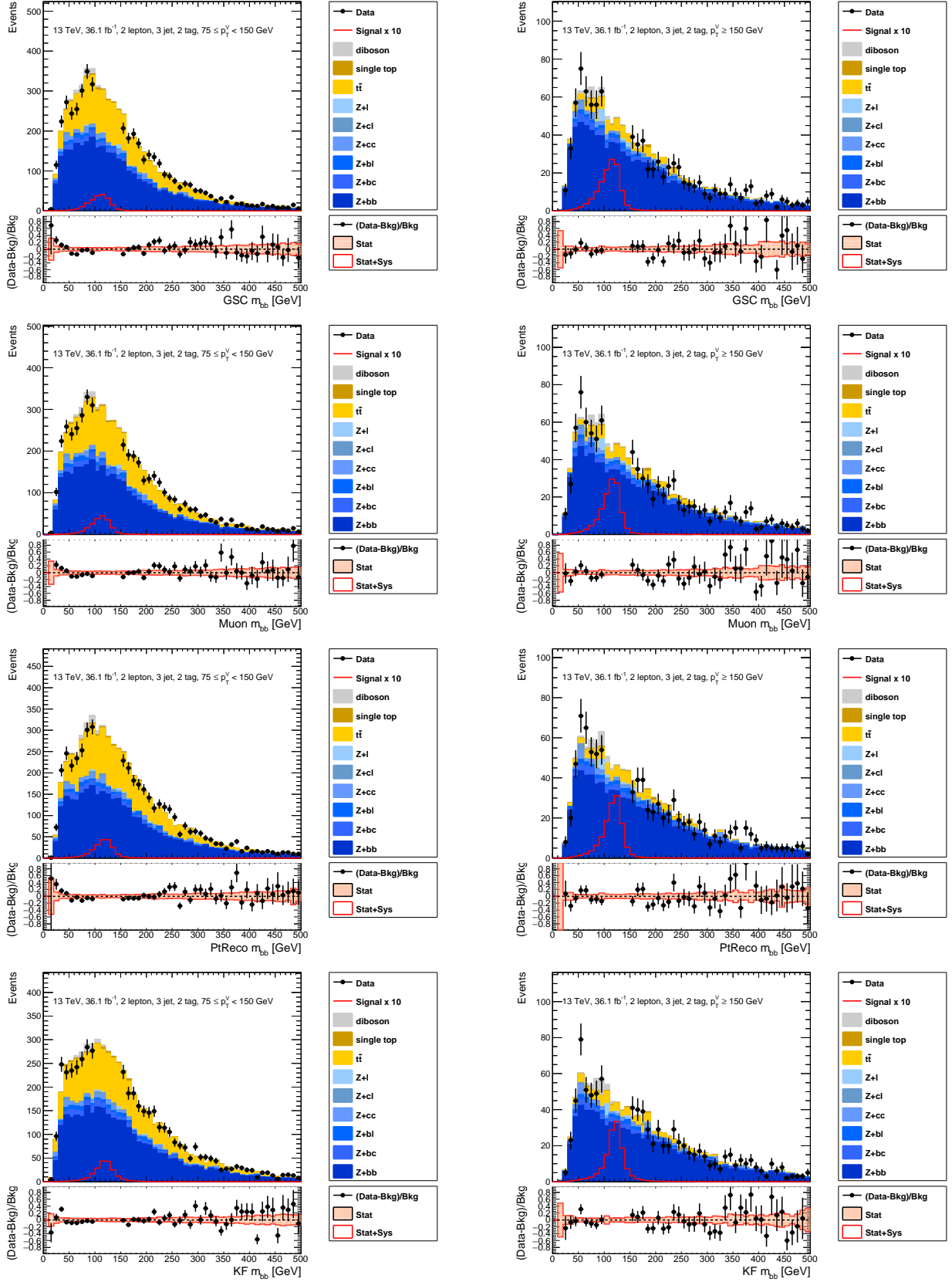
Figure 7.7 m_{bb} with various b-jet energy correction in 3 jet. $p_T^V = 75$–150 GeV (left) and $p_T^V = 75$–150 GeV (right). From top to bottom GSC, Muon, PtReco, KF. Data in $m_{bb} = 100$–150 GeV is blinded. Signal is scaled by 10. Z+HF and $t\bar{t}$ are scaled by the same factors in Section 11.1.
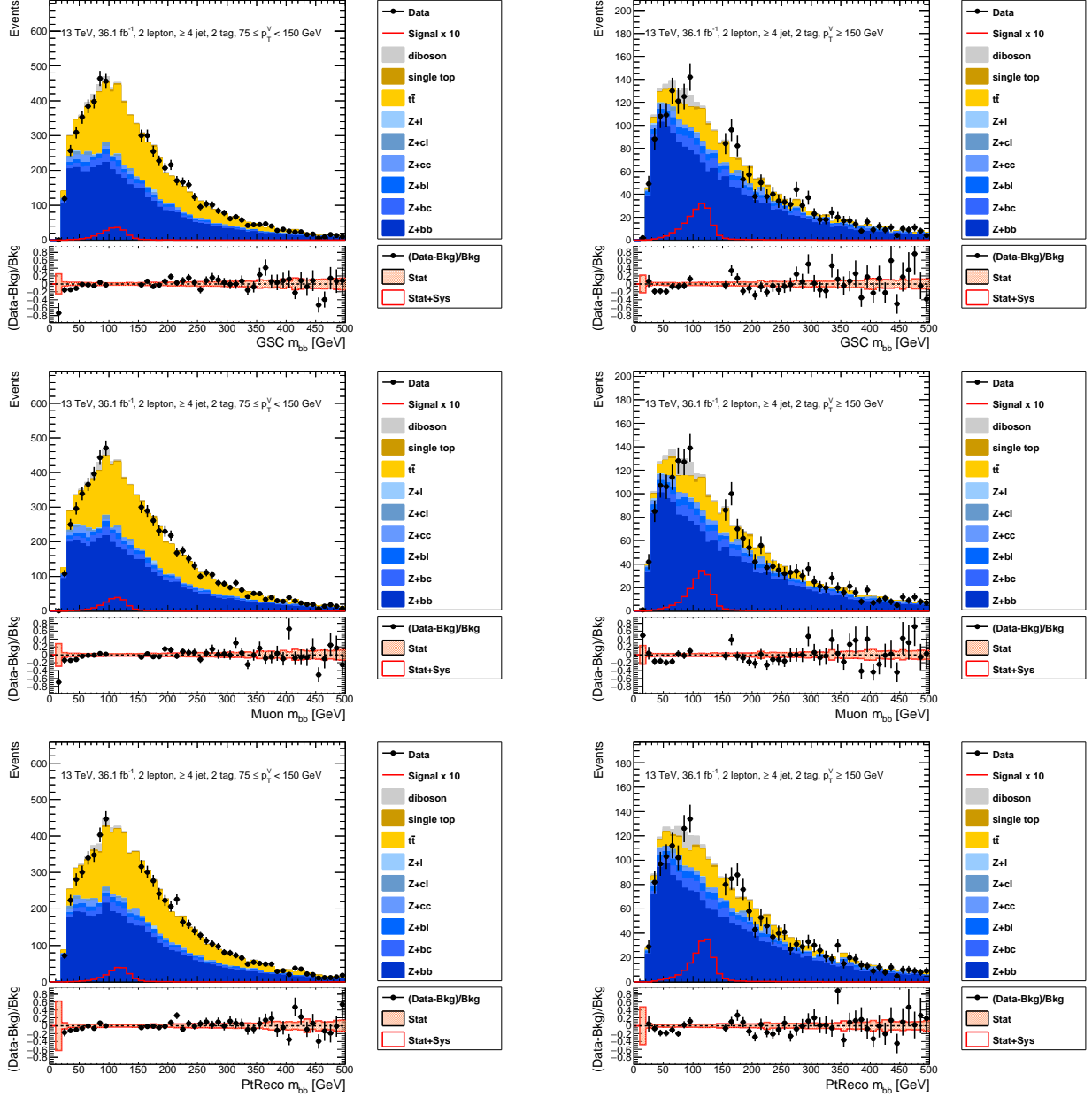
Figure 7.8 m_{bb} with various *b*-jet energy correction in ≥ 4 jet. $p_{\mathrm{T}}^{V} = 75$–150 GeV (left) and $p_{\mathrm{T}}^{V} = 75$–150 GeV (right). From top to bottom GSC, Muon, PtReco. Data in $m_{bb} = 100$–150 GeV is blinded. Signal is scaled by 10. $Z+$HF and $t\bar{t}$ are scaled by the same factors in Section 11.1.

p_T^V	Number of jets	GSC	Muon	PtReco	KF
75–150 GeV	2 jet	0.508	0.534	0.542	0.584
	3 jet	0.424	0.442	0.448	0.450
	$\geq$ 4 jet	0.339	0.352	0.358	-
150– GeV	2 jet	0.806	0.868	0.904	1.003
	3 jet	0.679	0.722	0.735	0.768
	$\geq$ 4 jet	0.551	0.578	0.589	-
	Combined	1.403	1.488	1.525	1.617

Table 7.1   Sensitivity of the m_{bb} distributions in the multivariate analysis with various b-jet energy correction. The sensitivity is calculated from the binned log likelihood ratio. PtReco is used for KF $\geq$ 4 jet events.

Chapter 8

Multivariate analysis

Multivariate analysis can improve the sensitivity by separating the signal and background efficiently, using several kinematic variables at the same time, instead of applying simple cuts on each variable. This analysis uses a multivariate technique called Boosted Decision Tree (BDT). In this chapter, the BDT is briefly reviewed in Section 8.1, input variables for the BDT are listed in Section 8.2, configuration of the BDT is described in Section 8.3, training and evaluation of the BDT are discussed in Section 8.4, transformation of the BDT output distributions (BDT_{VH}) is briefly summarized in Section 8.5, performance of the BDT is shown in Section 8.6.

8.1 Boosted Decision Tree

A toolkit for multivariate analysis (TMVA) is used to construct the BDT in this analysis [89]. The BDT uses several decision trees. The trees are made from the same training sample by reweighting events, and average of the individual trees is used as a single classifier. This stabilizes the response and enhance the performance. Each slit in each decision tree uses the best separating variable. Therefore, the same variables can be used in several nodes, and some variables may not be used at all. Thus, the decision trees are not affected by the useless variables. This is advantage compared to artificial neural networks in general. The leaf nodes, at the bottom of the trees, are labeled as signal or background, based on the majority of events.

8.2 Input Variables

Input variables used for the BDT are listed below.

- m_{bb}: Invariant mass of the 2 b-jets (Higgs boson candidate)
- $\Delta R(b, b)$: ΔR between the 2 b-jets
- p_T^{b1}: Transverse momentum of the leading b-jet
- p_T^{b2}: Transverse momentum of the 2nd leading b-jet
- $|\Delta\eta(V, H)|$: Difference of η between the Higgs boson candidate and the Z boson candidate
- $\Delta\phi(V, H)$: Azimuthal angle between the Higgs boson candidate and the Z boson candidate
- $m_{\ell\ell}$: Invariant mass of the 2 leptons (Z boson candidate)
- p_T^V: Transverse momentum of the Z boson candidate
- E_T^miss: Missing transverse momentum

For ≥ 3 jet events, additional variables below are used.

- p_T^{j3}: transverse momentum of the 3rd jet
- m_{bbj}: Invariant mass of the 2 b-jet and the 3rd jet

For 2 jet and 3 jet events, b-jet corrected with KF is used. For ≥ 4 jet events, b-jet corrected with PtReco is used. Appendix C shows comparison of data and simulation of the BDT input variables. Good agreement between data and simulation was found. Therefore, the variables can be used for the BDT.

The most powerful variable is the m_{bb} and $\Delta R(b,b)$. The other variables were added one by one if there was a gain in the sensitivity. Thus, the variables are optimized. The ranking of the input variables are derived from number of times the variables were used to split nodes in decision trees, considering each split weight based on separation gain and number of events. The ranking in the most sensitive 2 jet $p_T^V = 150–$ GeV region is: m_{bb}, $\Delta R(b,b)$, $\Delta \eta(V,H)$, p_T^{b2}, $\Delta \phi(V,H)$, p_T^V, E_T^{miss}, p_T^{b1}, $m_{\ell\ell}$.

Correlation between the BDT input variables were also studied. For example, the correlation between $\Delta R(b,b)$ and p_T^V is shown in Figure 8.1. Signal has negative correlation between $\Delta R(b,b)$ and p_T^V, p_T^{b1}, p_T^{b2} while background does not. Such difference in correlation is also used in the BDT automatically.

8.3 Configuration

Configuration of the BDT training parameters are listed below.

- Boosting type for the trees (BoostType): AdaBoost
- Learning rate for the AdaBoost algorithm (AdaBoostBeta): 0.15
- Node splitting separation criteria (SeparationType): GiniIndex
- Method for pruning of statistically insignificant branches (PruneMethod): NoPruning
- Number of trees (NTrees): 200
- Maximum depth of trees (MaxDepth): 4
- Number of cuts tested for the optimization in each node (nCuts): 100
- Minimum number of events in each node (nEventsMin): 5%

These were optimized in Run1 [10]. Each parameter was scanned to obtain optimal performance. It was found that they are also optimal in Run2 [90].

8.4 Training and Evaluation

The BDT is trained and evaluated in each analysis region using simulated samples. Pile-up reweighting and truth tagging is applied for the training. Truth tagging is to obtain statistics for small acceptance samples as written in Section 5.6. In order to avoid using the same samples for the training and evaluation, sample sets are separated into two samples A and B. Then, the BDT trained on sample A (B) are evaluated on sample B (A). No over-training effect was found comparing the BDT output distributions of training samples and test samples. Finally, the BDT output distributions of sample A and B are merged.

8.5 Transformation

The BDT output distributions are transformed in order to have smoother background distribution and keep finer binning in high sensitivity region. The transformation was established in Run1 and optimized for the

sensitivity [91]. The procedure starts from very fine binning, and merges bins from high sensitivity region. The statistical uncertainty of the total background is required to be less than 20% in each bin.

8.6   Performance

Figure 8.2 shows performance of the BDT_{VH} separating $t\bar{t}$ background using $E_\mathrm{T}^\mathrm{miss}$ as an example. tt has larger $E_\mathrm{T}^\mathrm{miss}$ compared to signal and thus separated to low BDT region. Figure 8.3 shows the BDT_{VH} distribution of the multivariate analysis. Good agreement between data and simulation was found in the low BDT region. Table 8.1 shows the sensitivity of the m_{bb} distributions in the cut-based analysis. Table 8.2 shows the sensitivity of the BDT_{VH} distributions in the multivariate analysis. The sensitivity of the multivariate analysis is about 20% higher than the cut-based analysis.

p_T^V	Number of jets	Sensitivity
75–150 GeV	2 jet	0.633
	3 jet	0.498
	≥ 4 jet	0.406
150–200 GeV	2 jet	0.638
	3 jet	0.511
	≥ 4 jet	0.424
200– GeV	2 jet	1.032
	3 jet	0.764
	≥ 4 jet	0.493
	Combined	1.885

Table 8.1   Sensitivity of the m_{bb} distributions in the cut-based analysis. The sensitivity is calculated from the binned log likelihood ratio.

p_T^V	Number of jets	Sensitivity
75–150 GeV	2 jet	0.856
	3 jet	0.672
	≥ 4 jet	0.532
150– GeV	2 jet	1.439
	3 jet	1.089
	≥ 4 jet	0.884
	Combined	2.346

Table 8.2   Sensitivity of BDT_{VH} distributions in the multivariate analysis. The sensitivity is calculated from the binned log likelihood ratio.
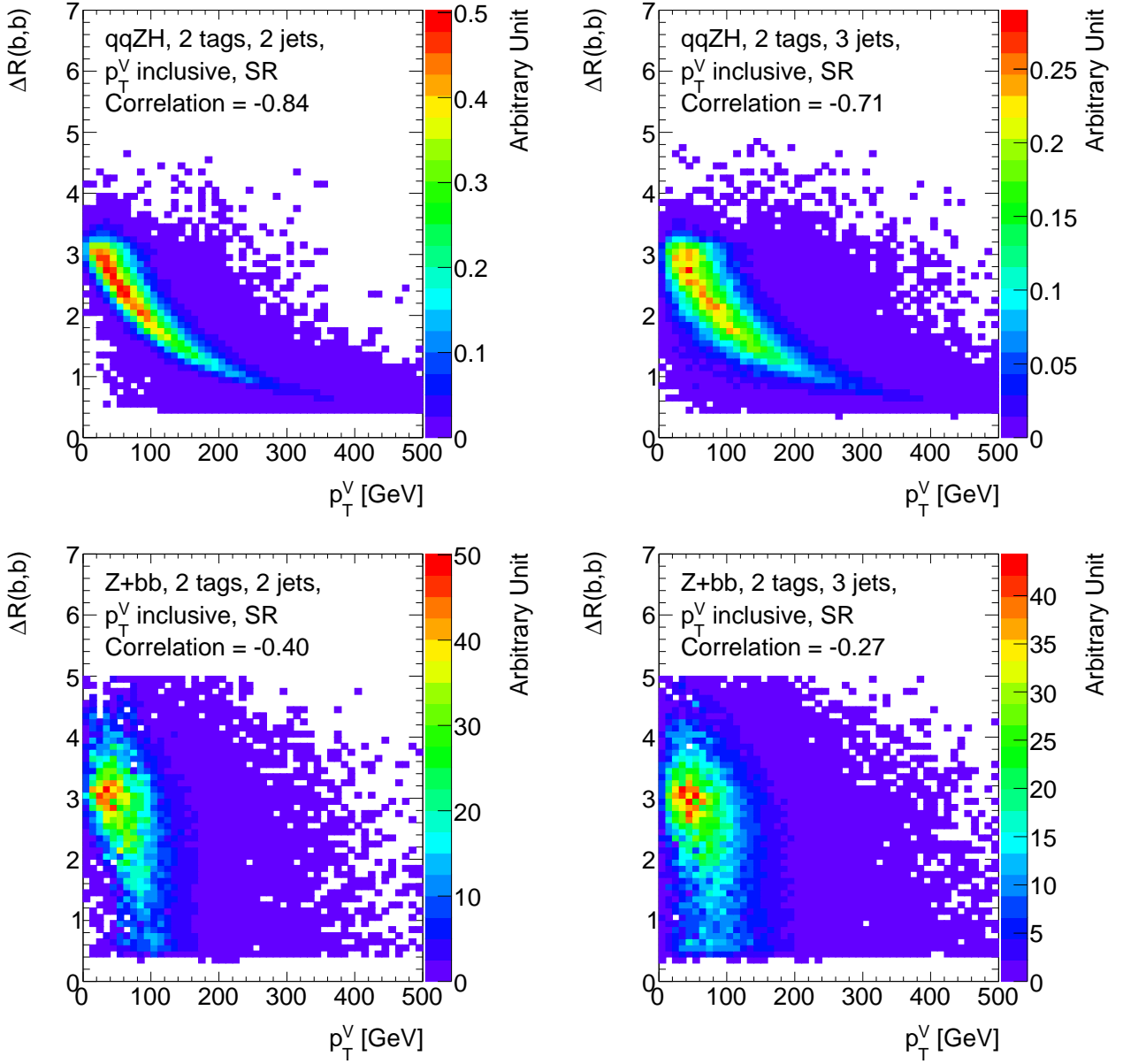
Figure 8.1 Correlation between $\Delta R(b, b)$ and p_{T}^{V}. 2 jet (left) and 3 jet (right). $qqZH$ (top) and $Z + bb$ (bottom).
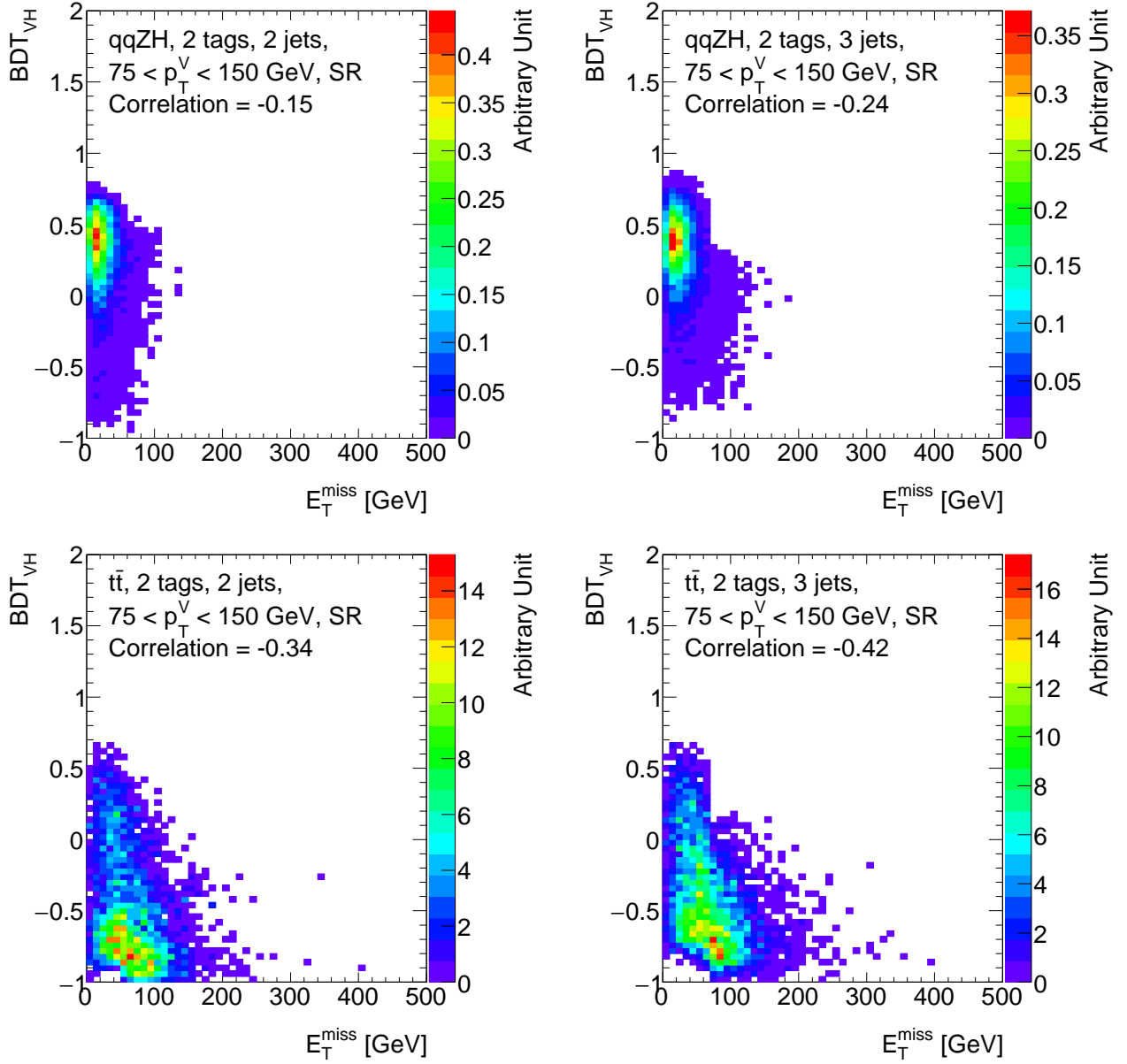
Figure 8.2   Performance of the BDT$_{VH}$ separating $t\bar{t}$ background using E_T^{miss}. 2 jet (left) and 3 jet (right). $qqZH$ (top) and $t\bar{t}$ (bottom).
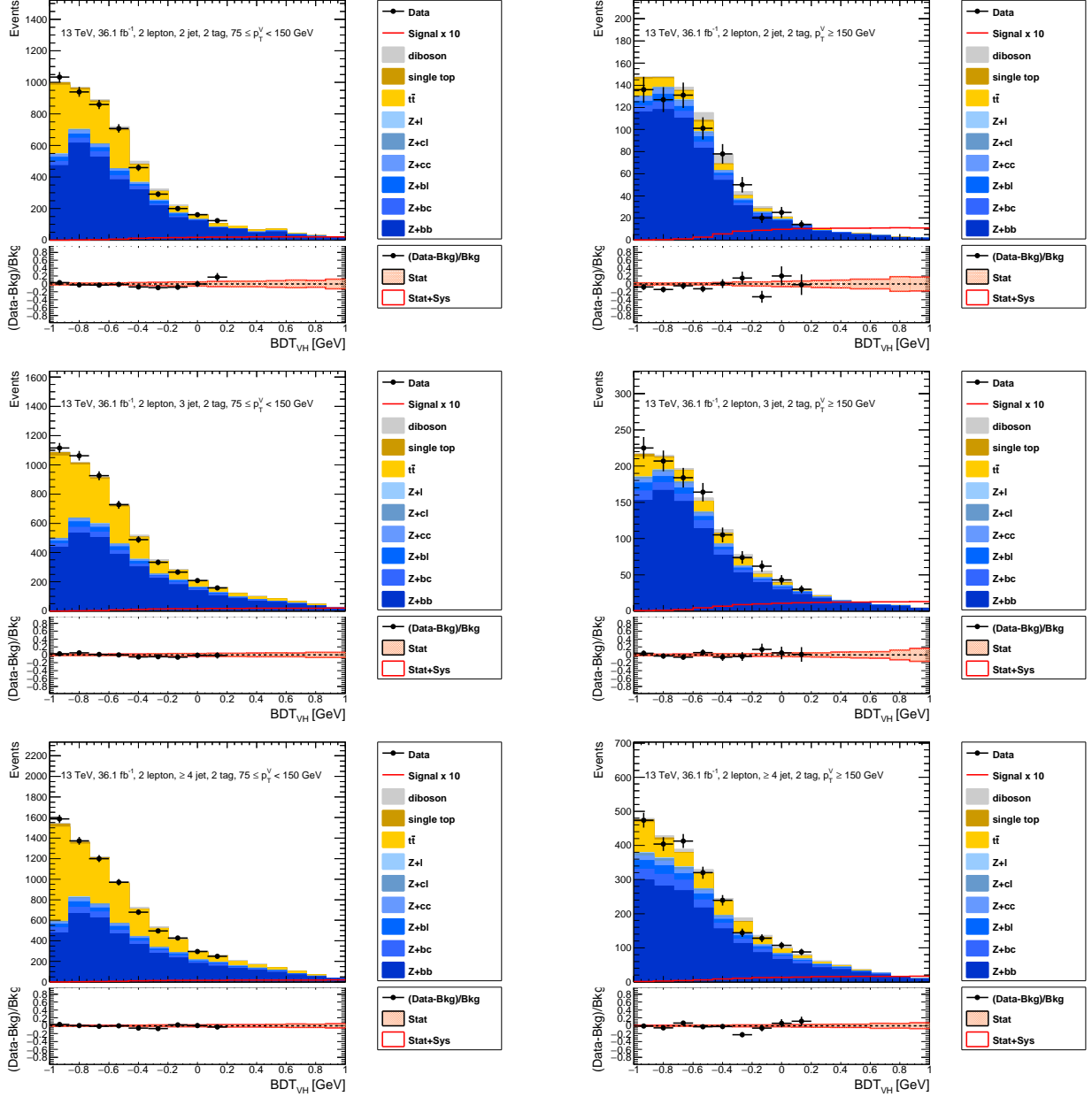
Figure 8.3   The BDT$_{VH}$ distributions of the multivariate analysis. $p_\mathrm{T}^V = 75$–150 GeV (left) and $p_\mathrm{T}^V = 150$– GeV (right). From top to bottom 2 jet, 3 jet, ≥ 4 jet. Data in high BDT$_{VH}$ 6 bins are blinded. Signal is scaled by 10. $Z+$HF and $t\bar{t}$ are scaled by the same factors in Section 11.1.

Chapter 9

Systematic uncertainties

This analysis searches for an excess of events over background and measure the signal strength. The results are affected by systematic uncertainties. Therefore, it is important to assess the systematic uncertainties. The systematic uncertainties are categorized into 3 groups: experimental uncertainties, background modeling uncertainties, and signal modeling uncertainties. In this chapter, experimental uncertainties, background modeling uncertainties and signal modeling uncertainties, are summarized in Section 9.1, 9.2 and 9.3 respectively.

9.1 Experimental uncertainties

Experimental uncertainties are estimated and grouped into uncorrelated components. Each component is varied as systematic variations of the analysis and propagated to the final results. There are 2 types of systematic variations. One reselects events and the other reweights events. For example, systematic variations for jet energy scale shift the jet energy scale by ± 1 standard deviation and events can migrate among regions, while systematic variations for b-tag efficiency shift the efficiency weight by ± 1 standard deviation without event migration. There are 61 variations for the experimental uncertainties. Table 9.1 shows 23 variations for beam, electrons, muons. Table 9.2 shows 38 variations for jets, b-tag and $E_{\mathrm{T}}^{\mathrm{miss}}$.

Luminosity is measured using several luminosity detectors [19]. Main sources of the uncertainty are instrumental effects and beam conditions. The uncertainty is 3.2%. Average number of interactions of simulation is scaled by a factor of 1.09 to improve the agreement of number of vertices. The uncertainty on pileup reweighting is estimated by varying the correction to 1.00 and 1.18.

Electron efficiency was measured using tag-and-probe method of Z and J/ψ [77]. Main source of the uncertainty is background estimation in the analysis. The uncertainty is a few% in $E_{\mathrm{T}} < 20$ GeV and less than 1% at $E_{\mathrm{T}} \geq 20$ GeV. Electron energy calibration was performed using $Z \to ee$ events [79]. Main source of the uncertainty is calibration of the calorimeter layers. The uncertainty is less than 1%.

Muon performance was measured using tag-and-probe method of Z and J/ψ [80]. Reconstruction efficiency was found to be 99% level. The uncertainty is less than 1%. Main source of the uncertainty is assigned for possible bias in the tag-and-probe, comparing efficiency in the tag-and-probe and efficiency of the generator level muons. Muon momentum scale was also measured. Main sources of the uncertainty are mass window width, background estimation in the analysis. The uncertainty is less than 1%.

JVT efficiency is measured using $Z(\to \mu\mu)$+jets events[83]. Main sources of uncertainties are generators differences and mis-modeling in $d\phi(Z, \mathrm{jet})$. The uncertainty is less than 2%. Jet energy scale is calibrated using simulation and in-situ techniques [81]. In situ techniques are based on transverse momentum balance between a

jet and well measured objects. Main source of the uncertainty is the pile-up correction. Additional uncertainty is considered for b-jets and c-jets. The uncertainty is about 4.5% for $p_{\mathrm{T}} = 20$ GeV, and less than 1% for jets with $100 < p_{\mathrm{T}} < 500$ GeV in the central region. Jet energy resolution was measured in Run1 and extrapolated for Run2 [92]. Main sources of the uncertainty are noise term and the extrapolation. The uncertainty is about 4% at $p_{\mathrm{T}} = 20$ GeV and less than 1% in $p_{\mathrm{T}} > 200$ GeV.

The b-tagging efficiency was measured using similar ways as Run1 [84]. Main sources of the uncertainty are uncertainties on $t\bar{t}$ modeling, background estimation, jet energy scale and jet energy resolution. No correlation between uncertainties on b-tagging efficiency and jet energy was found in this analysis. Therefore, the uncertainties are assigned separately in this analysis. The uncertainty is about 2% for b-jets, 10% for c-jets and 30% for light-jets. These are the largest experimental uncertainties in this analysis.

The $E_{\mathrm{T}}^{\mathrm{miss}}$ performance is evaluated using simulation [93]. Systematic uncertainties on electron, muon, jets are propagated through the $E_{\mathrm{T}}^{\mathrm{miss}}$ calculation. Main source of uncertainty on the soft term is the generator uncertainty. The uncertainty is about 10%.

9.2   Background modeling uncertainties

Data and simulated samples are used to model background in this analysis. Nominal samples are summarized in Table 4.1. Main backgrounds are Z+jets, $t\bar{t}$, diboson, single-top. Systematic uncertainties on the background modeling are estimated by comparing nominal and alternative samples, or comparing nominal samples and data in the CR. The RIVET framework is also used for particle level comparisons [94].

The background modeling uncertainties are summarized in Table 9.3 and 9.4. There are 3 types of uncertainties:

- Normalization uncertainties
- Acceptance uncertainties
- Shape uncertainties

Normalization uncertainties are floated for V+HF and $t\bar{t}$, and estimated for diboson and single-top comparing nominal and alternative samples. Acceptance uncertainties describes the relative normalization between regions. Differences in Double Ratio:

$$\frac{\mathrm{Acceptance}_{\mathrm{Region1}}^{\mathrm{Nominal}}}{\mathrm{Acceptance}_{\mathrm{Region2}}^{\mathrm{Nominal}}} / \frac{\mathrm{Acceptance}_{\mathrm{Region1}}^{\mathrm{Alternative}}}{\mathrm{Acceptance}_{\mathrm{Region2}}^{\mathrm{Alternative}}} \tag{9.1}$$

are added in quadrature to estimate the uncertainty. Shape uncertainties are estimated for m_{bb} and p_{T}^V in each region. The largest difference alternative sample shape is used. Shape uncertainties for the other variables were found to be covered by m_{bb} and p_{T}^V.

V+jets are separated into 3 groups, V+HF, $V + cl$, $V + ll$. V+HF is composed of $V + bb$, $V + bl$, $V + bc$ and $V + cc$. V+HF normalization is floated in 2 jet and $3 \geq$ jet separately. Uncertainty on V+HF composition is assigned as uncertainties on $V + bc$ / $V + bb$ ratio, $V + bl$ / $V + bb$ ratio, $V + cc$ / $V + bb$ ratio, in 2 jet and $3 \geq$ jet separately. Only normalization uncertainty is considered for $V + cl$ and $V + ll$, since the contributions are less than 1% of total background. For normalization and acceptance uncertainties, nominal SHERPA 2.2.1 is compared to the scale variations and alternative sample. The scale variations are:

- Renormalization scale (μ_R): 0.5 and 2.0
- Factorisation scale (μ_F): 0.5 and 2.0

- Parton shower resummation scale: 0.5 and 2.0
- CKKW merging scale: 30 GeV and 15 GeV

The alternative sample is generated with MADGRAPH5_aMC@NLO+PYTHIA8 [95]. Shape uncertainties are estimated for Z+HF and W+HF. For Z+HF, difference between nominal and data in the m_{bb} sideband is used. The $t\bar{t}$ contamination is reduced by the same $E_{\mathrm{T}}^{\mathrm{miss}}/\sqrt{S_{\mathrm{T}}} < 3.5$ cut in the cut-based analysis. Remaining $t\bar{t}$ is subtracted using simulation. Shape uncertainties for potential mis-modeling is parameterized approximately:

- p_{T}^V: $\pm$ 0.2 $\log_{10}$ (p_{T}^V / 50) - 0.07, constant below 10 GeV
- m_{bb}: $\pm$ 0.0005 (m_{bb} - 100), constant above 300 GeV

For W+HF, the same variations as normalization are also used for shape, since it is hard to have high purity CR. The shape uncertainties are dominated by the alternative sample and linear fits are used to parameterize the uncertainties approximately:

- p_{T}^V: $\pm$ 0.7 + 0.0013 p_{T}^V - 1, constant above 500 GeV
- m_{bb}: $\pm$ 0.8 + 0.0013 m_{bb} - 1, constant above 400 GeV

The $t\bar{t}$ uncertainties are estimated comparing nominal sample, POWHEG+PYTHIA8, and alternative samples. The alternative samples are:

- POWHEG+HERWIG7: Different parton shower sample [96]
- MADGRAPH5_aMC@NLO+PYTHIA8: Different generator sample
- POWHEG+PYTHIA8: Increased and decreased radiation samples

Normalization is floated in 2 jet and $3 \geq$ jet separately, and constrained by the data in the top $e\mu$ CR. Shape uncertainties are dominated by MADGRAPH5_aMC@NLO+PYTHIA8.

Single-top uncertainties are estimated using alternative samples. s-channel is less than 1% of total background therefore only normalization uncertainty is considered. For Wt and t-channel, nominal sample, POWHEG+PYTHIA6 are compared to alternative samples. The alternative samples are:

- POWHEG+HERWIG++: Different parton shower sample
- MADGRAPH5_aMC@NLO+HERWIG++: Different generator sample
- POWHEG+PYTHIA6: Increased and decreased radiation samples

For Wt, uncertainty on the interference between Wt and $t\bar{t}$ are estimated by diagram subtraction scheme instead of diagram removal scheme [97]. Acceptance uncertainties are estimated for 2 jet and $3 \geq$ jet. Shape uncertainties are dominated by the interference for Wt and parton shower for t-channel.

Diboson uncertainties are estimated using alternative samples. WW is less than 1% of total background therefore only normalization uncertainty is considered. For ZZ and WZ, nominal sample SHERPA 2.2.1 is compared to the scale variations and alternative samples. A jet binning method is used to estimate acceptance uncertainty from the scale variations [98]. The alternative samples are:

- POWHEG+PYTHIA8: Different parton shower samples
- POWHEG+HERWIG++: Different parton shower sample

These are used to estimate acceptance and shape uncertainties from Parton Shower and Underlying Event (PSUE).

Powheg+Pythia8 is also used to estimate shape uncertainties from Matrix Element (ME) generator. p_{T}^V shape variation for the ME was found to be negligible. PDF+α_{S} variations were found to be negligible.

9.3 Signal modeling uncertainties

Signal uncertainties are summarized in Table 9.5. Uncertainties on cross-section and branching ratio are assigned following the latest recommendation of the LHC Higgs Cross-section working group [24]. Cross-section uncertainty from missing higher-order QCD calculation is estimated by the scale variations:

- Renormalization scale: 0.33 and 3.0
- Factorisation scale: 0.33 and 3.0

The latest recommendation does not treat $qqZH$ and $ggZH$ separately. Therefore, in order to estimate cross-section uncertainty from the scale separately for $qqZH$ and $ggZH$, $qqZH$ cross-section uncertainty is assumed to be the same as $qqWH$. Then, $ggZH$ cross-section uncertainty is estimated from the total and $qqZH$ cross-section uncertainties. Cross-section uncertainties from PDF+α_{S} are estimated using variations of a PDF set [41]. However, the assumption used for the scale can not be used for the PDF+α_{S} since it is larger for $qqWH$. Therefore, uncertainty on $ggZH$ cross-section from PDF+α_{S} is taken from the previous recommendation [99]. Uncertainty on the branching ratio is assigned to be 1.7%. This is from uncertainties on missing higher order QCD and EW calculations, b quark mass and α_{S}. Acceptance uncertainties are estimated using the scale variations and alternative samples. The same jet binning method as diboson is used to estimate acceptance uncertainty from the scale variations [98]. The alternative samples are:

- Powheg+MiNLO+Pythia8: Different parton shower samples
- Powheg+MiNLO+Herwig++: Different parton shower sample
- Madgraph5_aMC@NLO+Pythia8:

These are used to estimate Parton Shower and Underlying Event (PSUE) uncertainties for acceptance and shape. PDF+α_{S} uncertainties are also estimated for acceptance and shape following PDF4LHC recommendations [41]. m_{bb} shape variation for the PDF+α_{S} was found to be negligible. Uncertainty on the NLO EW correction factor for $qqZH$ as a function of p_{T}^V is also assigned [47].

Table 9.1   Systematic variations for uncertainty on beam, electrons and muons. There are 2 variations for beam, 6 variations for electrons, and 15 variations for muons.

Beam
Uncertainties on integrated luminosity
Uncertainties on pile-up reweighting
Electron
Uncertainties on trigger efficiency
Uncertainties on reconstruction efficiency
Uncertainties on identification efficiency
Uncertainties on isolation efficiency
Uncertainties on energy scale
Uncertainties on energy resolution
Muon
Uncertainties on trigger efficiency (stat)
Uncertainties on trigger efficiency (syst)
Uncertainties on reconstruction and identification efficiency for $p_T \geq 15$ GeV (stat)
Uncertainties on reconstruction and identification efficiency for $p_T \geq 15$ GeV (syst)
Uncertainties on reconstruction and identification efficiency for $p_T < 15$ GeV (stat)
Uncertainties on reconstruction and identification efficiency for $p_T < 15$ GeV (syst)
Uncertainties on isolation efficiency (stat)
Uncertainties on isolation efficiency (syst)
Uncertainties on track-to-vertex association efficiency (stat)
Uncertainties on track-to-vertex association efficiency (syst)
Uncertainties on momentum scale
Uncertainties on charge dependent momentum scale (rho)
Uncertainties on charge dependent momentum scale (rebias)
Uncertainties on momentum resolution (ID)
Uncertainties on momentum resolution (MS)

Table 9.2 Systematic variations for uncertainties on jets, b-tag and $E_{\mathrm{T}}^{\mathrm{miss}}$. There are 22 variations for jets, 13 variations for b-tag, 3 variations for $E_{\mathrm{T}}^{\mathrm{miss}}$.

Jet
Uncertainties on JVT efficiency
Uncertainties on jet energy scale from the in situ analysis, 8 variations
Uncertainties on jet energy scale from η-intercalibration (modeling)
Uncertainties on jet energy scale from η-intercalibration (statistics)
Uncertainties on jet energy scale from η-intercalibration (non-closure)
Uncertainties on jet energy scale from pile-up (offset mu)
Uncertainties on jet energy scale from pile-up (offset NPV)
Uncertainties on jet energy scale from pile-up (p_{T} term)
Uncertainties on jet energy scale from pile-up (ρ topology)
Uncertainties on jet energy scale from sample's flavour composition
Uncertainties on jet energy scale from sample's flavour response
Uncertainties on jet energy scale from b-jet responce
Uncertainties on jet energy scale from punch-through jets
Uncertainties on jet energy scale from the behaviour of high-p_{T} jets
Uncertainties on jet energy resolution
b-tag
Uncertainties on efficiency for b-jets, 3 variations
Uncertainties on efficiency for c-jets, 3 variations
Uncertainties on efficiency for light-jets, 5 variations
Uncertainties on efficiency extrapolation to high p_T jets
Uncertainties on efficiency for tau jets
$E_{\mathrm{T}}^{\mathrm{miss}}$
Uncertainties on track-based soft term longitudinal resolution
Uncertainties on track-based soft term transverse resolution
Uncertainties on track-based soft term longitudinal scale

Table 9.3   Systematic uncertainties on Z+HF, W+HF, $t\bar{t}$ and single top. Z+HF and $t\bar{t}$ normalization is floated in 2 jet and $3 \geq$ jet separately.

Z+jets	
Z+HF normalization	Float
$Z + bc$ / $Z + bb$ ratio	30–40%
$Z + bl$ / $Z + bb$ ratio	20–25%
$Z + cc$ / $Z + bb$ ratio	13–15%
$Z + cl$ normalization	23%
$Z + ll$ normalization	18%
p_T^V and m_{bb} distributions	Shape
W+jets	
W+HF normalization	Float
$W + bc$ / $W + bb$ ratio	15–30%
$W + bl$ / $W + bb$ ratio	23–26%
$W + cc$ / $W + bb$ ratio	10–30%
$W + cl$ normalization	37%
$W + ll$ normalization	32%
p_T^V and m_{bb} distributions	Shape
$t\bar{t}$	
$t\bar{t}$ Normalization	Float
p_T^V and m_{bb} distributions	Shape
Single-top	
s-channel normalization	4.6%
t-channel normalization	4.4%
t-channel acceptance	17–20%
Wt normalization	6.2%
Wt acceptance	35–41%
p_T^V and m_{bb} distributions	Shape

Table 9.4   Systematic uncertainties on diboson. WW is less than 1% of total background therefore only normalization uncertainty is considered. VZ the systematic uncertainties are correlated for ZZ and WZ. PDF+α_S variations were found to be negligible. p_T^V shape variation for the ME was found to be negligible.

ZZ	
Normalization	20%
Acceptance (scale)	10–18%
Acceptance (PSUE)	3–6%
WZ	
Normalization	26%
Acceptance (scale)	13–21%
Acceptance (PSUE)	4–11%
VZ	
p_T^V and m_{bb} distribution (scale)	Shape
p_T^V and m_{bb} distribution (PSUE)	Shape
m_{bb} distribution (ME)	Shape
WW	
Normalization	25%

Table 9.5 Systematic uncertainties on signal. Uncertainties on cross-section and branching ratio are assigned following the latest recommendation of the LHC Higgs Cross-section working group [24]. m_{bb} shape variation for the PDF+α_S was found to be negligible.

$qq \to ZH$	
Cross-section (scale)	0.7%
Cross-section (PDF+α_S)	1.6%
Acceptance (scale)	2.5–8.8%
Acceptance (PSUE)	10–14%
Acceptance (PDF+α_S)	0.5–1.3%
p_T^V and m_{bb} distributions (scale)	Shape
p_T^V and m_{bb} distributions (PSUE)	Shape
p_T^V distributions (PDF+α_S)	Shape
p_T^V distribution (NLO EW)	Shape
$gg \to ZH$	
Cross-section (scale)	27%
Cross-section (PDF+α_S)	5%
Acceptance (scale)	2.5–8.8%
Acceptance (PSUE)	10–14%
Acceptance (PDF+α_S)	0.5–1.3%
p_T^V and m_{bb} distributions (scale)	Shape
p_T^V and m_{bb} distributions (PSUE)	Shape
p_T^V distributions (PDF+α_S)	Shape
ZH	
Branching ratio	1.7%

Chapter 10

Statistical analysis

In order to test background only hypothesis and measure the signal strength, a maximum likelihood fit is performed. Since the fit results are final results of this analysis, it is important to describe and validate the fit before looking at the results. In this chapter, the likelihood is described in Section 10.1, configuration of the fit is summarized in Section 10.2, validation of the fit is discussed in Section 10.3.

10.1 Likelihood

This analysis uses RooStats framework to build likelihood [100]. The likelihood can be written as:

$$L(\mu, \boldsymbol{\theta}) = \prod_{i \in bins} P(n_i | \mu s_i(\boldsymbol{\theta}) + b_i(\boldsymbol{\theta})) \prod_{j \in \boldsymbol{\theta}} G(\theta_j), \tag{10.1}$$

where P is the Poisson probability and for each bin of BDT_{VH} or m_{bb} distributions, and G is penalty terms for the systematic uncertainties. The systematic uncertainties are included as Nuisance Parameters (NP), $\boldsymbol{\theta}$. The NP are constrained by normal or log normal distributions. The log normal is used for normalisation uncertainties to avoid negative normalisation. The penalty terms are added to decrease the likelihood, when a fit value of the NP deviate from the nominal value. Statistical uncertainties of simulated samples are also included as NP per bin [101].

A test statistic q_μ is defined using the profile likelihood ratio [102]:

$$q_\mu = -2 \ln(\mathcal{L}(\mu, \hat{\hat{\boldsymbol{\theta}}}_{\boldsymbol{\mu}}) / \mathcal{L}(\hat{\mu}, \hat{\boldsymbol{\theta}})), \tag{10.2}$$

where $\hat{\hat{\boldsymbol{\theta}}}$ is the NP that maximize the likelihood for hypothesized μ, and $\hat{\boldsymbol{\theta}}$ and $\hat{\mu}$ are the NP and the signal strength that maximize the likelihood. Therefore, large q_μ means data is incompatible with the hypothesized μ. The disagreement between data and the hypothesized μ is quantified by the p-value.

$$p_\mu = \int_{q_{\mu,obs}}^{\infty} f(q_\mu, \mu) dq_\mu, \tag{10.3}$$

Where $q_{\mu,obs}$ is observed q_μ and $f(q_\mu, \mu)$ is PDF of q_μ.

Then, p_0 is used to test background only hypothesis, and derive probability of background only hypothesis. When p_0 is small, probability of background only hypothesis is small, and the excess is significant. For example $p_0 = 2.87 \times 10^{-7}$ corresponds to 5 standard deviations of Gaussian significance. If no excess is found, exclusion intervals with the CLs technique is reported [103]. If an excess is found, observed significance, expected significance, and the signal strength are reported. The expected significance are determined using simulation with all NP set at the fit value, but signal strength set at nominal.

		Multivariate analysis		Cut-based analysis	
	pTV	2 jet	$\geq$ 3 jet	2 jet	$\geq$ 3 jet
SR	pTV = 75–150 GeV	BDT$_{VH}$	BDT$_{VH}$	m_{bb}	m_{bb}
	pTV = 150–200 GeV	BDT$_{VH}$	BDT$_{VH}$	m_{bb}	m_{bb}
	pTV = 200– GeV			m_{bb}	m_{bb}
CR	pTV = 75–150 GeV	m_{bb}	m_{bb}	m_{bb}	m_{bb}
	pTV = 150–200 GeV	Yield	m_{bb}	Yield	m_{bb}
	pTV = 200– GeV				

Table 10.1   Regions and distributions used in the fit. Multivariate analysis (left) and cut-based analysis (right).

10.2   Configuration

Systematic variations with possible event migration between regions, such as jet energy scale systematic variations, are smoothed in order to avoid additional statistical effect on the systematic uncertainties. At first, bins from a extrema to the next are merged, to have no local extrema in the BDT$_{VH}$, or up to 1 local extrema in the m_{bb}. Then, bins are merged from right side, to have the statistical uncertainty less than 5%. It was found that there is no bias from the smoothing.

Systematic variations with negligible impact on the results are pruned in each region. Normalization uncertainty is removed if the variation is less than 0.5%, or the $\pm 1\sigma$ variations are in the same sign. Shape uncertainty is removed if the variation is less than 0.5% in all bins, or if only one of $\pm 1\sigma$ variations is non-zero. Normalization and shape uncertainties are removed if a sample is less than 2% of total background. It was found that there is no bias from the pruning.

Regions and distributions used in the fit are summarized in Table 10.1. There are 8 regions in the multivariate analysis and 10 regions in the cut-based analysis. m_{bb} is used in the top CR since BDT is not trained for top CR. Currently only yield is used in top CR 2 jet regions since statistics is limited. In future with more data, it will be possible to constrain the m_{bb} shape in the top CR.

10.3   Validation

The fit was validated by checking how much NP is pulled, how much the statistical uncertainties are reduced, and how much correlations were found among uncertainties. The expected and observed are compared for the validation. When a difference was found, the source was investigated and the variation was more de-correlated in order to avoid the constraint propagated in a wrong way.

The normalisation of V+HF and $t\bar{t}$ are shown in Chapter 11. They are sufficiently constrained in the 2 tag regions. The breakdown of the uncertainties on the signal strength are also shown in Chapter 11. In order to investigate the impact of each systematic variation, The fit is repeated setting a systematic variation to its fit value shifted to $\pm 1\sigma$ of its uncertainty. The differences of the signal strength are summed in quadrature in each category. The signal uncertainties, MC statistical uncertainty, background uncertainties and b-tag uncertainties were found to be dominant.

Chapter 11

Results

As mentioned in Chapter 6, it is important to cross check results of the multivariate analysis with the cut-based analysis. Furthermore it is also possible to validate both analyses, considering the diboson background as a signal. In this chapter, results of the multivariate analysis are shown in Section 11.1, results of the cut-based analysis are shown in Section 11.2, and the diboson validation is shown in Section 11.3.

11.1 Multivariate analysis

Postfit distributions in the top $e\mu$ CR are shown in Figure 11.1. Most of events are $t\bar{t}$ and thus uncertainties on $t\bar{t}$ modeling are constrained by data in this region. The floating normalization of $t\bar{t}$ is constrained:

- $t\bar{t}$ in 2 jet: 0.98 ± 0.11
- $t\bar{t}$ in ≥ 3 jet: 1.03 ± 0.07

Currently coarse binning is used, since data statistics is limited. Especially for 2 jets high p_{T}^V, only number of events is used. Postfit distributions in the SR are shown in Figure 11.2. The floating normalization of Z+jets is constrained by data in low BDT_{VH} regions that corresponds to m_{bb} sideband in the cut-based analysis:

- Z+HF in 2 jet: 1.28 ± 0.13
- Z+HF in ≥ 3 jet: 1.15 ± 0.10

An excess is found in high BDT_{VH} region. The significance and the signal strength are below.

- Observed significance: 3.6 standard deviations
- Expected significance: 1.9 standard deviations
- $\mu = 2.11 \ ^{+0.50}_{-0.48} \ \text{(stat.)} \ ^{+0.65}_{-0.47} \ \text{(syst.)}$

The breakdown of the uncertainties on the signal strength is summarized in Table 11.1. Impact of systematic uncertainties is getting greater than data statistical uncertainties. The most dominant sources are uncertainties on signal modeling, b-tag efficiency, Z+jets, MC stat, Jet and MET. Big impact NP are from signal acceptance uncertainties, b-tag efficiency, $t\bar{t}$ m_{bb} shape, Z+jets m_{bb} shape, Z+HF normalization. Number of events in the SR is shown in Table 11.2. 2 jet high p_{T}^V is the most sensitive region.
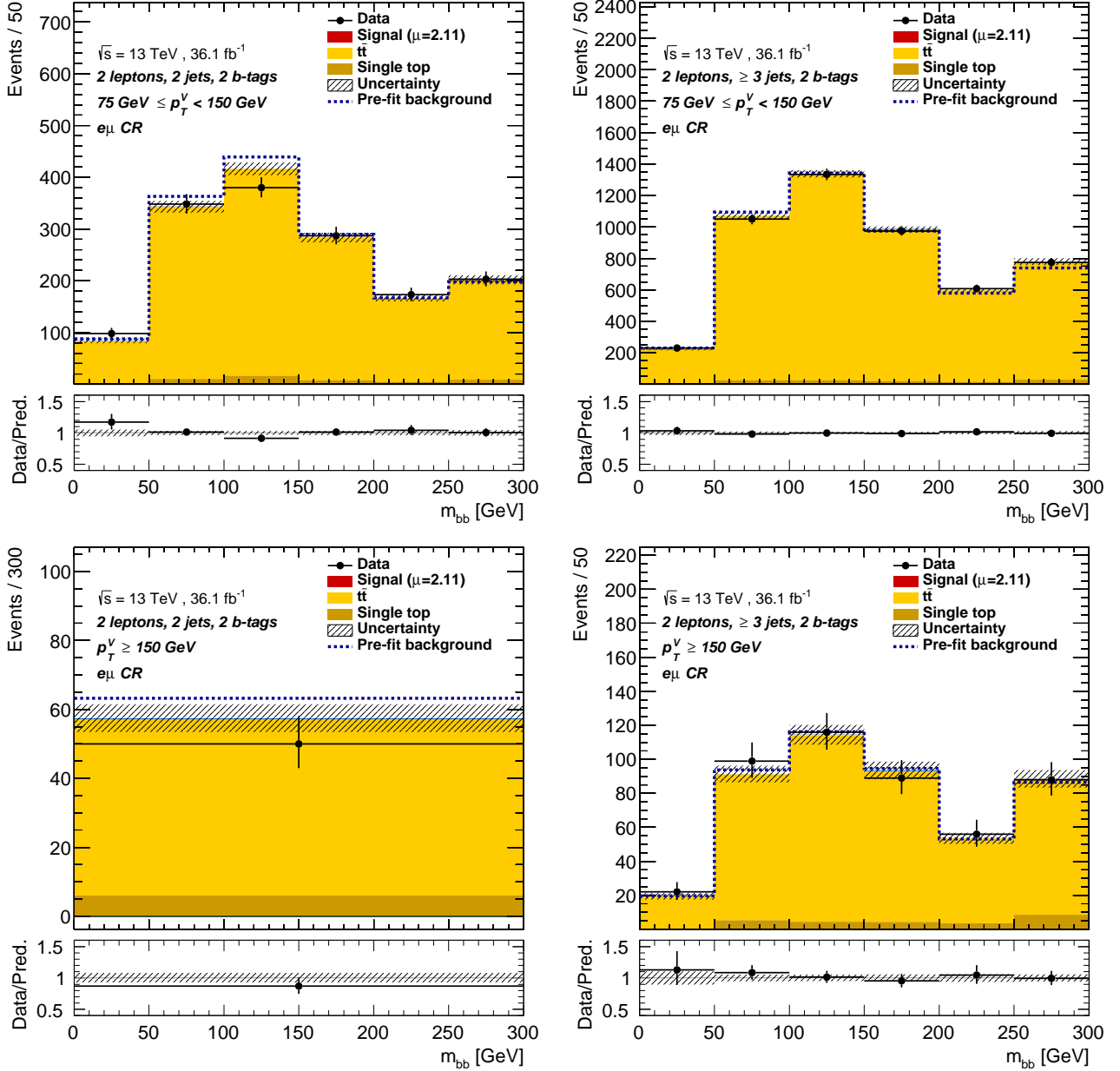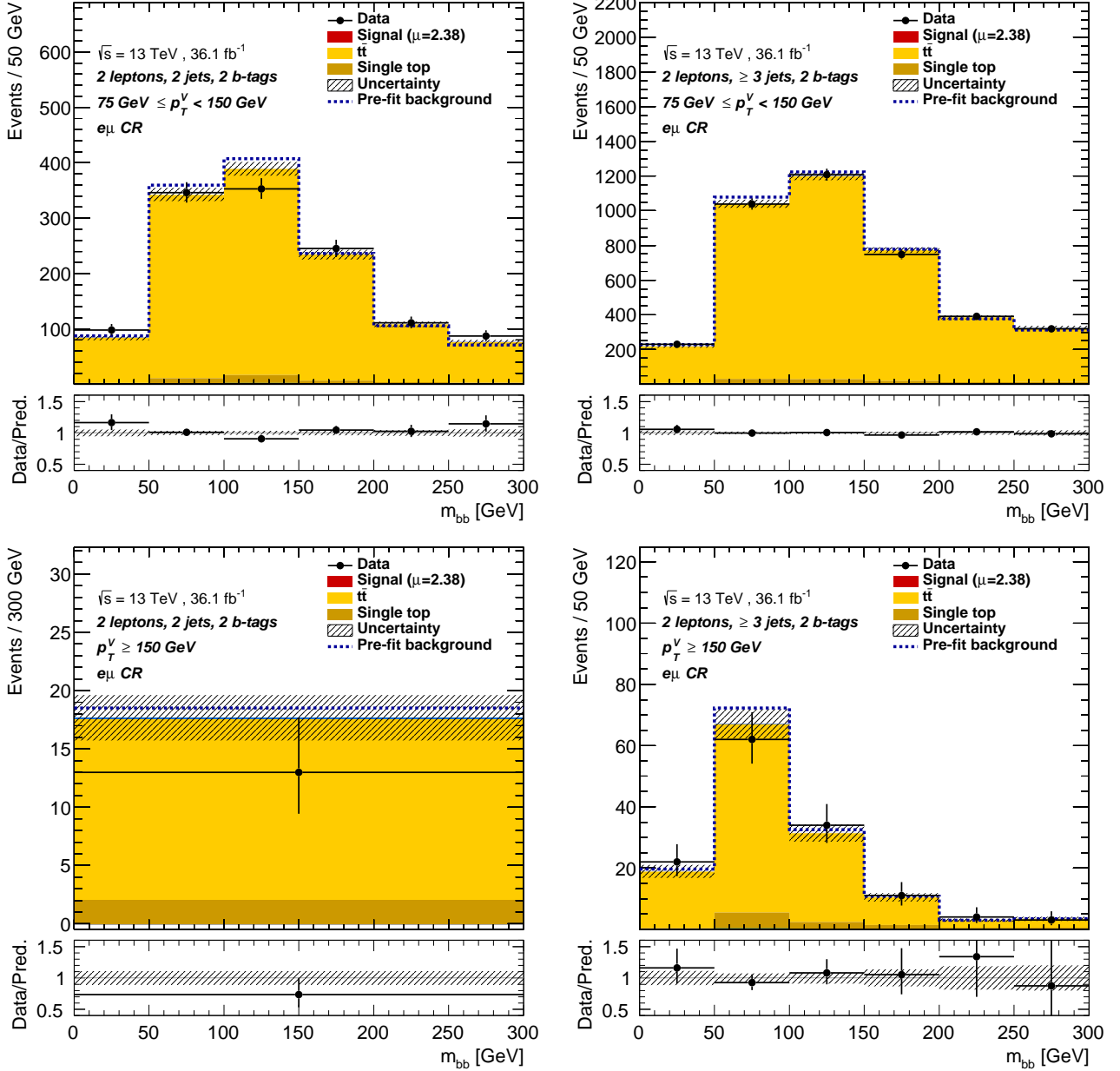
Figure 11.1 m_{bb} postfit distributions in the top $e\mu$ CR of the multivariate analysis. p_T^V 75–150 GeV (top) and p_T^V 150– GeV (bottom). 2 jets (left) and $\geq$ 3 jets (right). Filled histograms are postfit background and signal. Unfilled and unstacked histogram is signal, with a scale factor written in the legend. Dashed histograms are prefit background. Hatched bands are total uncertainties of postfit background and signal. Lower panels are ratio of data and postfit background and signal.
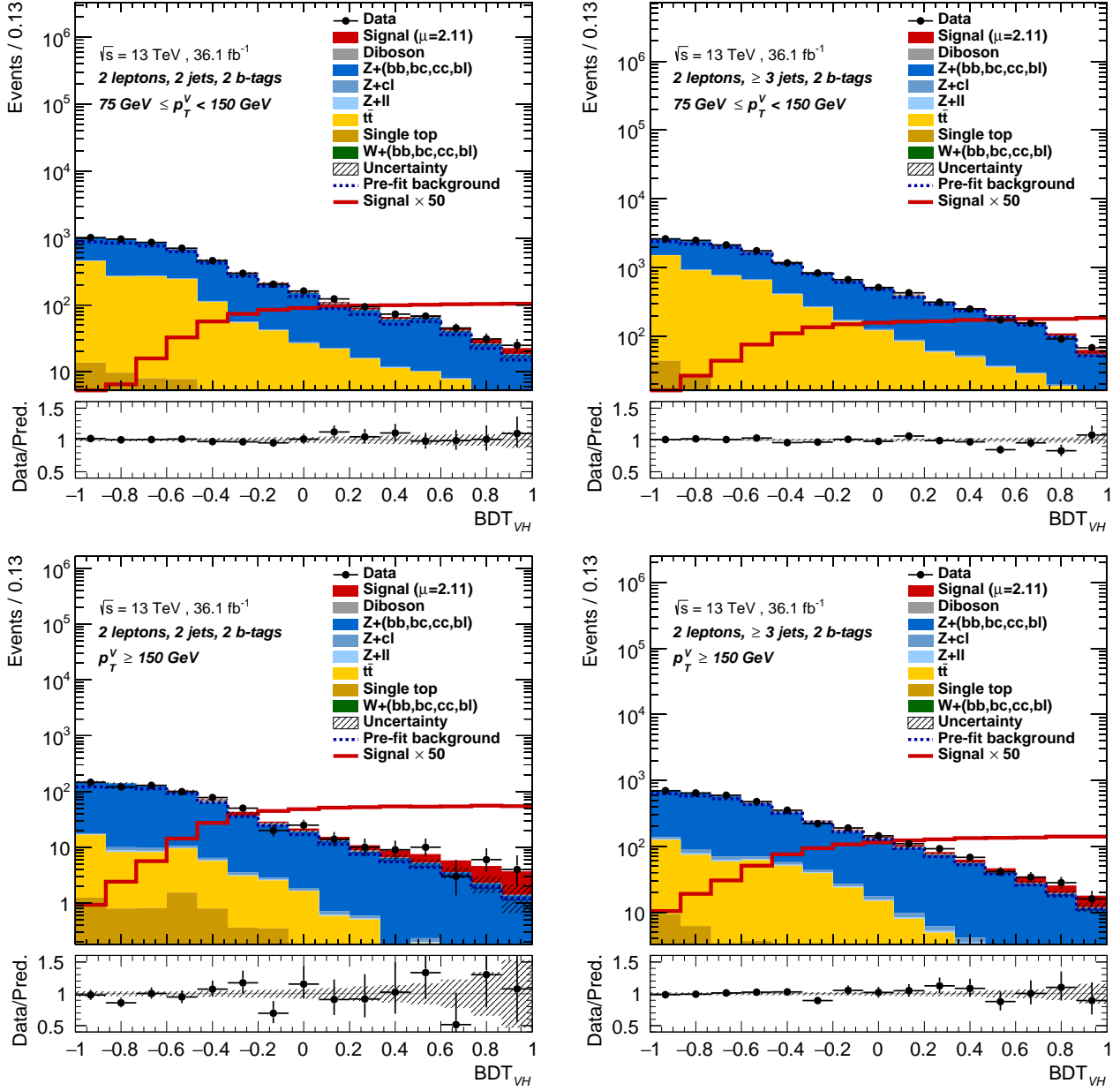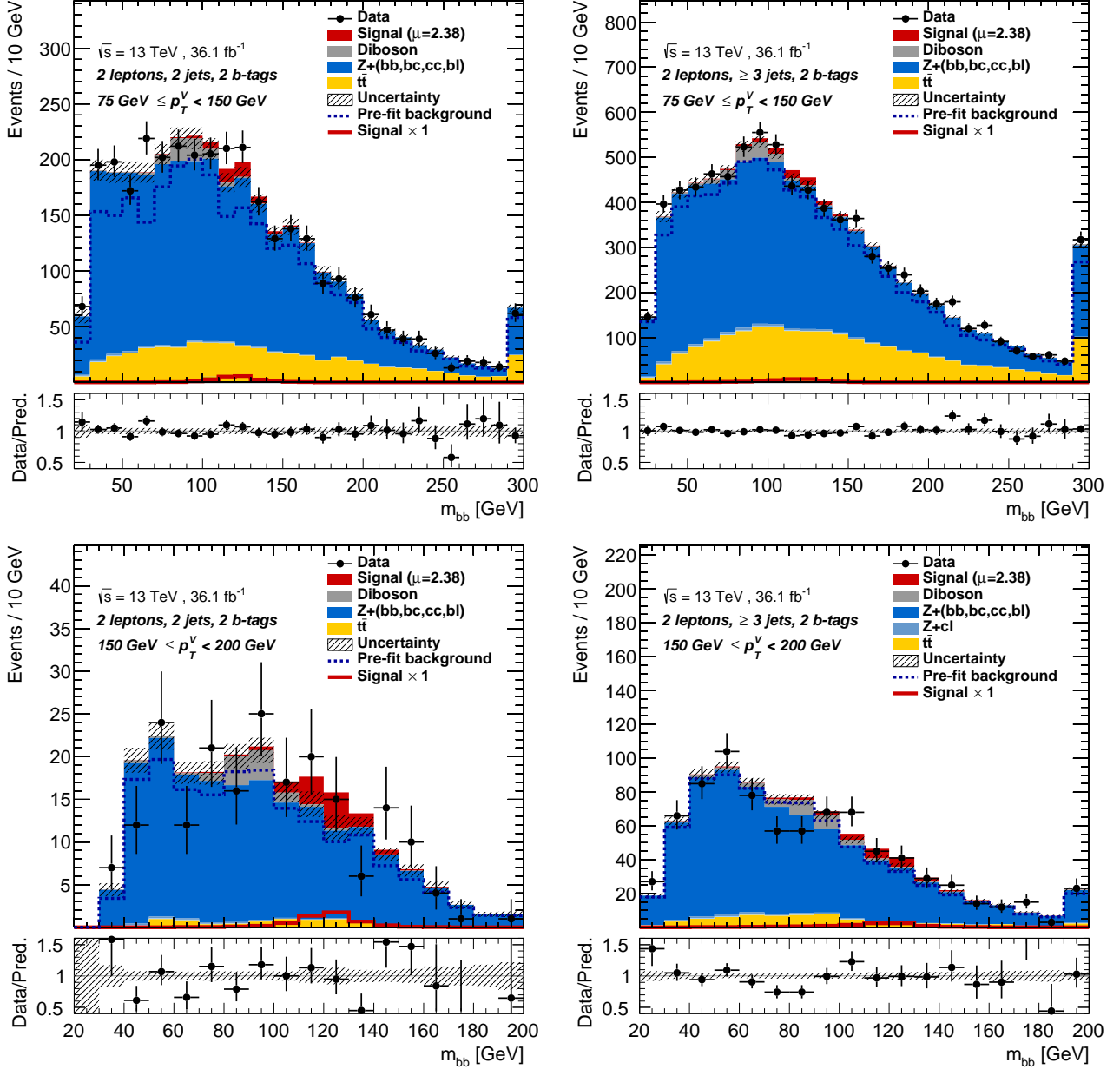
Figure 11.2 BDT_{VH} postfit distributions in the SR. p_T^V 75–150 GeV (top) and p_T^V 150– GeV (bottom). 2 jets (left) and $\geq$ 3 jets (right). Filled histograms are postfit background and signal. Unfilled and unstacked histogram is signal, with a scale factor written in the legend. Dashed histograms are prefit background. Hatched bands are total uncertainties of postfit background and signal. Lower panels are ratio of data and postfit background and signal.
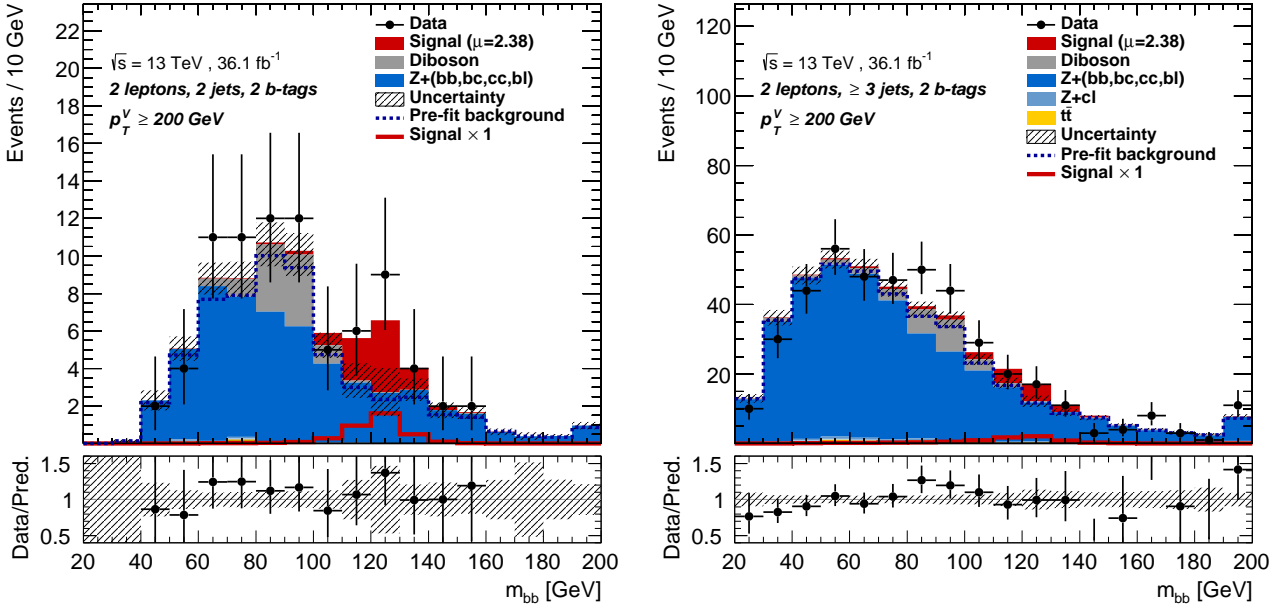
Table 11.1 Breakdown of uncertainties on signal strength of the multivariate analysis. Impact on signal strength is assessed by shifting a NP category to ± 1 standard deviation and fitting other parameters again. The impact in $\pm$ is the average of the absolute value. Quadrature sum of the impact can be different from the total because of correlations between uncertainties.

NP category	Impact on the signal strength
Total	± 0.74
Stat.	± 0.49
Syst.	± 0.56
b-tag	± 0.19
Jet and MET	± 0.15
Luminosity	± 0.07
Lepton	± 0.03
Signal	± 0.38
Z+jets	± 0.18
MC stat	± 0.17
$t\bar{t}$	± 0.13
Diboson	± 0.05
Single-top	± 0.03

Table 11.2 BDT$_{VH}$ postfit number of events in the SR. 2 jet high p_{T}^V is the most sensitive region.

p_{T}^V [GeV]	$75 - 150$		$150 -$	
Number of jets	2	≥ 3	2	≥ 3
$Z + ll$	10.04 ± 6.28	38.02 ± 21.38	2.09 ± 1.24	17.98 ± 10.69
$Z + cl$	26.65 ± 10.36	110.87 ± 42.15	5.73 ± 2.16	51.05 ± 19.45
Z+HF	3391.94 ± 85.13	8212.47 ± 154.87	631.08 ± 21.63	2999.07 ± 70.73
$W + ll$	0.01 ± 0.00	0.04 ± 0.00	0.00 ± 0.00	0.01 ± 0.00
$W + cl$	0.05 ± 0.00	0.18 ± 0.01	0.01 ± 0.00	0.05 ± 0.00
W+HF	2.63 ± 0.27	4.59 ± 0.15	0.25 ± 0.01	1.71 ± 0.06
Single-top	49.81 ± 18.86	129.22 ± 56.55	5.93 ± 2.30	28.43 ± 12.02
$t\bar{t}$	1478.15 ± 49.39	4911.92 ± 100.36	50.64 ± 3.12	437.07 ± 23.77
Diboson	74.95 ± 21.44	159.60 ± 35.88	24.95 ± 7.08	92.71 ± 21.28
Background	5034.23 ± 69.41	13566.90 ± 115.74	720.67 ± 20.11	3628.07 ± 58.44
Signal	44.88 ± 14.80	81.02 ± 25.65	23.61 ± 7.65	60.66 ± 18.98
Data	5113	13640	724	3708

11.2   Cut-based analysis

Postfit distributions in the top $e\mu$ CR are shown in Figure 11.3. Uncertainties on $t\bar{t}$ modeling are constrained in this region similarly to the multivariate analysis. The floating normalization of $t\bar{t}$ is constrained:

- $t\bar{t}$ in 2 jet: 0.97 ± 0.09
- $t\bar{t}$ in ≥ 3 jet: 0.95 ± 0.07

Postfit distributions in the SR are shown in Figure 11.4 and 11.5. The S/B ratio in the most sensitive bin is similar to the multivariate analysis. The floating normalization of Z+HF are constrained by data in m_{bb} sideband regions:

- Z+HF in 2 jet: 1.29 ± 0.12
- Z+HF in ≥ 3 jet: 1.08 ± 0.09

An excess is found at the mass of 125 GeV. The significance and the signal strength are below.

- Observed significance: 3.4 standard deviations
- Expected significance: 1.6 standard deviations
- $\mu = 2.38\ ^{+0.62}_{-0.59}$ (stat.) $^{+0.75}_{-0.53}$ (syst.)

The breakdown of the uncertainties on signal strength is summarized in Table 11.3. Impact of systematic uncertainties is getting greater than data statistical uncertainties. The most dominant sources are uncertainties on signal modeling, MC stat, b-tag efficiency, Z+jets modeling, $t\bar{t}$ modeling. Good agreement with the multivariate analysis within error was found. The expected significance is 20% lower than the multivariate analysis as expected. Number of events in the SR is shown in Table 11.4 and 11.5. 2 jet high p_{T}^{V} is the most sensitive region.

11.3   Diboson validation

The $ZZ \to \ell\ell bb$ yield is about 4 times larger than the $ZH \to \ell\ell bb$ in the SM. Therefore, it can be used for a good validation of the main analysis. A multivariate discriminant for the diboson signal (BDT_{VZ}) is used to extract the signal strength μ_{VZ}. It is trained for diboson signal with the same input variables in Chapter 8. WW is considered as a background since it has only small contribution. The normalization uncertainties on WZ and ZZ is removed. VH is considered as a background with cross-section uncertainty of 50%.

Postfit distributions in the top $e\mu$ CR are shown in Figure 11.6. The floating normalization of $t\bar{t}$ is constrained:

- $t\bar{t}$ in 2 jet: 0.97 ± 0.11
- $t\bar{t}$ in ≥ 3 jet: 1.01 ± 0.07

Postfit distributions in the SR are shown in Figure 11.7. The floating normalization of Z+jets is constrained by data in low BDT_{VH} regions that corresponds to m_{bb} sideband in the cut-based analysis:

- Z+HF in 2 jet: 1.26 ± 0.13
- Z+HF in ≥ 3 jet: 1.15 ± 0.11

An excess is found in high BDT_{VZ} region. The significance and the signal strength are:
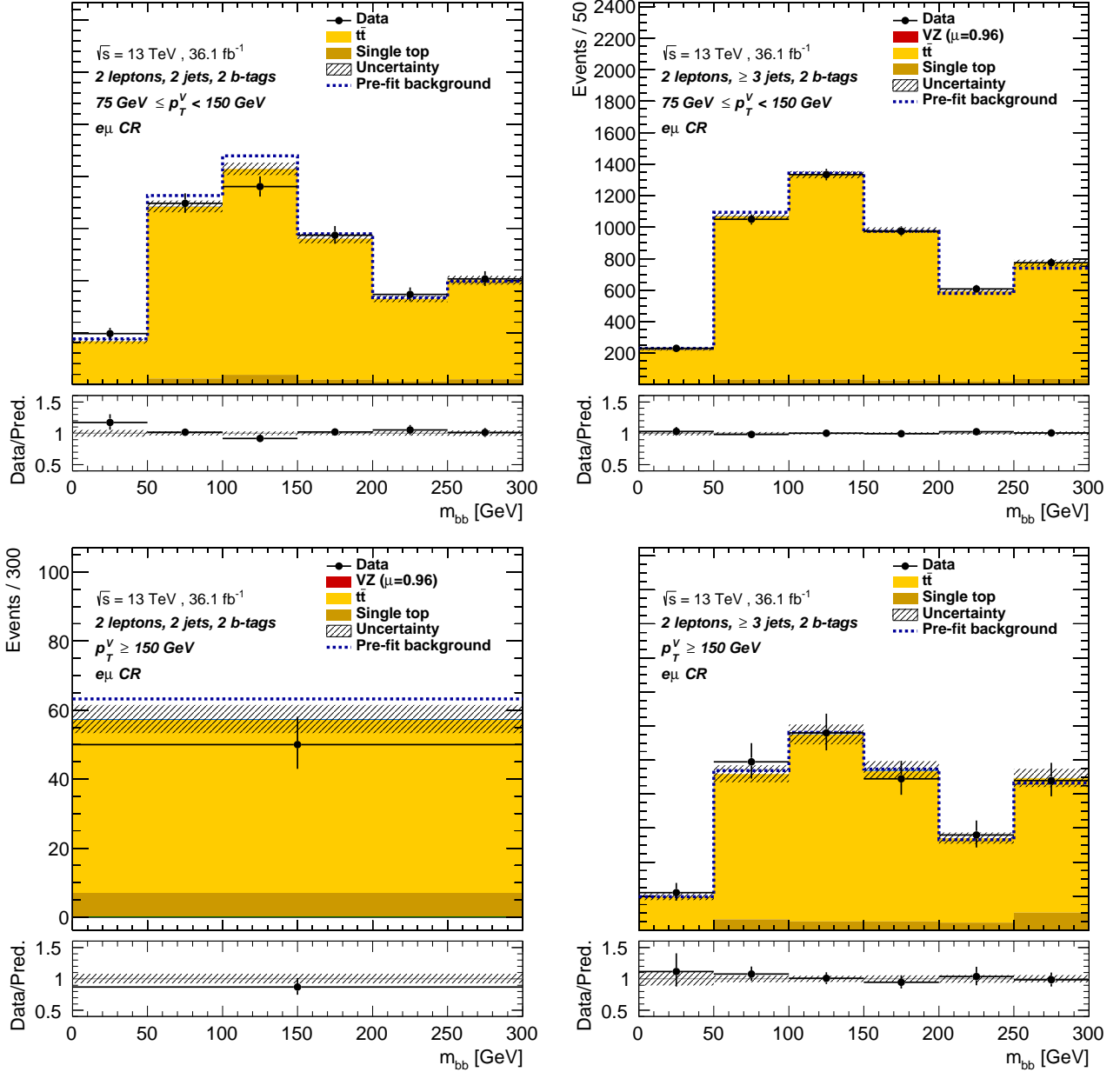
Figure 11.3 m_{bb} postfit distributions in the top $e\mu$ CR of the cut-based analysis. p_T^V 75–150 GeV (top) and p_T^V 150– GeV (bottom). 2 jets (left) and $\geq$ 3 jets (right). Filled histograms are postfit background and signal. Unfilled and unstacked histogram is signal, with a scale factor written in the legend. Dashed histograms are prefit background. Hatched bands are total uncertainties of postfit background and signal. Lower panels are ratio of data and postfit background and signal.

Figure 11.4 m_{bb} postfit distributions in the SR. p_T^V 75–150 GeV (top) and p_T^V 150–200 GeV (bottom). 2 jets (left) and $\geq$ 3 jets (right). Filled histograms are postfit background and signal. Unfilled and unstacked histogram is signal, with a scale factor written in the legend. Dashed histograms are prefit background. Hatched bands are total uncertainties of postfit background and signal. Lower panels are ratio of data and postfit background and signal.

Figure 11.5 m_{bb} postfit distributions in the SR p_T^V 200– GeV. 2 jets (left) and $\geq$ 3 jets (right). Filled histograms are postfit background and signal. Unfilled and unstacked histogram is signal, with a scale factor written in the legend. Dashed histograms are prefit background. Hatched bands are total uncertainties of postfit background and signal. Lower panels are ratio of data and postfit background and signal.

Table 11.3   Breakdown of uncertainties on signal strength of the cut-based analysis. Impact on signal strength is assessed by shifting a NP category to $\pm$ 1 standard deviation and fitting other parameters again. The impact in $\pm$ is the average of the absolute value. Quadrature sum of the impact can be different from the total because of correlations between uncertainties.

NP category	Impact on the signal strength
Total	$\pm$ 0.88
Stat.	$\pm$ 0.60
Syst.	$\pm$ 0.64
b-tag	$\pm$ 0.12
Luminosity	$\pm$ 0.08
Jet and MET	$\pm$ 0.06
Lepton	$\pm$ 0.04
Signal	$\pm$ 0.46
MC stat	$\pm$ 0.25
Z+jets	$\pm$ 0.12
$t\bar{t}$	$\pm$ 0.11
Diboson	$\pm$ 0.08
Single-top	$\pm$ 0.00

Table 11.4 m_{bb} postfit number of events in the SR. 2 jet high p_T^V is the most sensitive region.

p_T^V [GeV]	75 − 150		150 − 200	
Number of jets	2	≥ 3	2	≥ 3
$Z + ll$	6.76 ± 3.99	25.24 ± 0.82	0.58 ± 0.33	3.00 ± 1.80
$Z + cl$	19.20 ± 7.37	79.60 ± 30.78	1.62 ± 0.60	9.71 ± 3.75
Z+HF	2514.81 ± 65.46	5771.82 ± 110.31	182.21 ± 8.03	698.00 ± 20.14
$W + ll$	0.00 ± 0.00	0.02 ± 0.00	0.00 ± 0.00	0.00 ± 0.00
$W + cl$	0.03 ± 0.00	0.11 ± 0.00	0.00 ± 0.00	0.01 ± 0.00
W+HF	1.18 ± 0.05	2.56 ± 0.08	0.00 ± 0.00	0.81 ± 0.16
Single-top	19.43 ± 6.87	48.04 ± 18.50	0.80 ± 0.05	2.09 ± 0.86
$t\bar{t}$	568.67 ± 23.73	1935.79 ± 52.68	6.75 ± 0.75	64.13 ± 6.48
Diboson	69.30 ± 16.41	158.94 ± 29.02	10.53 ± 2.57	34.43 ± 6.96
Background	3199.37 ± 57.99	8022.12 ± 91.29	202.51 ± 7.85	812.17 ± 18.84
Signal	46.85 ± 15.65	84.02 ± 26.91	11.97 ± 3.96	25.04 ± 8.00
Data	3250	8123	205	817

Table 11.5 m_{bb} postfit number of events in the SR (2). 2 jet high p_T^V is the most sensitive region.

p_T^V [GeV]	200 −	
Number of jets	2	≥ 3
$Z + ll$	0.26 ± 0.14	1.89 ± 1.11
$Z + cl$	0.60 ± 0.23	5.04 ± 1.91
Z+HF	54.44 ± 3.71	368.57 ± 16.41
$W + l$	0.00 ± 0.00	0.00 ± 0.00
$W + cl$	0.00 ± 0.00	0.00 ± 0.00
W+HF	0.10 ± 0.01	0.26 ± 0.15
Single-top	0.34 ± 0.03	1.18 ± 0.50
$t\bar{t}$	0.00 ± 0.00	5.70 ± 1.03
Diboson	9.98 ± 2.40	30.12 ± 6.38
Background	65.72 ± 4.01	412.76 ± 15.88
Signal	8.63 ± 2.87	18.22 ± 5.78
Data	80	436

- Observed significance: 3.5 standard deviations
- Expected significance: 3.5 standard deviations
- $\mu = 0.96 \, ^{+0.19}_{-0.19}$ (stat.) $^{+0.26}_{-0.22}$ (syst.)

The significance is higher than the the main analysis, and the error on the signal strength is smaller than the main analysis. This is consistent with the fact that the ZZ yield is about 4 times larger than the ZH in the SM. Furthermore, the signal strength is consistent with the SM within error. Thus, the analysis is validated.

Figure 11.6 m_{bb} postfit distributions in the top $e\mu$ CR of the diboson validation. p_T^V 75–150 GeV (top) and p_T^V 150– GeV (bottom). 2 jets (left) and $\geq$ 3 jets (right). Filled histograms are postfit background and signal. Unfilled and unstacked histogram is signal, with a scale factor written in the legend. Dashed histograms are prefit background. Hatched bands are total uncertainties of postfit background and signal. Lower panels are ratio of data and postfit background and signal.
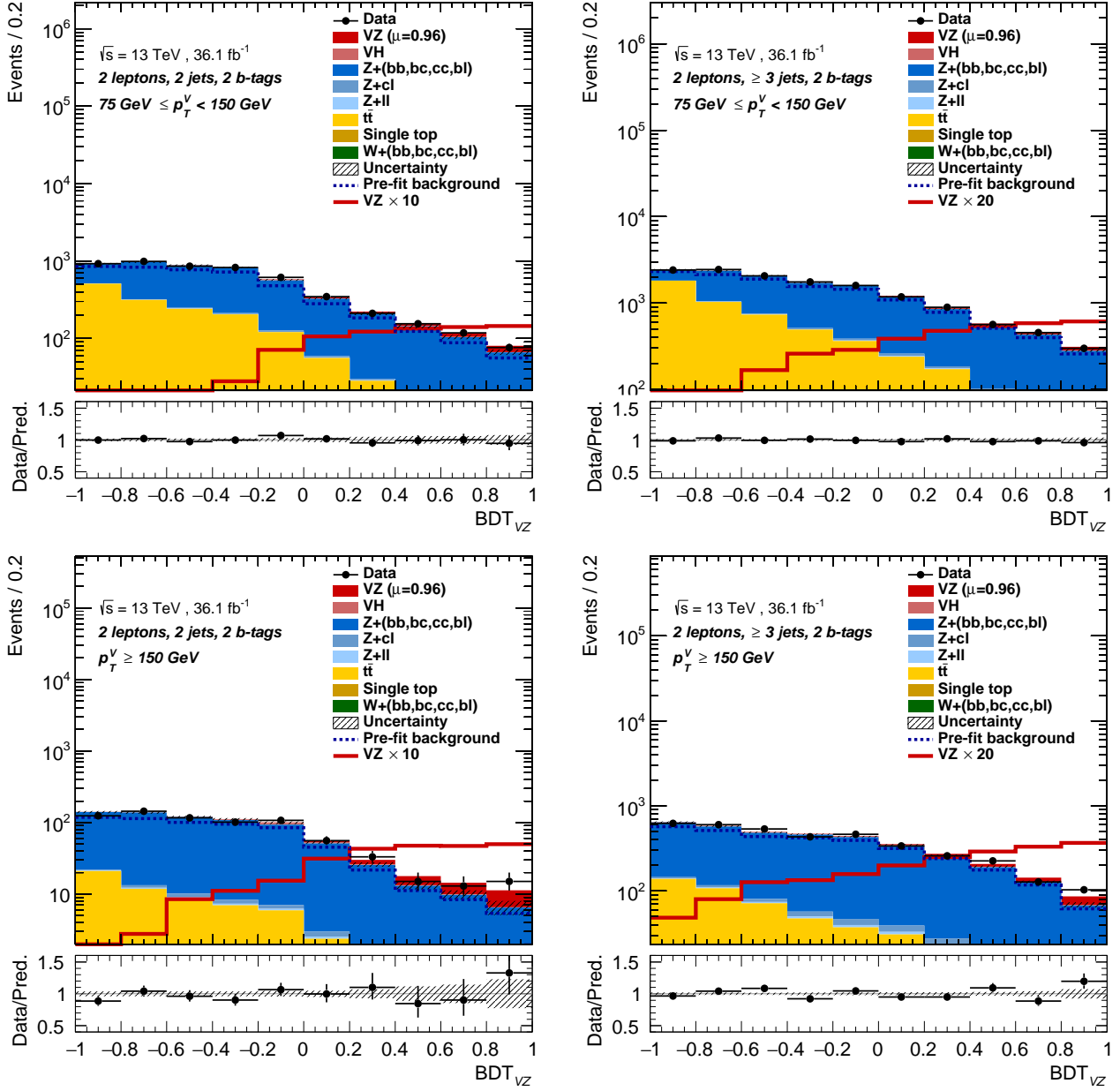
Figure 11.7 BDT$_{VZ}$ postfit distributions in the SR. p_{T}^V 75–150 GeV (top) and p_{T}^V 150– GeV (bottom). 2 jets (left) and $\geq$ 3 jets (right). Filled histograms are postfit background and signal. Unfilled and unstacked histogram is signal, with a scale factor written in the legend. Dashed histograms are prefit background. Hatched bands are total uncertainties of postfit background and signal. Lower panels are ratio of data and postfit background and signal.

Chapter 12

Combined Results

The results of the 2-lepton analysis in Run2 was presented in Chapter 11. Since the error on the signal strength is still large, it is important to look at the 0,1,2-lepton combined results. ATLAS reported Run1 combined results in 2014 [10], and Run1 + Run2 combined results in 2017 [90]. In this chapter, Run1 combined results, Run2 combined results, and Run1 + Run2 combined results are reviewed in Section 12.1, Section 12.2, and 12.3 respectively.

12.1 Run1 combined results

ATLAS reported Run1 combined results in 2014 [10]. The integrated luminosity was approximately 5 and 20 fb^{-1} for the center of mass energy of 7 and 8 TeV. The significance and the signal strength were:

- Observed significance: 1.4 standard deviations
- Expected significance: 2.6 standard deviations
- $\mu = 0.51 \, ^{+0.31}_{-0.30} \, \text{(stat.)} \, ^{+0.25}_{-0.22} \, \text{(syst.)}$

The signal strength of the Run1 combined results is shown in figure 12.1. There are results of 3 Parameter Of Interest (POI) fit and 2 POI fit. 3 POI fit de-correlates the signal strength of 0,1,2-lepton signal. 2 POI fit de-correlates the signal strength of 0,2-lepton signal (ZH) and 1-lepton signal (WH). In Run1 with limited data statistics, 0-lepton data was lower than background expectation at the mass of 125 GeV. Therefore, the signal strength was lower than zero.

12.2 Run2 combined results

ATLAS reported Run2 combined results in 2017 [90]. The integrated luminosity was 36.1 fb^{-1} for the center of mass energy of 13 TeV. The significance and the signal strength were:

- Observed significance: 3.5 standard deviations
- Expected significance: 3.0 standard deviations
- $\mu = 1.20 \, ^{+0.24}_{-0.23} \, \text{(stat.)} \, ^{+0.34}_{-0.28} \, \text{(syst.)}$

The signal strength of Run2 combined results is shown in figure 12.2. The results are consistent with the SM.

The 2-lepton results in the 3 POI fit are:

- Observed significance: 3.6 standard deviations
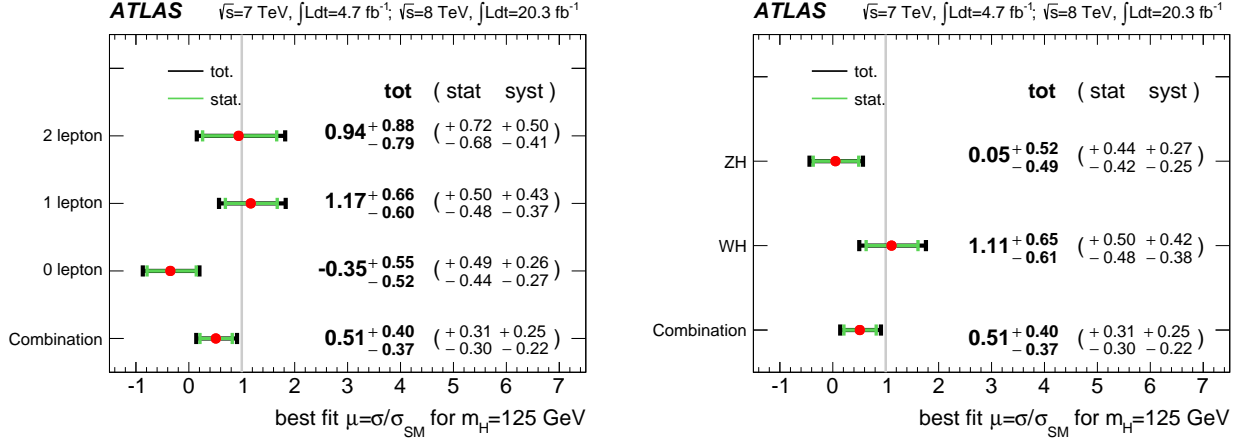
Figure 12.1   The signal strength of Run1 combined results [10]. 3 POI fit (left) and 2 POI fit (right).
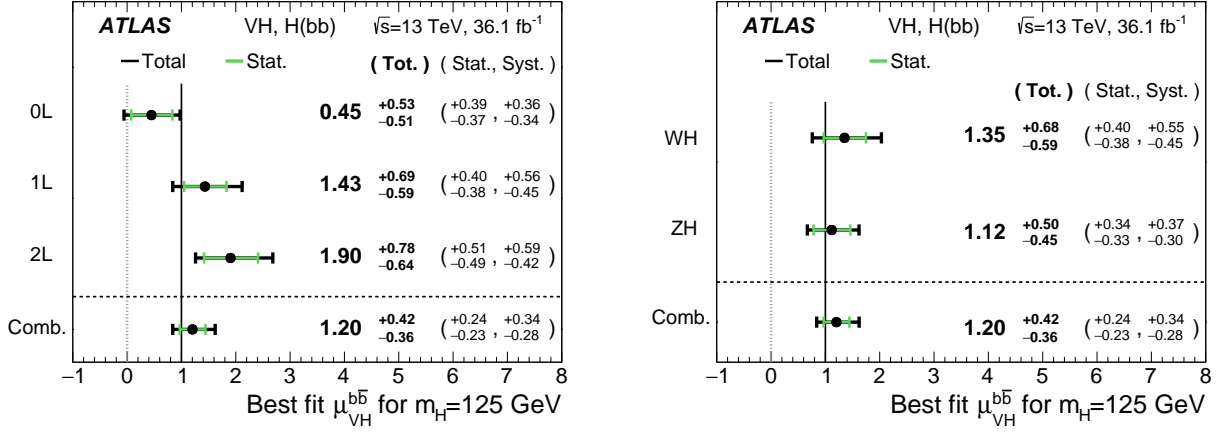
Figure 12.2   The signal strength of Run2 combined results [90]. 3 POI fit (left) and 2 POI fit (right).

- Expected significance: 1.9 standard deviations
- $\mu = 1.90\ ^{+0.51}_{-0.49}$ (stat.) $^{+0.59}_{-0.42}$ (syst.)

These are consistent with the results in Section 11.1. The signal strength is about 10% lower than Section 11.1. This can be explained by difference in the Z+HF normalization. The floating normalization of Z+HF is also constrained by data in the 0-lepton channel in the combined fit. Thus, Z+HF is normalized to higher value than Section 11.1:

- Z+HF in 2 jet: 1.30 ± 0.10
- Z+HF in ≥ 3 jet: 1.22 ± 0.09

The floating normalization of $t\bar{t}$ is de-correlated for 2 lepton channel in the combined fit. Therefore, $t\bar{t}$ is normalized similarly to Section 11.1:

- $t\bar{t}$ in 2 lepton 2 jet: 0.97 ± 0.09
- $t\bar{t}$ in 2 lepton ≥ 3 jet: 1.04 ± 0.06
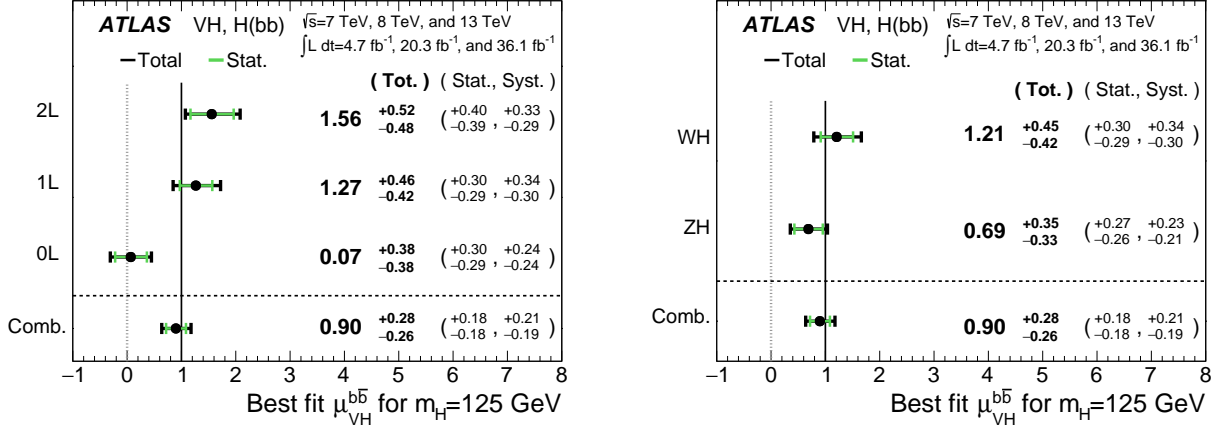
Figure 12.3   The signal strength of Run1 + Run2 combined results [90]. 3 POI fit (left) and 2 POI fit (right).

12.3   Run1 + Run2 combined results

ATLAS reported Run1 + Run2 combined results in 2017 [90]. The integrated luminosity was 4.7, 20.3, 36.1 fb^{-1} for center of mass energy of 7, 8, 13 TeV. The systematic uncertainty on b-jet energy scale was correlated between Run1 and Run2, after testing different correlation schemes for systematic uncertainties on jet energy scale. Systematic uncertainties on signal cross-section, branching ratio and the NLO EW correction were also correlated between Run1 and Run2. The other correlation was also tested and found to be negligible. The significance and the signal strength were:

- Observed significance: 3.6 standard deviations
- Expected significance: 4.0 standard deviations
- $\mu = 0.90 {}^{+0.18}_{-0.18}$ (stat.) ${}^{+0.21}_{-0.19}$ (syst.)

The signal strength of Run1 + Run2 combined results is shown in figure 12.3. The results are consistent with the SM.

Chapter 13

Conclusion

Theis thesis presented a piece of evidence for the Higgs boson decaying to a pair of b quarks. The LHC Run2 proton-proton collisions data collected with the ATLAS detector is used. The center-of-mass energy is 13 TeV, and the integrated luminosity is 36.1 fb^{-1}. ATLAS level-1 endcap muon trigger (TGC) achieved about 90% trigger efficiency. A b-jet energy correction (KF) improved the Higgs mass resolution about 40% at maximum. An excess over background is found in the Vector boson associated production (VH) 2-lepton channel. The observed (expected) significance is 3.6 (1.9) standard deviations. The signal strength compared to the Standard Model (SM) is 2.11 $^{+0.50}_{-0.48}$ (stat.) $^{+0.65}_{-0.47}$ (syst.). In ATLAS VH 0, 1, 2-lepton, Run1 + Run2 combined results [90], the observed (expected) significance is 3.6 (4.0) standard deviations. The signal strength is 0.90 $^{+0.18}_{-0.18}$ (stat.) $^{+0.21}_{-0.19}$ (syst.). The results are consistent with the SM.

In order to reach expected significance of 5 standard deviations, ATLAS will have to reduce statistical and systematic uncertainties. The integrated luminosity will reach 100 fb^{-1} by the end of Run2 in 2018. The luminosity extrapolation in Run2 is shown in Figure 13.1. If ATLAS achieves systematic uncertainty of 0.12 on the signal strength, it will reach expected significance of 5 standard deviations around 80 fb^{-1}. In 2-lepton analysis, there are several ideas to improve the sensitivity. For example, the KF can use the track-based soft term to balance the system more properly. In this case, the assumption of the signal topology can be removed and more model independent correction can be established. Furthermore, data distribution in the top $e\mu$ Control Region can be used to estimate $t\bar{t}$ in the Signal Region. In this case, systematic uncertainties on $t\bar{t}$ simulation can be removed.
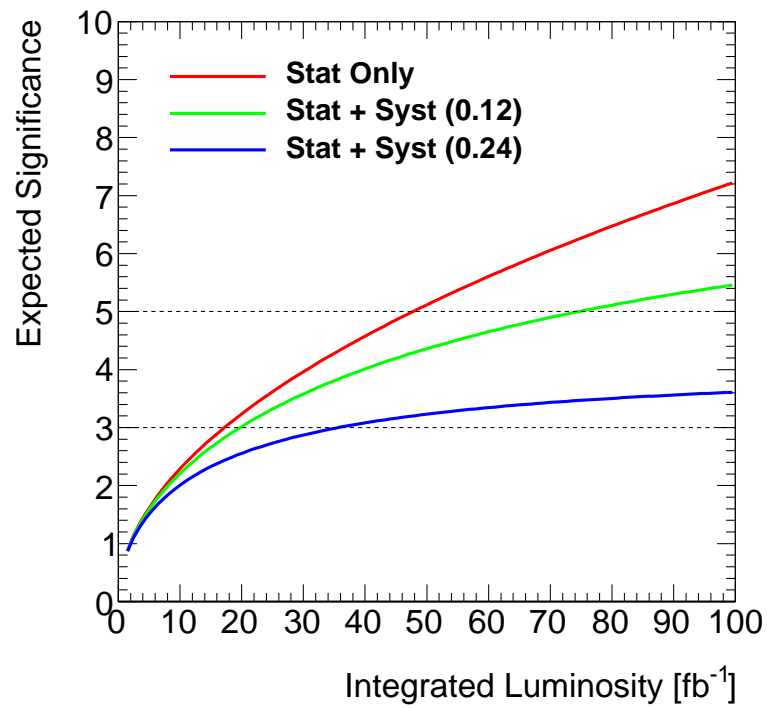
Figure 13.1   Luminosity extrapolation. Red line considers only statistical uncertainty. Green (blue) line considers statistical uncertainty and systematic uncertainty of 0.12 (0.24) on the signal strength.

Appendix

In this appendix, the estimation of multi-jet background is summarized in Appendix A, the KF variables, the BDT variables and an event display are shown in Appendix B, C and D respectively.

A   Multi-jet background

Multi-jet background is strongly suppressed by requiring 2 leptons and the Z boson mass. However, the cross-section of multi-jet is orders of magnitude larger than the signal and backgrounds, as shown in Figure 2.1, and jets can be still rarely identified as leptons in the SR. Therefore, it is important to estimate the amount of multi-jet in the SR. In 2-lepton analysis, multi-jet can be estimated at first in a region called Same Sign (SS) region, where 2 leptons are required to have the same charge. Then, multi-jet in the SR can be estimated assuming that the number of events in SS and Opposite Sign (OS) are the same.

The $m_{\ell\ell}$ distributions in the SS is shown in Figure A.1. Multi-jet is modeled by a exponential function fit to data after subtracting Z+jets and top. For electron channel, Z+jets and top are normalized to nominal cross-sections. For muon channel, Z+jets and top are scaled by 0.6 since there was a difference in data and simulation. The number of events around the Z peak was about 10 times smaller in muon channel. Signal efficiency loss by requiring OS was about 0.26% for muon channel and 2.03% for electron channel. Therefore, OS is only required for the muon channel. The charge identification of muons will improve in future.

The $m_{\ell\ell}$ distributions in the SR is shown in Figure A.2. Multi-jet was found to be less than 1% of total background. This corresponds to 10% level of signal in $m_{bb} = 100$–140 GeV. However, the m_{bb} shape of multi-jet was found to be close to Z+jets and $t\bar{t}$. Therefore, multi-jet can be absorbed by the floating normalization of Z+jets and $t\bar{t}$ in the statistical analysis. Furthermore, multi-jet in top CR was also found to be less than 1% of total background. Therefore, multi-jet is not included in the statistical analysis.

B   KF variables

The KF variables are shown in Figure B.3–B.10. Good agreement between data and simulation was found. Therefore, it is possible to use these variables for the KF.

C   BDT variables

The BDT variables are shown in Figure C.11–C.16. Good agreement between data and simulation was found. Therefore, it is possible to use these variables for the BDT.
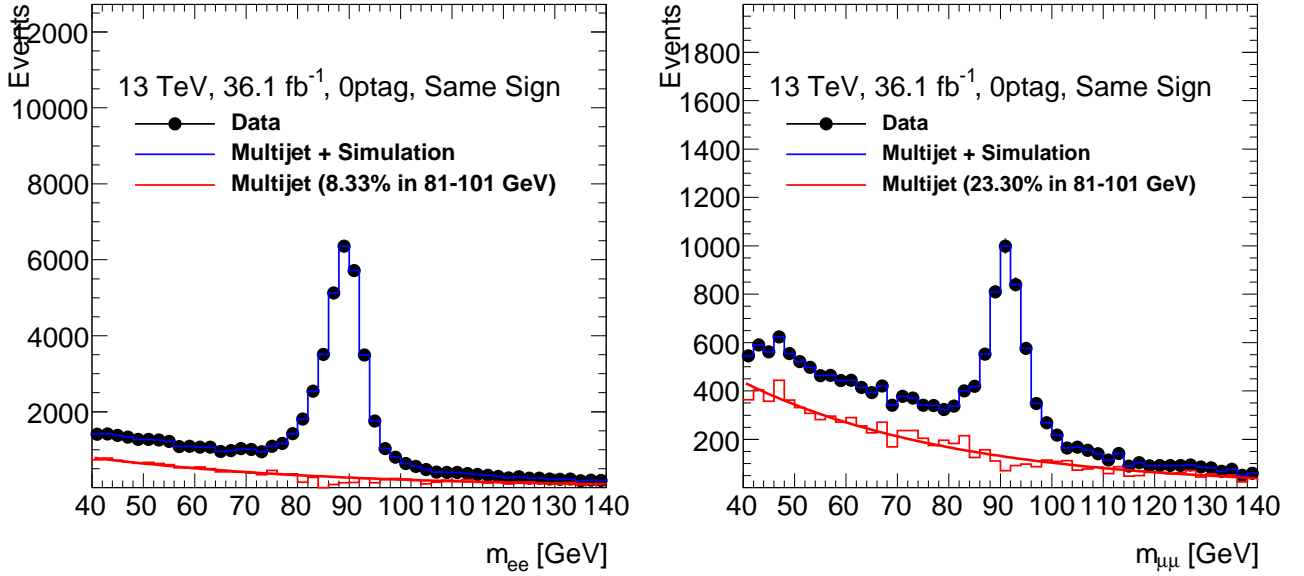
Figure A.1 $m_{\ell\ell}$ distribution in SS. Electron channel (left) and muon channel (right).
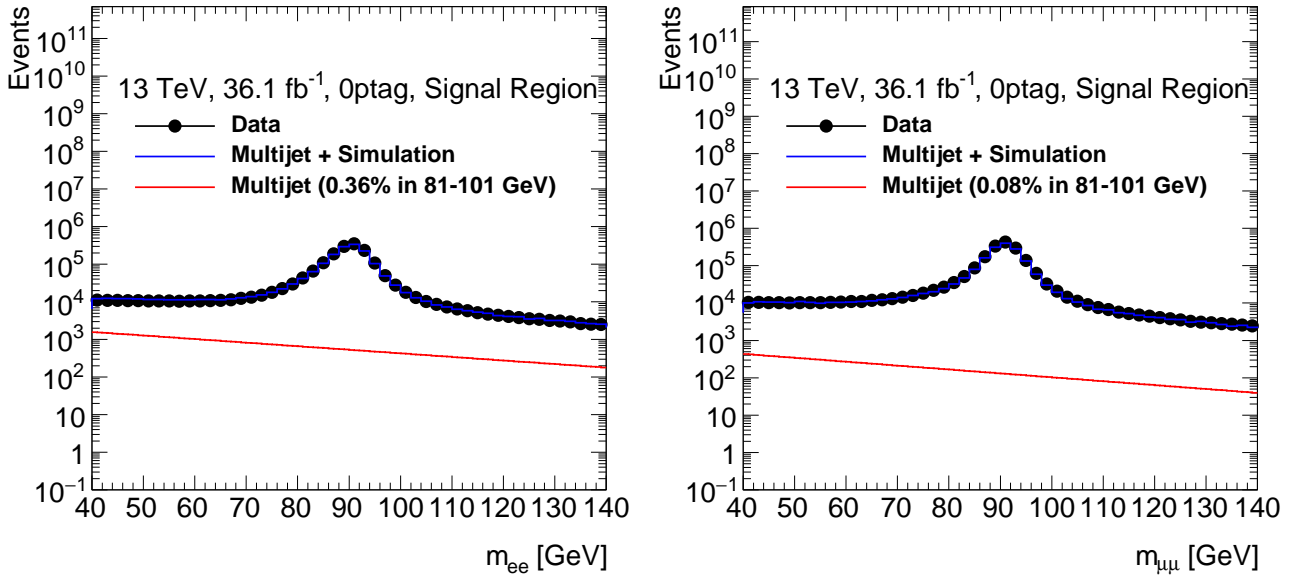
Figure A.2 $m_{\ell\ell}$ distribution in SR. Electron channel (left) and muon channel (right).

D   Event display

An event display of a 2 muon, 2 tag, 2 jet event in the high BDT_{VH} region is shown in Figure D.17. Auxiliary material of the ATLAS combined results can be found in URL of [90]. There are two muons from Z boson candidate with a mass of 89 GeV and p_T^V of 204 GeV. Another muon is from a b-jet with $\Delta R < 0.4$. The one from a b-jet is used in the muon-in-jet correction. There are 2 b-jet from the Higgs boson candidate with a mass of 123 GeV. Such events are in the high BDT_{VH} region.
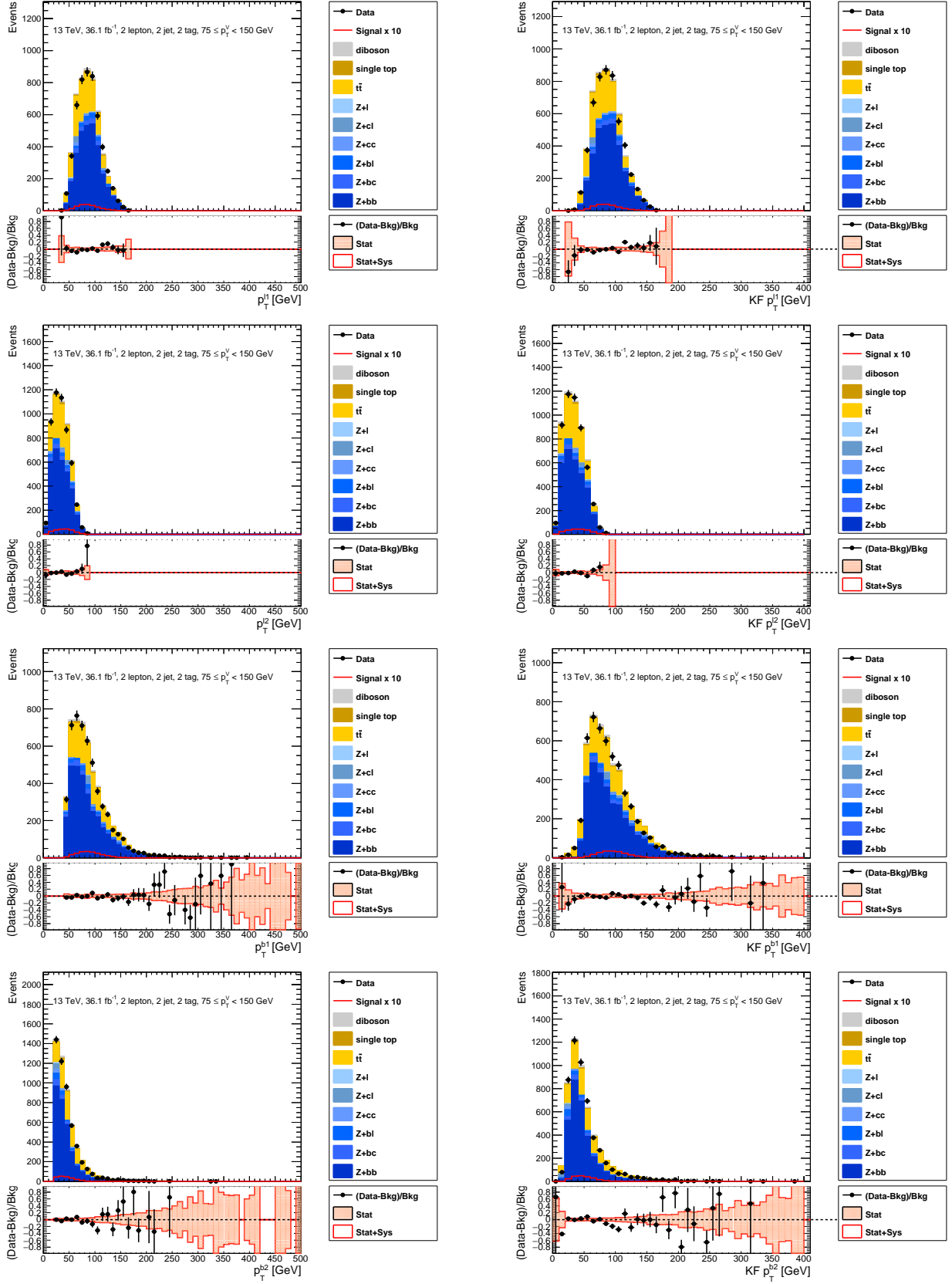
Figure B.3   KF variables in 2 jet p_T^V 75–150 GeV (1). before KL (left) and after KF (right). From top to bottom p_T of leading lepton, sub leading lepton, leading b-jet, sub leading lepton b-jet. Signal is scaled by 10. Z+HF and $t\bar{t}$ are scaled by the same factors in section 11.1.
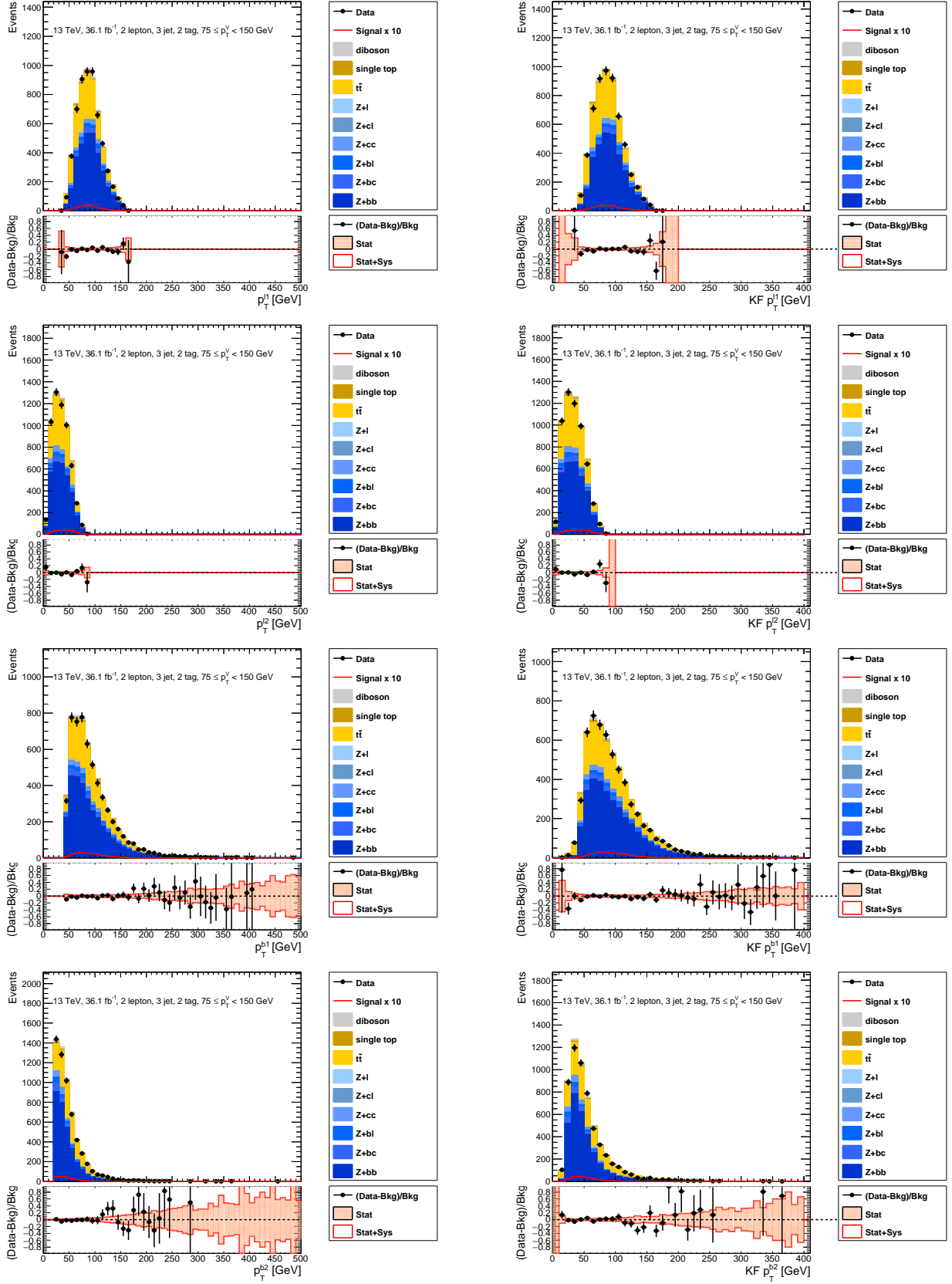
Figure B.4 KF variables in 3 jet p_T^V 75–150 GeV (1). before KL (left) and after KF (right). From top to bottom p_T of leading lepton, sub leading lepton, leading b-jet, sub leading lepton b-jet. Signal is scaled by 10. Z+HF and $t\bar{t}$ are scaled by the same factors in section 11.1.
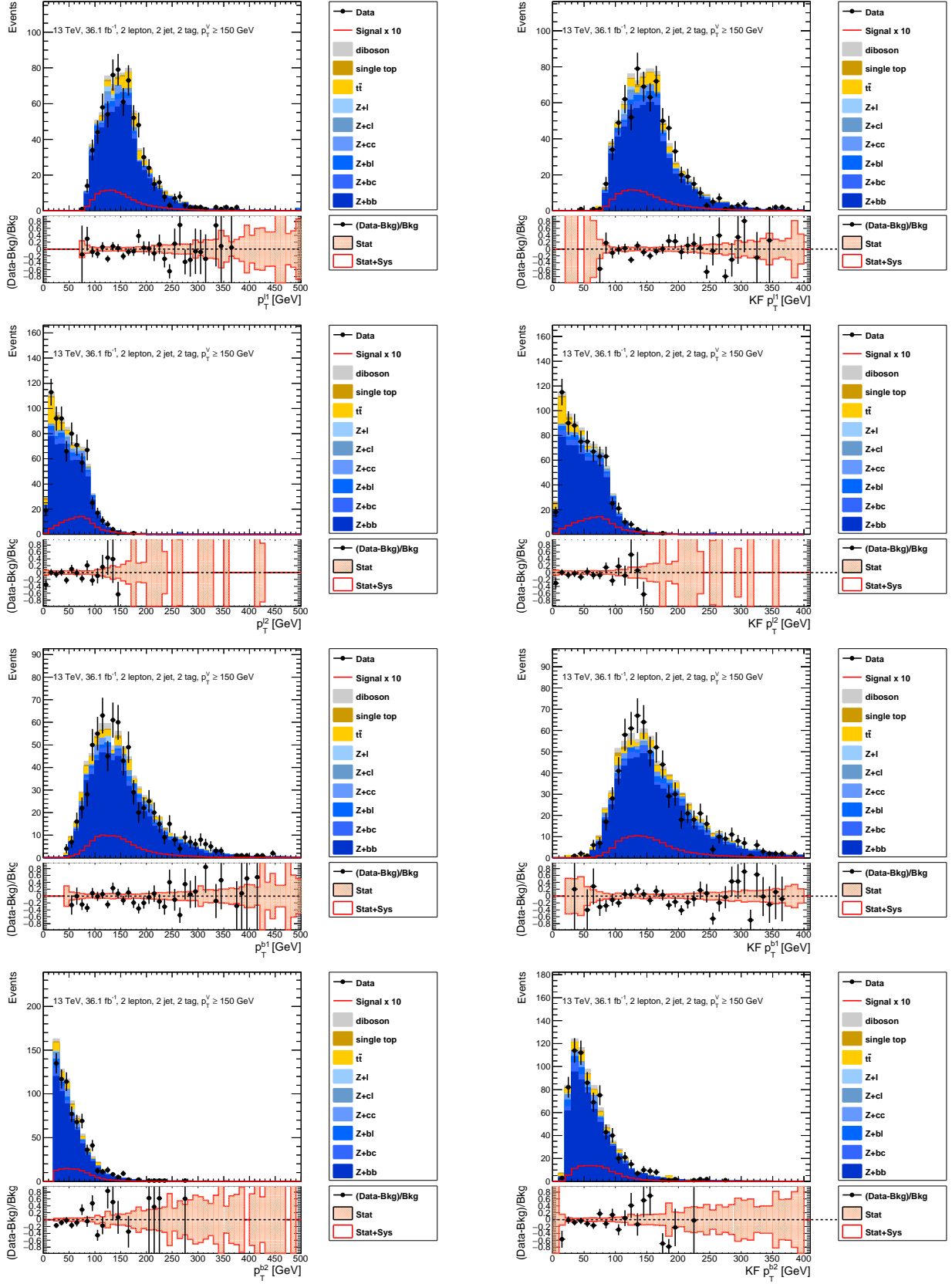
Figure B.5   KF variables in 2 jet p_T^V 150– GeV (1). before KL (left) and after KF (right). From top to bottom p_T of leading lepton, sub leading lepton, leading b-jet, sub leading lepton b-jet. Signal is scaled by 10. Z+HF and $t\bar{t}$ are scaled by the same factors in section 11.1.
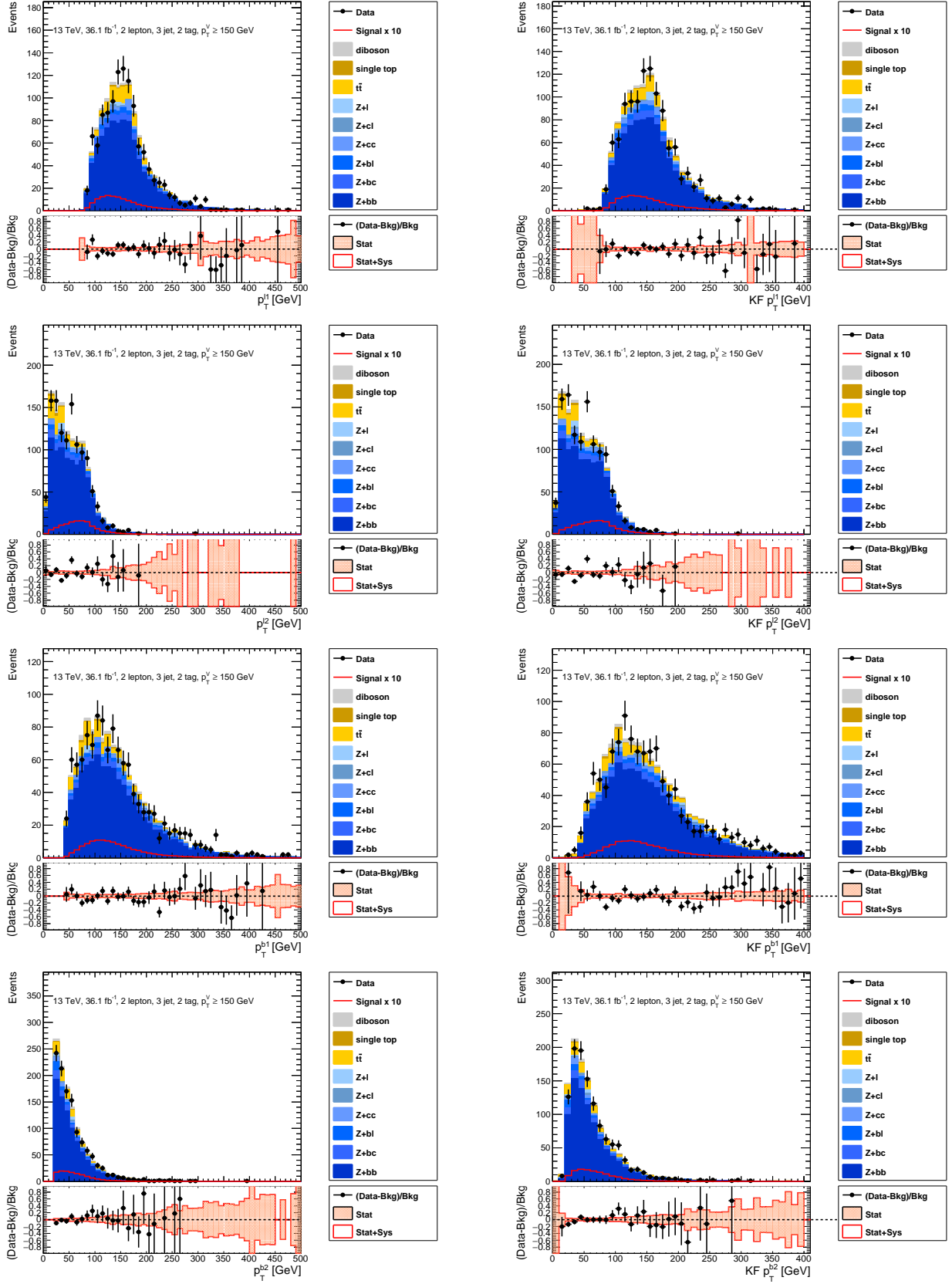
Figure B.6   KF variables in 3 jet p_T^V 150– GeV (1). before KL (left) and after KF (right). From top to bottom p_T of leading lepton, sub leading lepton, leading b-jet, sub leading lepton b-jet. Signal is scaled by 10. Z+HF and $t\bar{t}$ are scaled by the same factors in section 11.1.
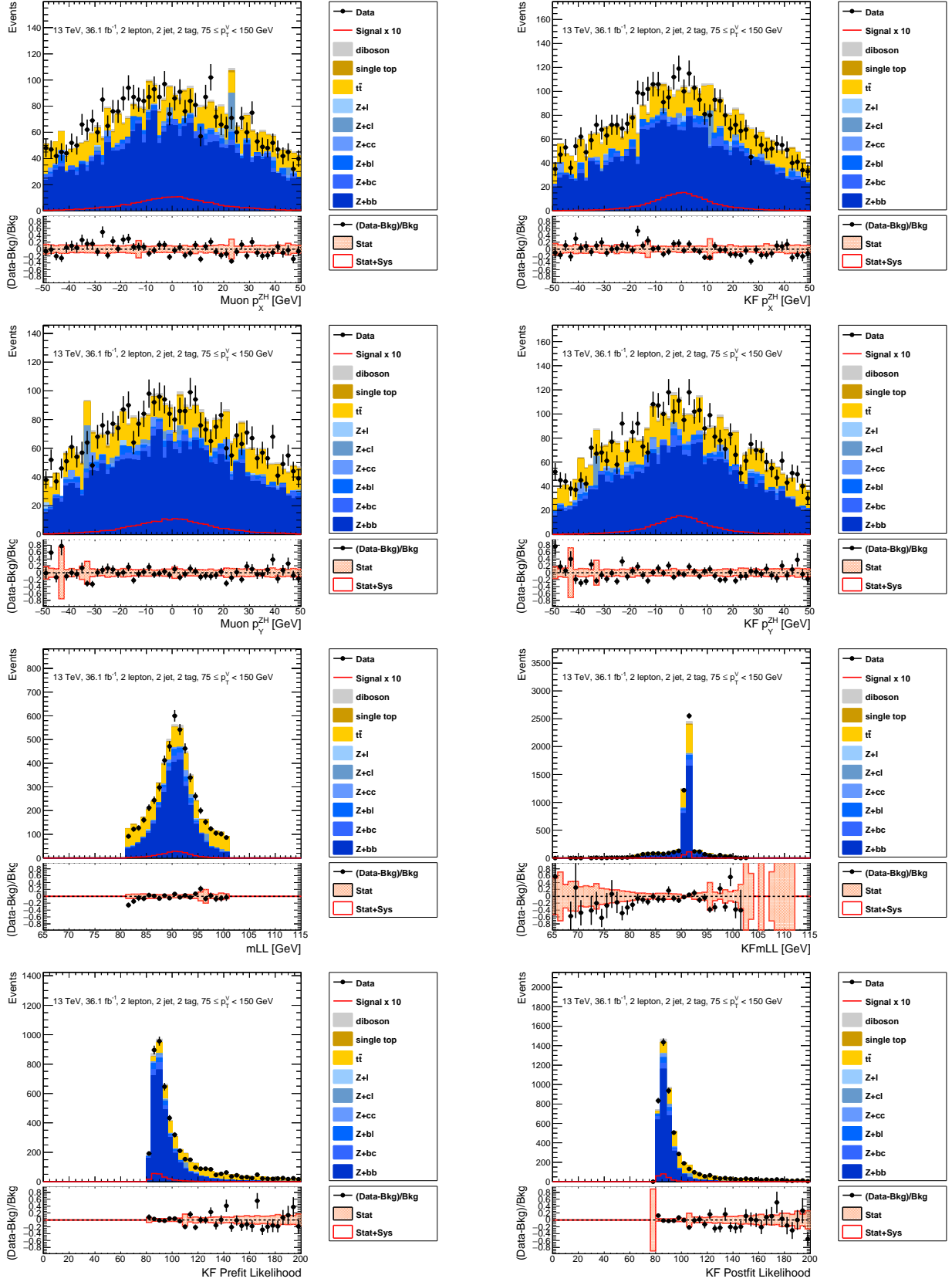
Figure B.7 KF variables in 2 jet p_T^V 75–150 GeV (2). before KL (left) and after KF (right). From top to bottom p_X^{ZH}, p_Y^{ZH}, $m_{\ell\ell}$, the likelihood. Signal is scaled by 10. Z+HF and $t\bar{t}$ are scaled by the same factors in section 11.1.
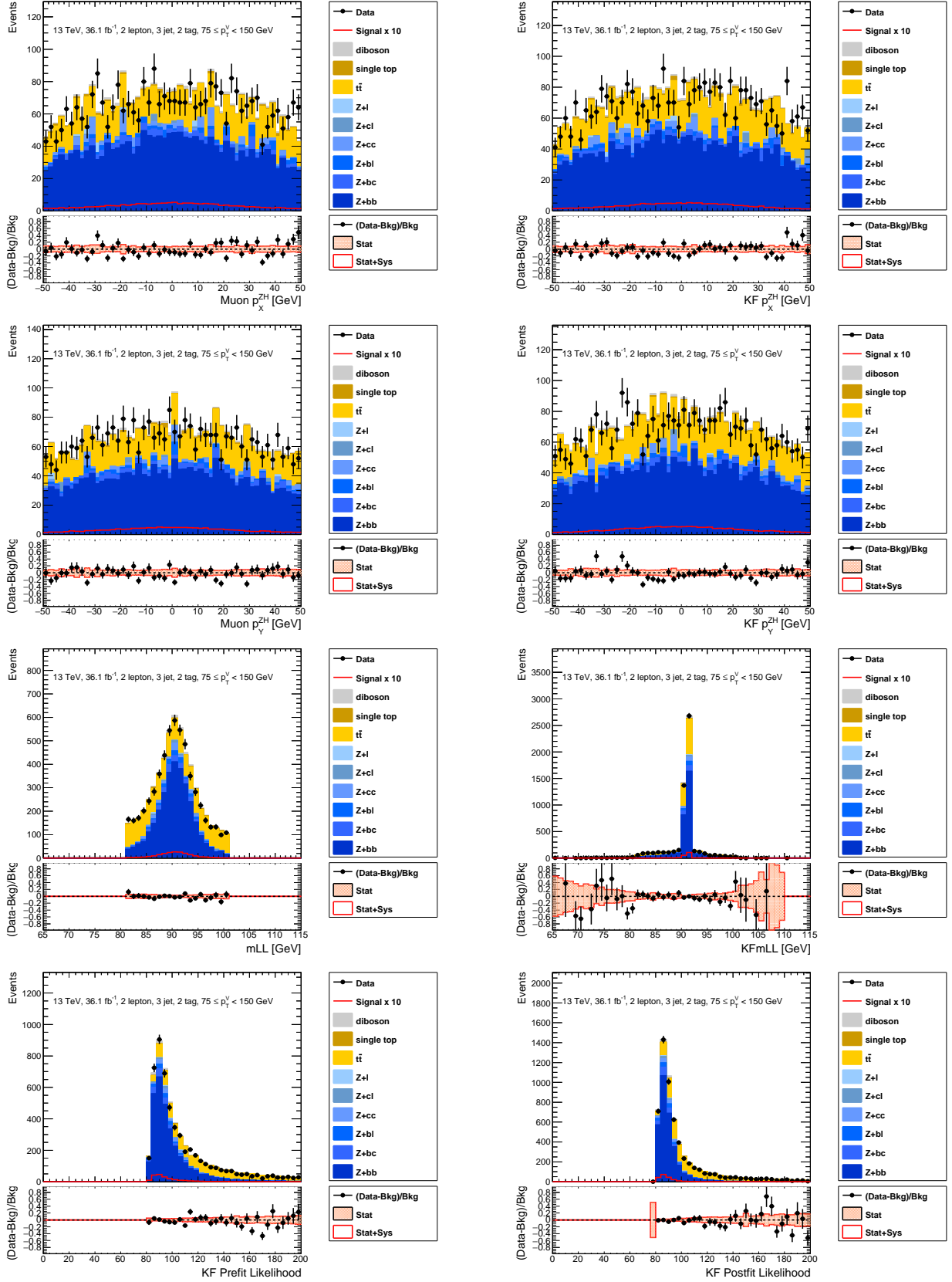
Figure B.8   KF variables in 3 jet p_T^V 75–150 GeV (2). before KL (left) and after KF (right). From top to bottom p_X^{ZH}, p_Y^{ZH}, $m_{\ell\ell}$, the likelihood. Signal is scaled by 10. Z+HF and $t\bar{t}$ are scaled by the same factors in section 11.1.
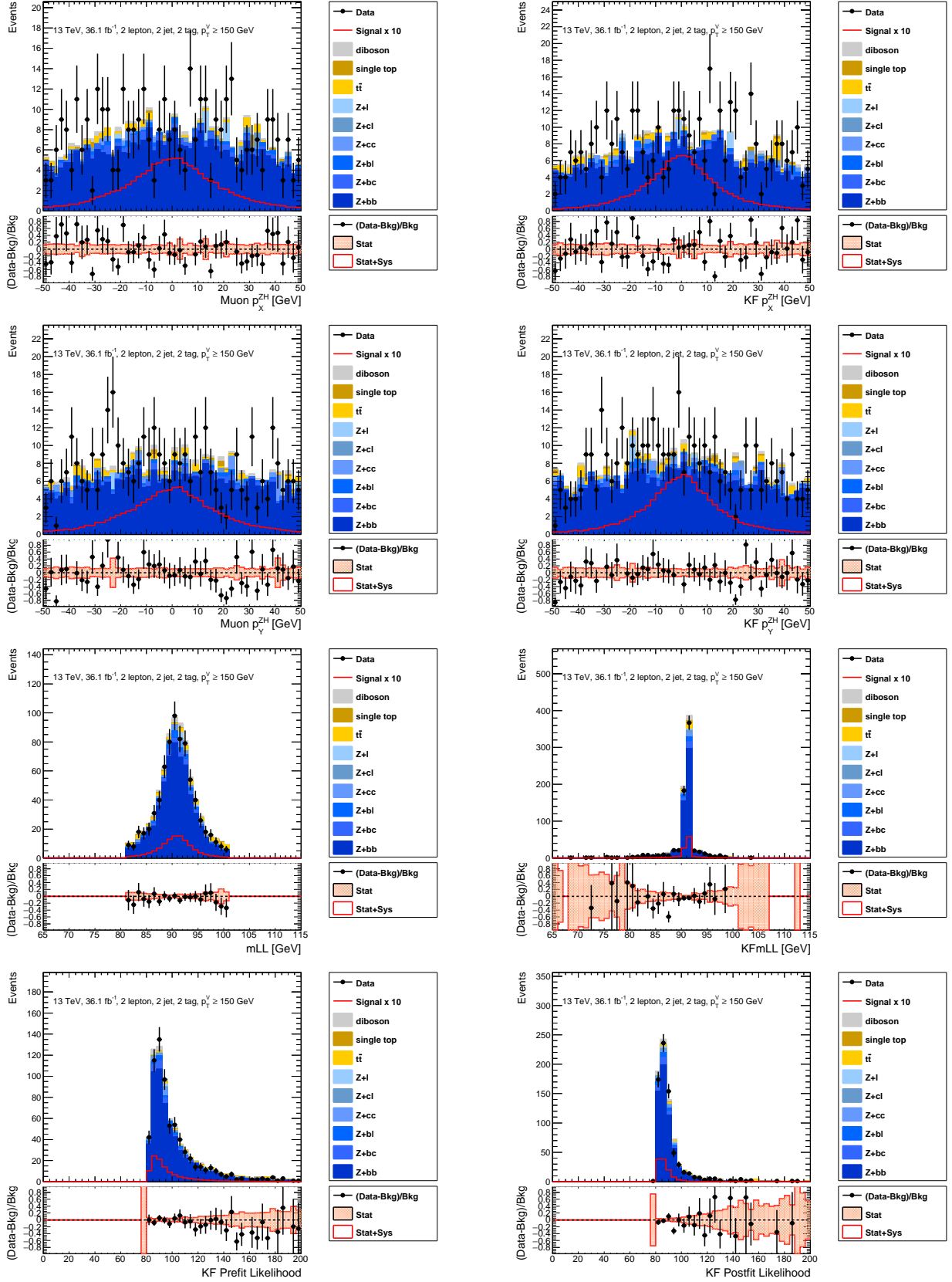
Figure B.9   KF variables in 2 jet p_T^V 150– GeV (2). before KL (left) and after KF (right). From top to bottom p_X^{ZH}, p_Y^{ZH}, $m_{\ell\ell}$, the likelihood. Signal is scaled by 10. Z+HF and $t\bar{t}$ are scaled by the same factors in section 11.1.
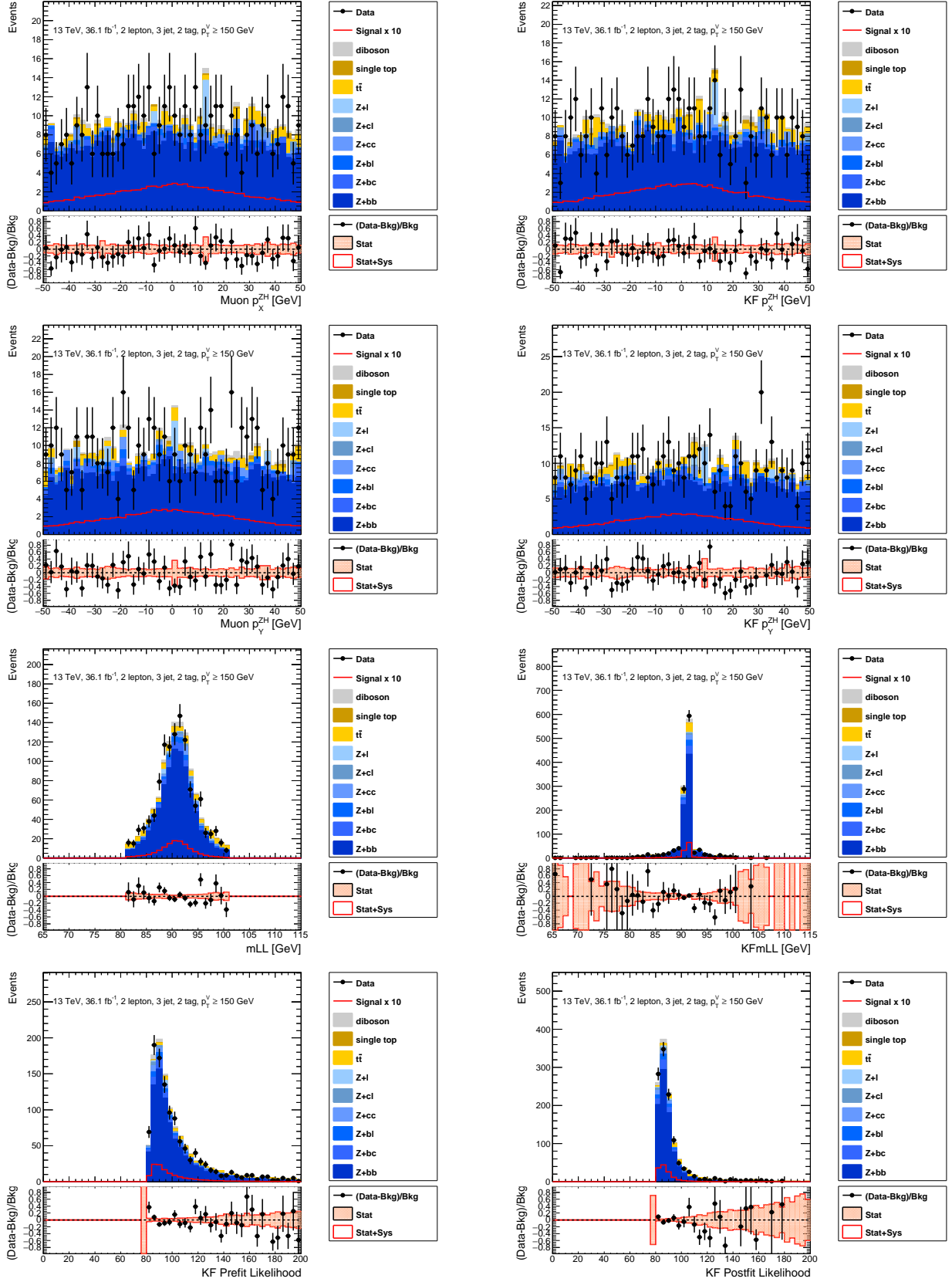
Figure B.10   KF variables in 3 jet p_T^V 150– GeV (2). before KL (left) and after KF (right). From top to bottom p_X^{ZH}, p_Y^{ZH}, $m_{\ell\ell}$, the likelihood. Signal is scaled by 10. Z+HF and $t\bar{t}$ are scaled by the same factors in section 11.1.
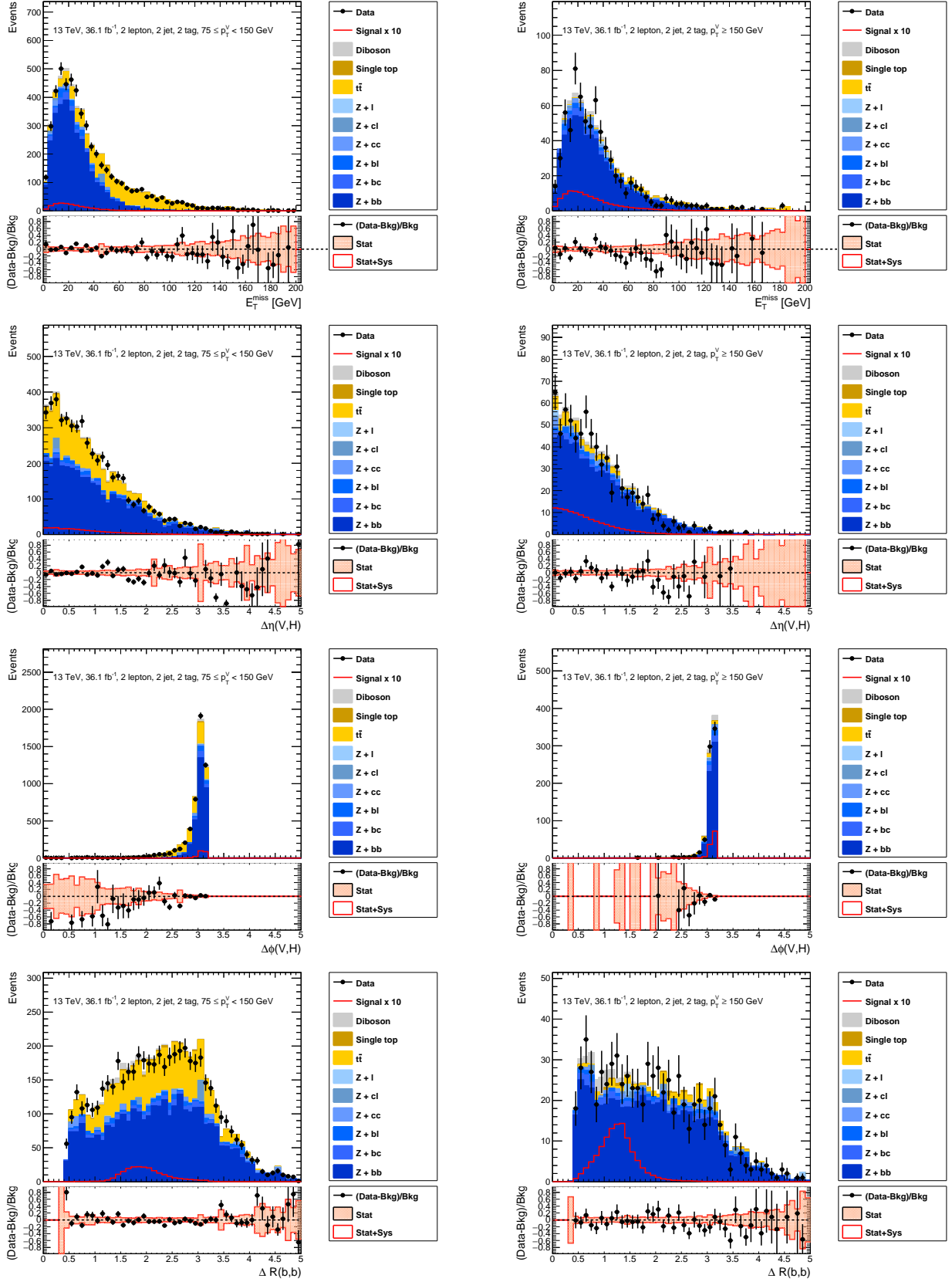
Figure C.11   BDT input variables in 2 jet (1). p_T^V = 75–150 GeV (left) and 150– GeV (right). E_T^{miss}, $\Delta\eta(V,H)$, $\Delta\phi(V,H)$, $\Delta R(b,b)$ from top to bottom. Signal is scaled by 10. Z+HF and $t\bar{t}$ are scaled by the same factors in section 11.1.
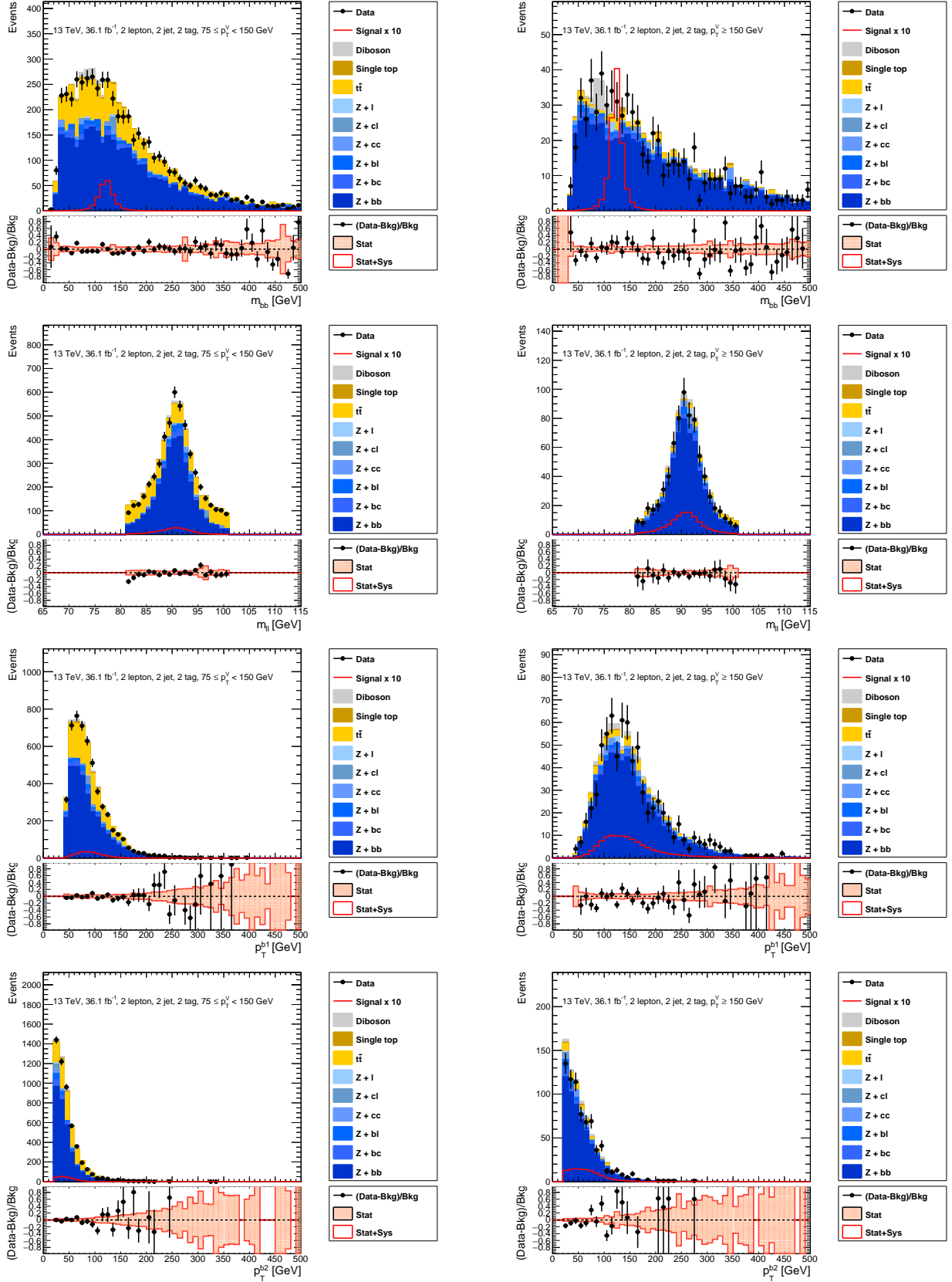
Figure C.12   BDT input variables in 2 jet (2). $p_T^V = 75$–150 GeV (left) and 150– GeV (right). m_{bb}, $m_{\ell\ell}$, p_T^{b1}, p_T^{b2} from top to bottom. Signal is scaled by 10. Z+HF and $t\bar{t}$ are scaled by the same factors in section 11.1.
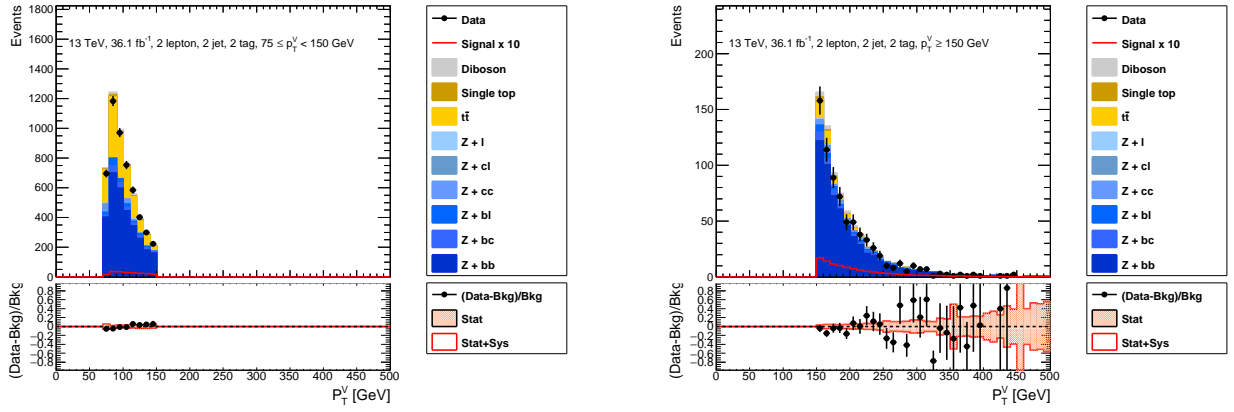
Figure C.13   BDT input variables in 2 jet (3). p_T^V = 75–150 GeV (left) and 150– GeV (right). Signal is scaled by 10. Z+HF and $t\bar{t}$ are scaled by the same factors in section 11.1.
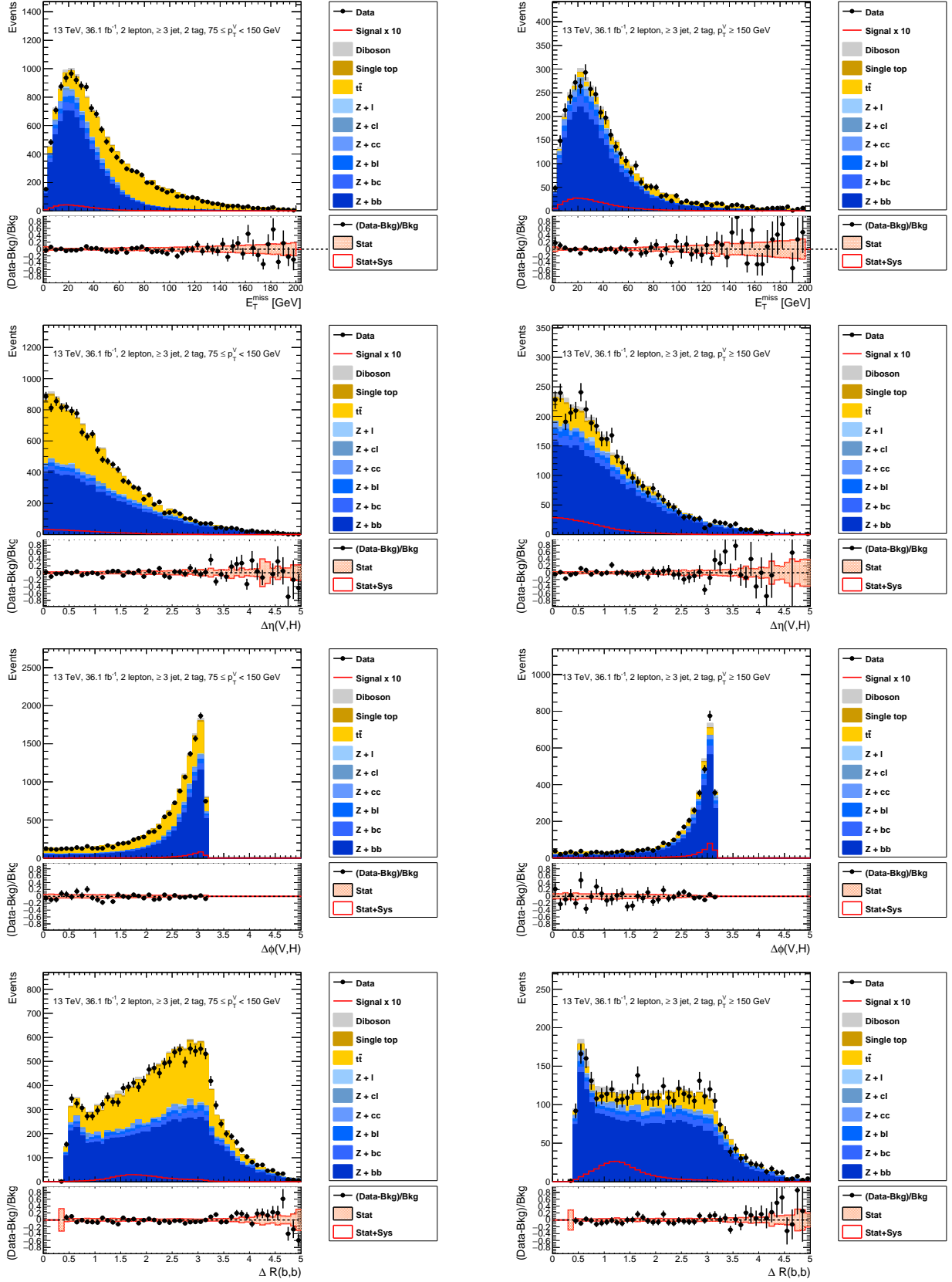
Figure C.14 — BDT input variables in ≥ 3 jet (1). $p_T^V = 75$–150 GeV (left) and 150– GeV (right). E_T^{miss}, $\Delta\eta(V,H)$, $\Delta\phi(V,H)$, $\Delta R(b,b)$ from top to bottom. Signal is scaled by 10. Z+HF and $t\bar{t}$ are scaled by the same factors in section 11.1.
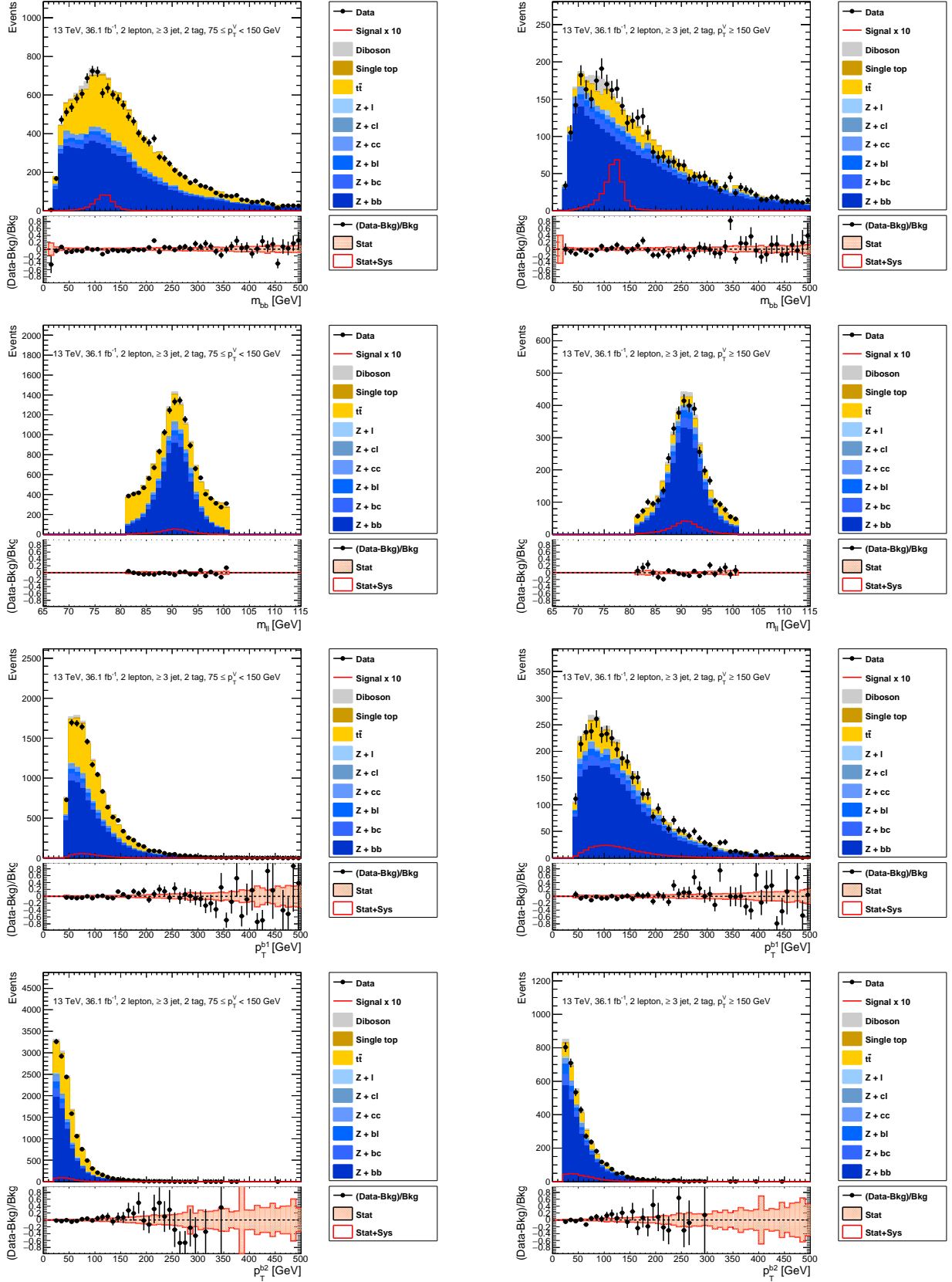
Figure C.15   BDT input variables in ≥ 3 jet (2). $p_T^V = 75$–150 GeV (left) and 150– GeV (right). m_{bb}, $m_{\ell\ell}$, p_T^{b1}, p_T^{b2} from top to bottom. Signal is scaled by 10. Z+HF and $t\bar{t}$ are scaled by the same factors in section 11.1.
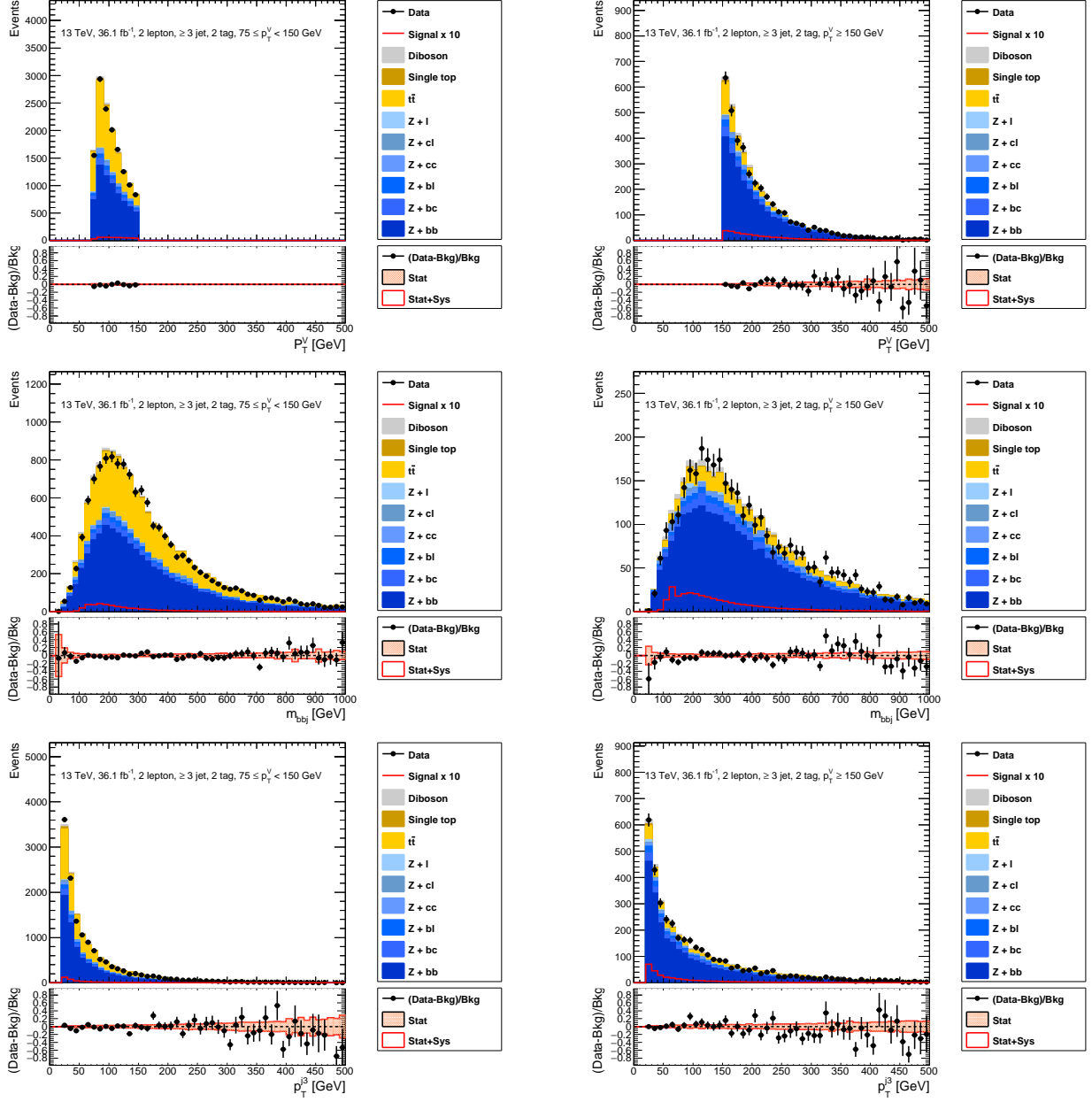
Figure C.16   BDT input variables in ≥ 3 jet (3). $p_{\mathrm{T}}^V = 75$–150 GeV (left) and 150– GeV (right). p_{T}^V, m_{bbj}, p_{T}^{j3}, from top to bottom. Signal is scaled by 10. Z+HF and $t\bar{t}$ are scaled by the same factors in section 11.1.
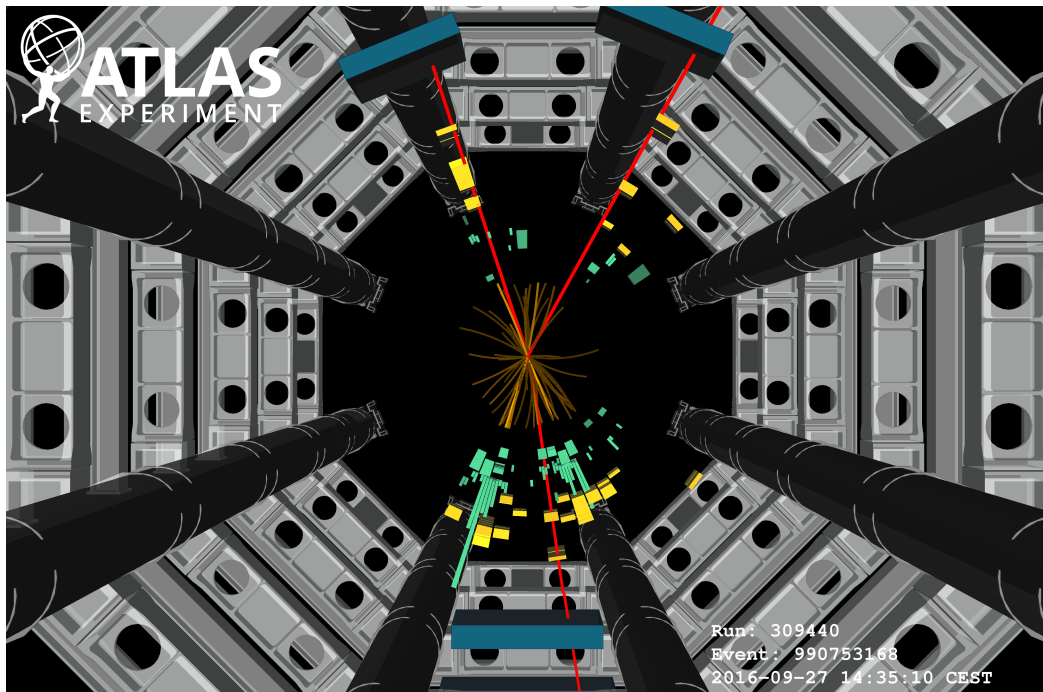
Figure D.17   A 2 muon, 2 tag, 2 jet event in high BDT$_{VH}$ region [90]. Red tracks are muons. Green bars are the energy depositions in the electromagnetic calorimeter. Yellow bars are the energy depositions in the hadronic calorimeter.

Acknowledgement

References

[1] F. Englert and R. Brout. Broken Symmetry and the Mass of Gauge Vector Mesons. *Phys. Rev. Lett.*, 13: 321–323, 1964. doi: 10.1103/PhysRevLett.13.321.

[2] Peter W. Higgs. Broken symmetries, massless particles and gauge fields. *Phys. Lett.*, 12:132–133, 1964. doi: 10.1016/0031-9163(64)91136-9.

[3] Peter W. Higgs. Broken Symmetries and the Masses of Gauge Bosons. *Phys. Rev. Lett.*, 13:508–509, 1964. doi: 10.1103/PhysRevLett.13.508.

[4] G. S. Guralnik, C. R. Hagen, and T. W. B. Kibble. Global Conservation Laws and Massless Particles. *Phys. Rev. Lett.*, 13:585–587, 1964. doi: 10.1103/PhysRevLett.13.585.

[5] Peter W. Higgs. Spontaneous Symmetry Breakdown without Massless Bosons. *Phys. Rev.*, 145:1156–1163, 1966. doi: 10.1103/PhysRev.145.1156.

[6] T. W. B. Kibble. Symmetry breaking in nonAbelian gauge theories. *Phys. Rev.*, 155:1554–1561, 1967. doi: 10.1103/PhysRev.155.1554.

[7] The ATLAS Collaboration. Observation of a new particle in the search for the standard model higgs boson with the atlas detector at the lhc. 2012. doi: 10.1016/j.physletb.2012.08.020.

[8] The CMS Collaboration. Observation of a new boson at a mass of 125 gev with the cms experiment at the lhc. 2012. doi: 10.1016/j.physletb.2012.08.021.

[9] C. Patrignani and Particle Data Group. Review of particle physics. *Chinese Physics C*, 40(10):100001, 2016. URL http://stacks.iop.org/1674-1137/40/i=10/a=100001.

[10] ATLAS Collaboration. Search for the $b\bar{b}$ decay of the standard model higgs boson in associated $(w/z)h$ production with the atlas detector. 2014. doi: 10.1007/JHEP01(2015)069.

[11] CMS Collaboration. Search for the standard model higgs boson produced in association with a w or a z boson and decaying to bottom quarks. 2013. doi: 10.1103/PhysRevD.89.012003.

[12] ATLAS Collaboration. Constraints on new phenomena via higgs boson couplings and invisible decays with the atlas detector. 2015. doi: 10.1007/JHEP11(2015)206.

[13] CDF Collaboration and D0 Collaboration. Evidence for a particle produced in association with weak bosons and decaying to a bottom-antibottom quark pair in higgs boson searches at the tevatron. 2012. doi: 10.1103/PhysRevLett.109.071804.

[14] ATLAS and CMS Collaborations. Measurements of the higgs boson production and decay rates and constraints on its couplings from a combined atlas and cms analysis of the lhc pp collision data at $\sqrt{s} = 7$ and 8 tev. 2016. doi: 10.1007/JHEP08(2016)045.

[15] F. Halzen and Alan D. Martin. *QUARKS AND LEPTONS: AN INTRODUCTORY COURSE IN MODERN PARTICLE PHYSICS*. 1984. ISBN 0471887412, 9780471887416.

[16] The Super-Kamiokande Collaboration and Y. Fukuda et al. Evidence for oscillation of atmospheric neutri-

nos. 1998. doi: 10.1103/PhysRevLett.81.1562.

[17] Lyndon Evans and Philip Bryant. Lhc machine. 2008. URL http://stacks.iop.org/1748-0221/3/i=08/a=S08001.

[18] J. M. Campbell, J. W. Huston, and W. J. Stirling. Hard interactions of quarks and gluons: a primer for lhc physics. 2006. doi: 10.1088/0034-4885/70/1/R02.

[19] ATLAS Collaboration. Luminosity determination in pp collisions at $\sqrt{s} = 8$ tev using the atlas detector at the lhc. 2016. doi: 10.1140/epjc/s10052-016-4466-1.

[20] A. D. Martin, W. J. Stirling, R. S. Thorne, and G. Watt. Parton distributions for the lhc. 2009. doi: 10.1140/epjc/s10052-009-1072-5.

[21] John C. Collins, Davison E. Soper, and George Sterman. Factorization of hard processes in qcd. 2004.

[22] W.J. Stirling. private communication. 2012. URL http://www.hep.ph.ic.ac.uk/%7Ewstirlin/plots/plots.html.

[23] ATLAS Collaboration. Study of the spin and parity of the higgs boson in diboson decays with the atlas detector. 2015. doi: 10.1140/epjc/s10052-015-3685-1.

[24] LHC Higgs Cross Section Working Group. Handbook of lhc higgs cross sections: 4. deciphering the nature of the higgs sector. 2016. URL https://cds.cern.ch/record/2227475.

[25] Jorg Wenninger. Approaching the Nominal Performance at the LHC. page MOYAA1. 6 p, 2017. URL https://cds.cern.ch/record/2289717.

[26] Fabienne Marcastel. Cern's accelerator complex. 2013. URL https://cds.cern.ch/record/1621583.

[27] Bruc et al. Lhc run 2: Results and challenges. Technical report, 2016. URL https://cds.cern.ch/record/2201447.

[28] ATLAS Collaborations. Luminosity public results run2. 2016. URL https://twiki.cern.ch/twiki/bin/view/AtlasPublic/LuminosityPublicResultsRun2.

[29] The ATLAS Collaboration. The atlas experiment at the cern large hadron collider. *Journal of Instrumentation*, 3(08):S08003, 2008. URL http://stacks.iop.org/1748-0221/3/i=08/a=S08003.

[30] Karolos Potamianos. The upgraded pixel detector and the commissioning of the inner detector tracking of the atlas experiment for run-2 at the large hadron collider. 2016.

[31] Expected performance of the ATLAS b-tagging algorithms in Run-2. Technical Report ATL-PHYS-PUB-2015-022, CERN, Geneva, Jul 2015. URL https://cds.cern.ch/record/2037697.

[32] ATLAS Collaboration. Optimisation of the ATLAS b-tagging performance for the 2016 LHC Run. Technical Report ATL-PHYS-PUB-2016-012, CERN, Geneva, Jun 2016. URL https://cds.cern.ch/record/2160731.

[33] Bartosz Mindur. ATLAS Transition Radiation Tracker (TRT): Straw tubes for tracking and particle identification at the Large Hadron Collider. Technical Report ATL-INDET-PROC-2016-001, CERN, Geneva, Mar 2016. URL https://cds.cern.ch/record/2139567.

[34] ATLAS Collaboration. L1 muon trigger public results, 2015. URL https://twiki.cern.ch/twiki/bin/view/AtlasPublic/L1MuonTriggerPublicResults.

[35] ATLAS Collaboration. Muon trigger public results, 2016. URL https://twiki.cern.ch/twiki/bin/view/AtlasPublic/MuonTriggerPublicResults.

[36] ATLAS Collaboration. The atlas simulation infrastructure. 2010. doi: 10.1140/epjc/s10052-010-1429-9.

[37] Torbjãűrn Sjãűstrand, Stephen Mrenna, and Peter Skands. A brief introduction to pythia 8.1. 2007. doi: 10.1016/j.cpc.2008.01.036.

[38] ATLAS Collaboration. Summary of ATLAS Pythia 8 tunes. Technical Report ATL-PHYS-PUB-2012-003, CERN, Geneva, Aug 2012. URL https://cds.cern.ch/record/1474107.

[39] D. J. Lange. The EvtGen particle decay simulation package. *Nucl. Instrum. Meth.*, A462:152–155, 2001. doi: 10.1016/S0168-9002(01)00089-4.

[40] T. Gleisberg, S. Hoeche, F. Krauss, M. Schoenherr, S. Schumann, F. Siegert, and J. Winter. Event generation with sherpa 1.1. 2008. doi: 10.1088/1126-6708/2009/02/007.

[41] Jon Butterworth, Stefano Carrazza, Amanda Cooper-Sarkar, Albert De Roeck, Joel Feltesse, Stefano Forte, Jun Gao, Sasha Glazov, Joey Huston, Zahari Kassabov, Ronan McNulty, Andreas Morsch, Pavel Nadolsky, Voica Radescu, Juan Rojo, and Robert Thorne. Pdf4lhc recommendations for lhc run ii. 2015. doi: 10.1088/0954-3899/43/2/023001.

[42] Gionata Luisoni, Paolo Nason, Carlo Oleari, and Francesco Tramontano. Hw/hz + 0 and 1 jet at nlo with the powheg box interfaced to gosam and their merging within minlo. 2013. doi: 10.1007/JHEP10(2013)083.

[43] Stefano Frixione, Paolo Nason, and Carlo Oleari. Matching nlo qcd computations with parton shower simulations: the powheg method. 2007. doi: 10.1088/1126-6708/2007/11/070.

[44] Simone Alioli, Paolo Nason, Carlo Oleari, and Emanuele Re. A general framework for implementing nlo calculations in shower monte carlo programs: the powheg box. 2010. doi: 10.1007/JHEP06(2010)043.

[45] Gavin Cullen, Nicolas Greiner, Gudrun Heinrich, Gionata Luisoni, Pierpaolo Mastrolia, Giovanni Ossola, Thomas Reiter, and Francesco Tramontano. Automated one-loop calculations with gosam. 2011. doi: 10.1140/epjc/s10052-012-1889-1.

[46] Keith Hamilton, Paolo Nason, and Giulia Zanderighi. Minlo: Multi-scale improved nlo. 2012. doi: 10.1007/JHEP10(2012)155.

[47] Ansgar Denner, Stefan Dittmaier, Stefan Kallweit, and Alexander MÃijck. Hawk 2.0: A monte carlo program for higgs production in vector-boson fusion and higgs strahlung at hadron colliders. 2014. doi: 10.1016/j.cpc.2015.04.021.

[48] ATLAS Collaboration. Measurement of the z/γ^* boson transverse momentum distribution in pp collisions at $\sqrt{s} = 7$ tev with the atlas detector. 2014. doi: 10.1007/JHEP09(2014)145.

[49] M. L. Ciccolini, S. Dittmaier, and M. Kramer. Electroweak radiative corrections to associated wh and zh production at hadron colliders. 2003. doi: 10.1103/PhysRevD.68.073003.

[50] Oliver Brein, Abdelhak Djouadi, and Robert Harlander. Nnlo qcd corrections to the higgs-strahlung processes at hadron colliders. 2003. doi: 10.1016/j.physletb.2003.10.112.

[51] Oliver Brein, Robert Harlander, Marius Wiesemann, and Tom Zirke. Top-quark mediated effects in hadronic higgs-strahlung. 2011. doi: 10.1140/epjc/s10052-012-1868-6.

[52] Giancarlo Ferrera, Massimiliano Grazzini, and Francesco Tramontano. Associated zh production at hadron colliders: the fully differential nnlo qcd calculation. 2014. doi: 10.1016/j.physletb.2014.11.040.

[53] John M. Campbell, R. Keith Ellis, and Ciaran Williams. Associated production of a higgs boson at nnlo. 2016. doi: 10.1007/JHEP06(2016)179.

[54] Lukas Altenkamp, Stefan Dittmaier, Robert V. Harlander, Heidi Rzehak, and Tom J. E. Zirke. Gluon-induced higgs-strahlung at next-to-leading order qcd. 2012. doi: 10.1007/JHEP02(2013)078.

[55] B. Hespel, F. Maltoni, and E. Vryonidou. Higgs and z boson associated production via gluon fusion in the sm and the 2hdm, 2015.

[56] Robert V. Harlander, Anna Kulesza, Vincent Theeuwes, and Tom Zirke. Soft gluon resummation for gluon-induced higgs strahlung. 2014. doi: 10.1007/JHEP11(2014)082.

[57] Robert V. Harlander, Stefan Liebler, and Tom Zirke. Higgs strahlung at the large hadron collider in the 2-higgs-doublet model. 2013. doi: 10.1007/JHEP02(2014)023.

[58] Oliver Brein, Robert V. Harlander, and Tom J. E. Zirke. vh@nnlo - higgs strahlung at hadron colliders. 2012. doi: 10.1016/j.cpc.2012.11.002.

[59] Stefano Frixione, Paolo Nason, and Giovanni Ridolfi. A positive-weight next-to-leading-order monte carlo for heavy flavour hadroproduction. 2007. doi: 10.1088/1126-6708/2007/09/126.

[60] ATLAS Run 1 Pythia8 tunes. Technical Report ATL-PHYS-PUB-2014-021, CERN, Geneva, Nov 2014. URL http://cds.cern.ch/record/1966419.

[61] Simone Alioli, Paolo Nason, Carlo Oleari, and Emanuele Re. Nlo single-top production matched with shower in powheg: s- and t-channel contributions. 2009. doi: 10.1088/1126-6708/2009/09/11110.1007/JHEP02(2010)011.

[62] Emanuele Re. Single-top wt-channel production matched with parton showers using the powheg method. 2010. doi: 10.1140/epjc/s10052-011-1547-z.

[63] Peter Zeiler Skands. Tuning monte carlo generators: The perugia tunes. 2010. doi: 10.1103/PhysRevD.82.074018.

[64] Michal Czakon and Alexander Mitov. Top++: a program for the calculation of the top-pair cross-section at hadron colliders. 2011. doi: 10.1016/j.cpc.2014.06.021.

[65] Nikolaos Kidonakis. Nnll resummation for s-channel single top quark production. 2010. doi: 10.1103/PhysRevD.81.054028.

[66] Nikolaos Kidonakis. Next-to-next-to-leading-order collinear and soft gluon corrections for t-channel single top quark production. 2011. doi: 10.1103/PhysRevD.83.091503.

[67] Nikolaos Kidonakis. Two-loop soft anomalous dimensions for single top quark associated production with a w- or h-. 2010. doi: 10.1103/PhysRevD.82.054018.

[68] Monte Carlo Generators for the Production of a W or Z/γ^* Boson in Association with Jets at ATLAS in Run 2. Technical Report ATL-PHYS-PUB-2016-003, CERN, Geneva, Jan 2016. URL https://cds.cern.ch/record/2120133.

[69] Richard D. Ball, Valerio Bertone, Stefano Carrazza, Christopher S. Deans, Luigi Del Debbio, Stefano Forte, Alberto Guffanti, Nathan P. Hartland, Jose I. Latorre, Juan Rojo, and Maria Ubiali. Parton distributions with lhc data. 2012. doi: 10.1016/j.nuclphysb.2012.10.003.

[70] Fabio Cascioli, Philipp Maierhöfer, and Stefano Pozzorini. Scattering amplitudes with open loops. 2011. doi: 10.1103/PhysRevLett.108.111601.

[71] Tanju Gleisberg and Stefan Hoeche. Comix, a new matrix element generator. 2008. doi: 10.1088/1126-6708/2008/12/039.

[72] Leif Lonnblad. Correcting the colour-dipole cascade model with fixed order matrix elements. 2001. doi: 10.1088/1126-6708/2002/05/046.

[73] Nils Lavesson and Leif Lonnblad. W+jets matrix elements and the dipole cascade. 2005. doi: 10.1088/1126-6708/2005/07/054.

[74] S. Catani, L. Cieri, G. Ferrera, D. de Florian, and M. Grazzini. Vector boson production at hadron colliders: a fully exclusive qcd calculation at nnlo. 2009. doi: 10.1103/PhysRevLett.103.082001.

[75] Multi-Boson Simulation for 13 TeV ATLAS Analyses. Technical Report ATL-PHYS-PUB-2017-005, CERN, Geneva, May 2017. URL https://cds.cern.ch/record/2261933.

[76] ATLAS Collaboration. Reconstruction of primary vertices at the atlas experiment in run 1 proton-proton

collisions at the lhc. 2016. doi: 10.1140/epjc/s10052-017-4887-5.

[77] ATLAS Collaboration. Electron efficiency measurements with the ATLAS detector using the 2015 LHC proton-proton collision data. Technical Report ATLAS-CONF-2016-024, CERN, Geneva, Jun 2016. URL https://cds.cern.ch/record/2157687.

[78] Improved electron reconstruction in ATLAS using the Gaussian Sum Filter-based model for bremsstrahlung. Technical Report ATLAS-CONF-2012-047, CERN, Geneva, May 2012. URL http://cds.cern.ch/record/1449796.

[79] Electron and photon energy calibration with the ATLAS detector using data collected in 2015 at $\sqrt{s} = 13$ TeV. Technical Report ATL-PHYS-PUB-2016-015, CERN, Geneva, Aug 2016. URL https://cds.cern.ch/record/2203514.

[80] ATLAS Collaboration. Muon reconstruction performance of the ATLAS detector in proton–proton collision data at $\sqrt{s} = 13$ TeV. 2016. doi: 10.1140/epjc/s10052-016-4120-y.

[81] ATLAS Collaboration. Jet energy scale measurements and their systematic uncertainties in proton-proton collisions at $\sqrt{s} = 13$ TeV with the ATLAS detector, 2017.

[82] ATLAS Collaboration. Selection of jets produced in 13TeV proton-proton collisions with the ATLAS detector. Technical Report ATLAS-CONF-2015-029, CERN, Geneva, Jul 2015. URL https://cds.cern.ch/record/2037702.

[83] ATLAS Collaboration. Performance of pile-up mitigation techniques for jets in pp collisions at $\sqrt{s} = 8$ TeV using the ATLAS detector. 2015. doi: 10.1140/epjc/s10052-016-4395-z.

[84] ATLAS Collaboration. Performance of b-jet identification in the atlas experiment. 2015. doi: 10.1088/1748-0221/11/04/P04008.

[85] ATLAS Collaboration. Measurement of the tau lepton reconstruction and identification performance in the ATLAS experiment using pp collisions at $\sqrt{s} = 13$ TeV. Technical Report ATLAS-CONF-2017-029, CERN, Geneva, May 2017. URL https://cds.cern.ch/record/2261772.

[86] ATLAS Collaboration. Performance of missing transverse momentum reconstruction for the ATLAS detector in the first proton-proton collisions at at $\sqrt{s}= 13$ TeV. Technical Report ATL-PHYS-PUB-2015-027, CERN, Geneva, Jul 2015. URL https://cds.cern.ch/record/2037904.

[87] Manuel Proissl. Dijet Invariant Mass Studies in the Higgs boson $H \to b\bar{b}$ resonance search in association with a W/Z boson using the ATLAS detector, 2014. URL https://cds.cern.ch/record/1997808. Presented 2014.

[88] A. D. Bukin. Fitting function for asymmetric peaks, 2007.

[89] A. Hoecker, P. Speckmayer, J. Stelzer, J. Therhaag, E. von Toerne, H. Voss, M. Backes, T. Carli, O. Cohen, A. Christov, D. Dannheim, K. Danielowski, S. Henrot-Versille, M. Jachowski, K. Kraszewski, A. Krasznahorkay Jr., M. Kruk, Y. Mahalalel, R. Ospanov, X. Prudent, A. Robert, D. Schouten, F. Tegenfeldt, A. Voigt, K. Voss, M. Wolter, and A. Zemla. Tmva - toolkit for multivariate data analysis. 2007.

[90] ATLAS Collaboration. Evidence for the $h \to b\bar{b}$ decay with the atlas detector, 2017. URL https://atlas.web.cern.ch/Atlas/GROUPS/PHYSICS/PAPERS/HIGG-2016-29/.

[91] Daniel Buscher and Karl Jakobs. Search for Higgs bosons with b-jets in the final state in proton-proton collisions with the ATLAS experiment, Nov 2016. URL https://cds.cern.ch/record/2232472. Presented 26 Oct 2016.

[92] Jet Calibration and Systematic Uncertainties for Jets Reconstructed in the ATLAS Detector at $\sqrt{s} = 13$ TeV. Technical Report ATL-PHYS-PUB-2015-015, CERN, Geneva, Jul 2015. URL http://cds.cern.ch/

record/2037613.

[93] Expected performance of missing transverse momentum reconstruction for the ATLAS detector at $\sqrt{s} =$ 13 TeV. Technical Report ATL-PHYS-PUB-2015-023, CERN, Geneva, Jul 2015. URL https://cds.cern.ch/record/2037700.

[94] Andy Buckley, Jonathan Butterworth, David Grellscheid, Hendrik Hoeth, Leif Lonnblad, James Monk, Holger Schulz, and Frank Siegert. Rivet user manual, 2010.

[95] J. Alwall, R. Frederix, S. Frixione, V. Hirschi, F. Maltoni, O. Mattelaer, H. S. Shao, T. Stelzer, P. Torrielli, and M. Zaro. The automated computation of tree-level and next-to-leading order differential cross sections, and their matching to parton shower simulations. 2014. doi: 10.1007/JHEP07(2014)079.

[96] Johannes Bellm, Stefan Gieseke, David Grellscheid, Simon Platzer, Michael Rauch, Christian Reuschle, Peter Richardson, Peter Schichtel, Michael H. Seymour, Andrzej Siodmok, Alexandra Wilcock, Nadine Fischer, Marco A. Harrendorf, Graeme Nail, Andreas Papaefstathiou, and Daniel Rauch. Herwig 7.0 / herwig++ 3.0 release note. 2015. doi: 10.1140/epjc/s10052-016-4018-8.

[97] S. Frixione, E. Laenen, P. Motylinski, B. Webber, and C. D. White. Single-top hadroproduction in association with a w boson. 2008. doi: 10.1088/1126-6708/2008/07/029.

[98] Iain W. Stewart and Frank J. Tackmann. Theory uncertainties for higgs and other searches using jet bins. 2011. doi: 10.1103/PhysRevD.85.034011.

[99] LHC Higgs Cross Section Working Group. Handbook of lhc higgs cross sections: 3. higgs properties. 2013. doi: 10.5170/CERN-2013-004.

[100] Lorenzo Moneta, Kevin Belasco, Kyle Cranmer, Sven Kreiss, Alfio Lazzaro, Danilo Piparo, Gregory Schott, Wouter Verkerke, and Matthias Wolf. The roostats project, 2010.

[101] Roger Barlow and Christine Beeston. Fitting using finite monte carlo samples. *Computer Physics Communications*, 77(2):219 – 228, 1993. ISSN 0010-4655. doi: https://doi.org/10.1016/0010-4655(93)90005-W. URL http://www.sciencedirect.com/science/article/pii/001046559390005W.

[102] Glen Cowan, Kyle Cranmer, Eilam Gross, and Ofer Vitells. Asymptotic formulae for likelihood-based tests of new physics. 2010. doi: 10.1140/epjc/s10052-011-1554-0.

[103] A L Read. Presentation of search results: the cl s technique. *Journal of Physics G: Nuclear and Particle Physics*, 28(10):2693, 2002. URL http://stacks.iop.org/0954-3899/28/i=10/a=313.